DYNAMIC FRACTURE OF EXPLOSIVE BOLT

A THESIS SUBMITTED TO
THE GRADUATE SCHOOL OF NATURAL AND APPLIED SCIENCES
OF
MIDDLE EAST TECHNICAL UNIVERSITY

BY

BATUHAN GÖKÇE

IN PARTIAL FULFILLMENT OF THE REQUIREMENTS
FOR
THE DEGREE OF MASTER OF SCIENCE
IN
MECHANICAL ENGINEERING

JUNE 2018

Approval of the thesis:

DYNAMIC FRACTURE OF EXPLOSIVE BOLT

submitted by **BATUHAN GÖKÇE** in partial fulfillment of the requirements for the degree of **Master of Science in Mechanical Engineering Department, Middle East Technical University** by,

Prof. Dr. Halil Kalıpçılar
Dean, Graduate School of **Natural and Applied Sciences** _____

Prof. Dr. M. A. Sahir Arıkan
Head of Department, **Mechanical Engineering** _____

Assist. Prof. Dr. Hüsnü DAL
Supervisor, **Mechanical Engineering Dept., METU** _____

Prof. Dr. R. Orhan YILDIRIM
Co-Supervisor, **Mechanical Engineering Dept., METU** _____

Examining Committee Members:

Prof. Dr. Serkan DAĞ
Mechanical Engineering Dept., METU _____

Assist. Prof. Dr. Hüsnü DAL
Mechanical Engineering Dept., METU _____

Prof. Dr. R. Orhan YILDIRIM
Mechanical Engineering Dept., METU _____

Prof. Dr. Süha ORAL
Mechanical Engineering Dept., METU _____

Assoc. Prof. Dr. Murat DEMİRAL
Mechanical Engineering Dept., UTAA _____

Date: ___21.06.2018___

I hereby declare that all information in this document has been obtained and presented in accordance with academic rules and ethical conduct. I also declare that, as required by these rules and conduct, I have fully cited and referenced all material and results that are not original to this work.

Name, Surname   :   Batuhan GÖKÇE

Signature   :

ABSTRACT

DYNAMIC FRACTURE OF EXPLOSIVE BOLT

GÖKÇE, Batuhan

M.S., Department of Mechanical Engineering

Supervisor: Assist. Prof. Dr. Hüsnü DAL

Co-Supervisor: Prof. Dr. R. Orhan YILDIRIM

June 2018, 112 Pages

In this study, dynamic fracture of the pressure type explosive bolt is established with different geometry of the piston, which is used to break the body, to enhance the reliability of the system. Before the fracture analysis of the explosive bolts, pyrotechnic combustion analysis is studied and 0-D ballistic solver is developed to simulate the performance of the initiator into the pyrotechnic, namely pressure type, explosive bolt. By using the developed model, the pressure and temperature in the expansion chamber, the position and velocity of the piston can be predicted. After prediction of these parameters, the pressure expansion is validated with closed bomb experiments. Then, three different shape piston models are developed to study on clean separation without fragmenting parts with minimum dissipated of energy during the separation of the system to get higher reliability. The varied separation behavior of these pyrotechnic explosive bolt models are analyzed and compared in LS-DYNA.

Keywords: Pyrotechnics, Pyrotechnic Actuated Devices, Explosive Bolt, Ignition, Initiator

ÖZ

PATLAYAN CİVATANIN DİNAMİK KIRILIMI

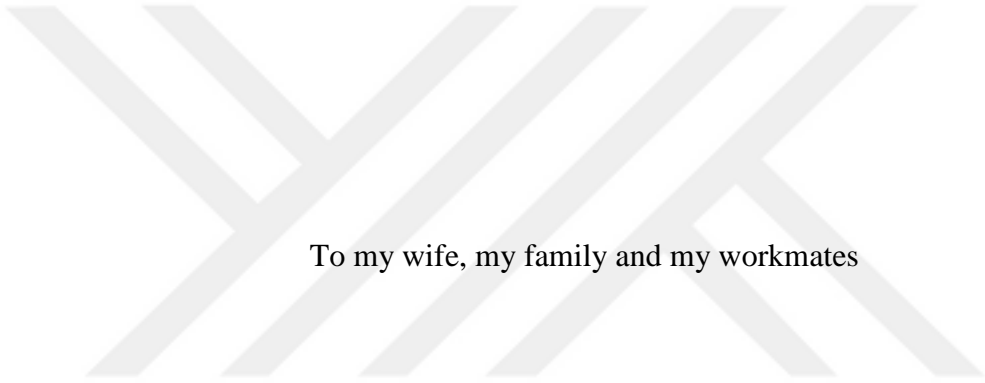GÖKÇE, Batuhan

Yüksek Lisans, Makina Mühendiliği Bölümü

Tez Yöneticisi: Dr. Öğr. Üyesi Hüsnü DAL

Yardımcı Tez Yöneticisi: Prof. Dr. R. Orhan YILDIRIM

Haziran 2018, 112 Sayfa

Bu tez çalışmasında, sistemin güvenilirliğini artırmak için farklı geometrilere sahip pistonlardan oluşan basınç tipli patlayan civataların kırılımı çalışılmıştır. Kırılım analizlerinden önce piroteknik patlayan civatanın içerisinde bulunan başlatıcı elemanın performansını benzetmek için sıfır boyutlu balistik bir kod geliştirilmiştir. Geliştirilen bu kodu kullanarak, genleşme haznesindeki basınç ve sıcaklık değerleriyle pistonun konumu ve hızı tahmin edilebilir. Bu parametrelerin tahmininden sonra kapalı bomba testleriyle balistik kodun doğrulaması gerçekleştirilmiştir. Sistemin güvenilirliğini artırmak için parçacık oluşturmayan, en düşük enerji kaybıyla gerçekleşen temiz bir ayrılma üzerinde çalışmak için üç farklı piston modeli oluşturulmuştur. Bu modellerin farklı ayrılma davranışları LS-DYNA ile analiz edilmiş ve karşılaştırılmıştır.

Anahtar Kelimeler: Piroteknik, Piroteknik Tahrikli Aygıtlar, Patlayan Civata, Ateşleme, Başlatıcı Eleman

To my wife, my family and my workmates

ACKNOWLEDGEMENTS

TABLE OF CONTENTS

LIST OF TABLES

LIST OF FIGURES

FIGURES

LIST OF SYMBOLS

A	initial yield strength
$a_1 \dots a_5$	least square constants
A_p	area of the piston
A_w	surface area between the bolt body and piston
B	hardening constant
b	pressure constant
c	wave speed
C	strain rate constant
C_0	bulk speed of sound
c_v	specific heat at the constant volume
C_p^0	molar heat capacitance at constant pressure
C_v^0	molar heat capacitance at constant volume
E	Young's modulus
e	specific internal energy
F_p	force on the piston
f_S	penalty force
h	convective heat transfer coefficient
H^0	enthalpy
I	internal force
K	tangent stiffness matrix
k_i	Fourth-order Runge-Kutta slopes
L	element size
M	diagonal mass matrix
m	thermal softening exponent
m_p	mass of the piston

n	pressure exponent
N	number of species
P_g	gas phase pressure
r	pyrotechnic burn rate
R	universal gas constant
T	temperature
T_m	melting temperature of a material
T_p	temperature of the products
T_w	temperature of the bolt body wall
u	displacement
$\dot{u}$	velocity
$\ddot{u}$	acceleration
U^0	internal energy
V	volume
v_p	velocity of the piston
Y	mass fractions of species
z_p	piston position
$\dot{Q}_{cp}$	heat transfer rates from surroundings to condensed phase products
$\dot{Q}_{cp,g}$	heat transfer rates from the condensed to gas phase products
$\dot{Q}_g$	heat transfer rates from the surroundings to gas phase products
$\dot{W}_g$	work done by the gas phase products
α	absorptivity of the bolt body
ε	net emissivity of the product mixture
ρ	density
σ	Stefan-Boltzman constant
η_{cp}	mass fraction of products in condensed phase
Δx	displacement
$\bar{\sigma}$	equivalent flow stress

$\bar{\varepsilon}$ equivalent plastic strain

Γ_0 Grüneisen's gamma

Subscripts

s solid

cp condensed phase

g gas phase

cp, g between condensed and gas phases

0 initial condition

CHAPTER 1

INTRODUCTION

Pyrotechnics have been utilized for many high technology applications such as spacecraft, aircraft and missile systems for ignition, booster separation, firing release and destruction cases of malfunction. In a variable or constant closed volume, overall chemical reactions of these energetic materials, indeed combustion, produce highly exothermic, transient, turbulent environment and consequently, the combustion products having high temperature increases the pressure. In some cases, this pressure can be utilized as mechanical work while it can be utilized as a shock wave by detonation. Pyrotechnic devices use this mechanical work and shock wave to complete their tasks. The main advantages of pyrotechnic devices are high power to weight ratio, high reliability, small size, low operating current, simple circuit requirement, reasonably low cost, ability to deliver more energy in a shorter time than any other mechanical device and controllable force [1].

Explosive bolts are one reliable and efficient pyrotechnic release devices used in many applications such as launcher operation, stage separation, rocket sled release, thrust termination and the release of external tanks [1]. It generally consists of permanent charge and initiator starting the explosive train. Up to now, various different shapes and size of explosive bolts have been designed for a great variety of application according to firing characteristics, size, shape, type of used charge and failure modes. However, high explosive and pressure types are well known two types of explosive bolts. To break the bolt, high explosive bolts create a shock wave inside the cavity with detonation, while pressure type explosive bolts generates high pressure with chemical reaction of the pyrotechnics. Pyrotechnic or pressure type of explosive bolt is a kind of non-fragmenting bolt and cannot damage to the other components

1

especially electrical ones. However, high explosive type bolts can be harmful for the electrical component because of the generated shock wave.

In this study, dynamic fracture of the pressure type explosive bolt is established with different geometry of the piston to enhance the reliability of the system. The numerical analysis of pressure type explosive bolt is developed to study and compare the separation behaviors of these models.

1.1 LITERATURE SURVEY

In recent years, one shot pyrotechnic actuated devices have been designed and used in many rocket, fuse and space systems. Some of them have cleanly separated without damaging the surrounding components whereas some failures have occurred during the missions due to the undesired separation time and fragmenting parts.

There are numerous technical reports and articles related to the high explosive type explosive bolts. However, only a few pressure type explosive bolts have been published. The analysis of the high explosive bolts is easier than the pressure type explosive bolts since the modeling of high explosive inside the body can be developed by using finite element analysis programs if the JWL parameters are known. However, modeling of pyrotechnics combustion involves so many complexities e.g., three-dimensionality, time-dependency, complex reaction kinetics, chocked, and non-chocked flow effects. To overcome these complexities, 0-D or 1-D time dependent internal ballistic codes have been advanced in recent studies [2]–[6]. However, they are based on NASA standard initiator actuated pin puller. The pyrotechnic combustion and pin motion can be performed for pyrotechnically actuated device without material failure. Within this framework, many performance predictions and sensitivity analyses have been developed for the pyrotechnic combustion in pin puller.

Pacheco [7] modelled and simulated a non-explosive bolt, Frangibolt shown in Figure 1. This bolt consists of a shape memory alloy (SMA) like Ni-Ti, Cu-Zn, Cu-Zn-Al, Mg-Cu, Fe-Mn-Si, Cr-Ni, actuator and heater. SMAs are a kind of metal and their shapes can change with the temperature. The mechanism of this deformation is based on thermoelastic martensitic transformations in the material. Therein, constitutive

2

models are formulated to describe this transformation. The SMAs elongate with increasing the temperature and a force that acts on the bolt body creates as a result of it. After the force reaches the critical value, the bolt separates from the notched section. In addition, the reaction of the bolt body was studied by using finite element analysis method in ANSYS. Even if the Frangibolt enables non-destructive and repeating test without creating shock wave, its response time is not instantaneous like pyrotechnic ones and also the phase temperature transformation should not exceed 120 °C for clean and successful separation.
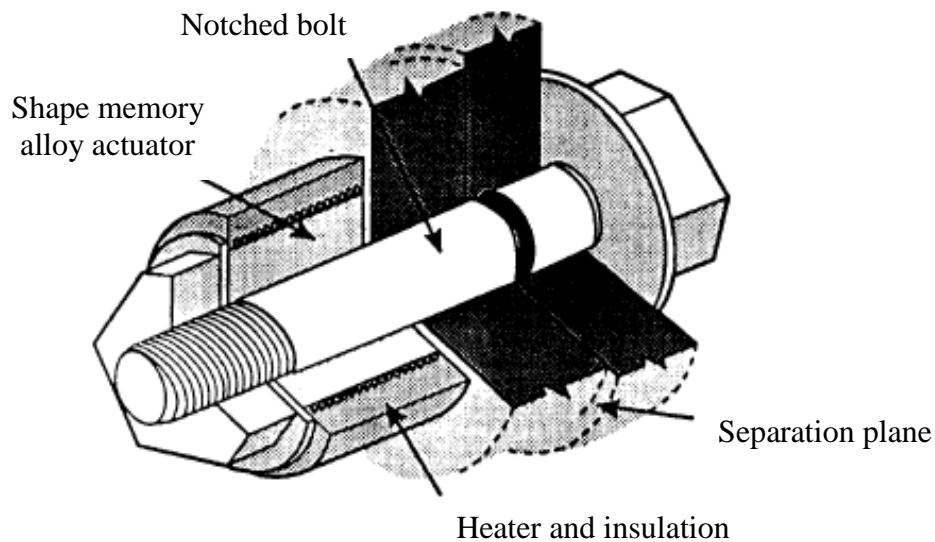
Figure 1: Frangibolt separates from notch section on the separation plane with the creating force resultant of heated Shape Memory Alloy Actuator [7].

Lee [8] simulated the performance of a ridge-cut high explosive bolts by using CTH, a hydro-code, developed by Sandia National Laboratory. The functionality of this bolt depends on the essential design parameters such as ridge shape, depth, location of the detonation charge output. Before determining these design parameters, CTH was utilized by using the detonation of the detonator and structural response of the body. After that, design parameters were determined to increase the reliability of the modeling explosive bolt design shown in

Figure 2. CTH, a kind of Eularian finite difference code, was characterized by changing the installed load on the body, the weight of RDX (Hexogen) and Lead azide and notch location. The code uses on the JWL (Jones-Wilkins-Lee) equation [9] to model the detonation, Mie-Gruiesen equation to identify equation of state for material and Johnson Cook material model [10] to set up the material model. The created model was verified with tests and it becomes useful tool to analyze the fracture mechanisms of the ridge cut explosive bolts.
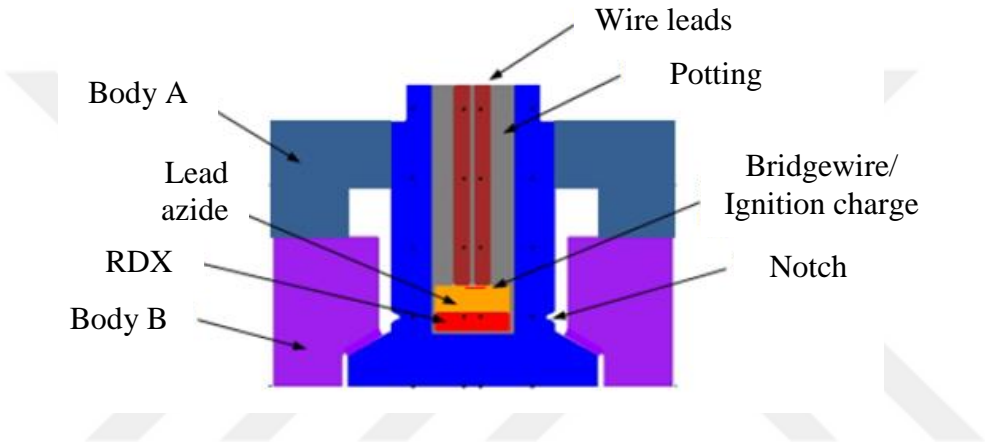
Figure 2: The given cross-sectional view of ridge-cut explosive bolts contains high explosives as RDX and Lead Azide. They are activated after igniting the charge [8].

Han [11] studied separation behavior of a ridge-cut explosive bolt, which separates because of detonation of high explosives PETN and RDX. Several gap distances (0.00, 0.02, 0.05, 0.07 and 0.30 mm) shown in Figure 3 between the bolt body and fixture were analyzed to get high reliability by using AUTODYN. Firstly, the geometric modeling and meshing procedure were defined at ANSYS Workbench Explicit Dynamics and then, this creating model was imported to AUTODYN. Johnson-Cook model [10] was used for the bolt body material, 17-4PH stainless steel. The high explosive section was implemented by using the JWL Equations [9]. The critical value of the tensile stress to simulate the failure was determined by using different reference works related to the ridge-cut explosive bolts. As a result of this study, the analysis shows that the gap distance smaller than 0.07 mm causes collision between the body and fixture and also, the magnitude of release waves decreases because of it. In this

4

way, the separation characteristic of ridge-cut explosive bolts was established with analysis.

(a)

(b)
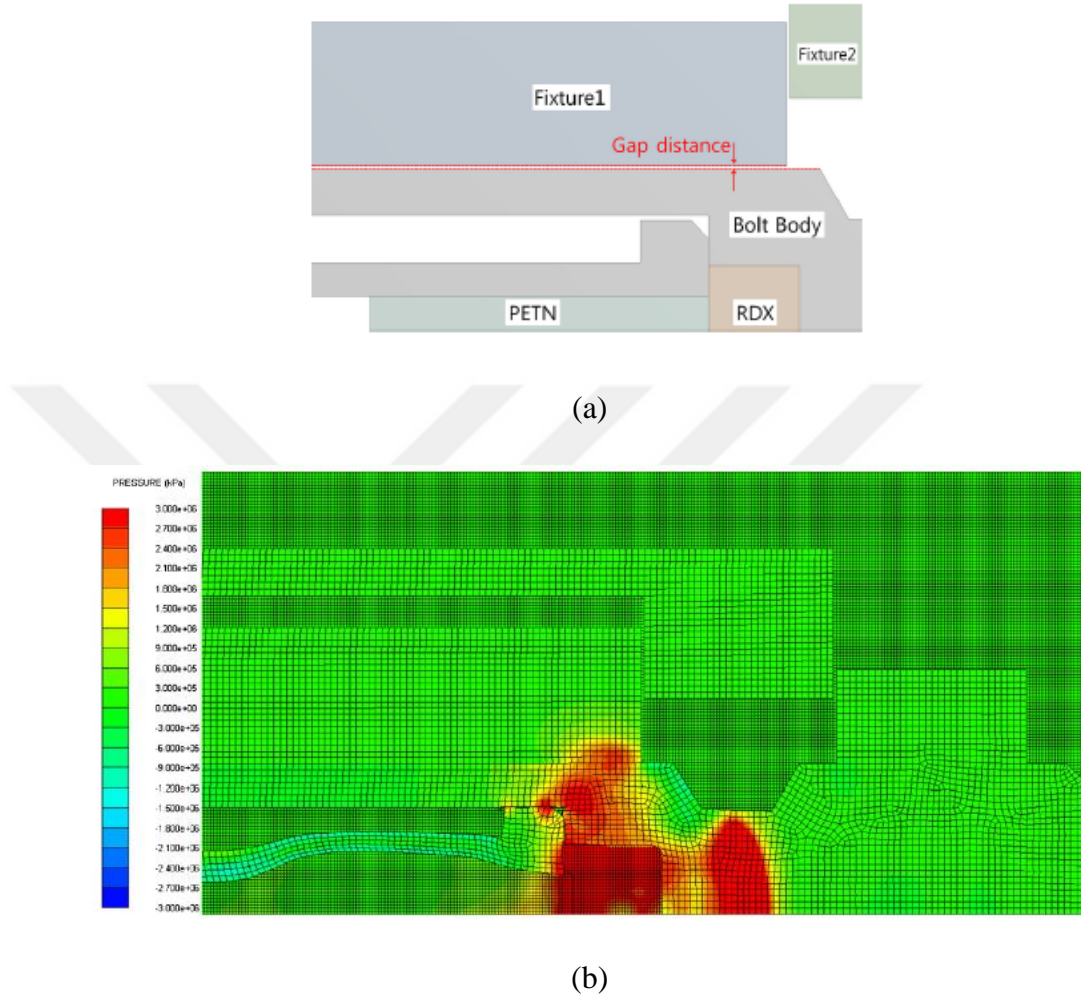
Figure 3: The gap distance shown in part (a) is a critical parameter for the separation characteristics of the bolt body. In part (b), the collision of the bodies was observed [11].

Pyroshock generations in high explosive type explosive bolts can cause failures including cracks and fractures in crystals, ceramics, epoxies, glass envelopes, solder joints and wire leads, seal failure, migration of contaminating particles, relay and switch chatter and transfer of state, deformation of very small lightweight structural elements, such as microelectronics [12]. Lee [13] developed a numerical method to analyze and predict the pyroshock propagation on the ridge-cut explosive bolts. He

used ANSYS AUTODYN as a commercial hydrocode within this scope. The reformed numerical model can control the fluid structure interactions. Also, material models were used to simulate the detonation with shock wave propagation for high explosives and stress wave propagation for body material. However, the critical point of the analyses is that velocities were taken from the gauge points on the hydrocode. These results were compared with the experimental pyroshock measurement performed by using Laser Doppler Vibrometers at the system in Figure 4. As a result of this study, the phenomenon of the pyroshock was understood and some design parameters were obtained to decrease the level of it. In this way, the reliability of the release devices containing the explosives can be enhanced.
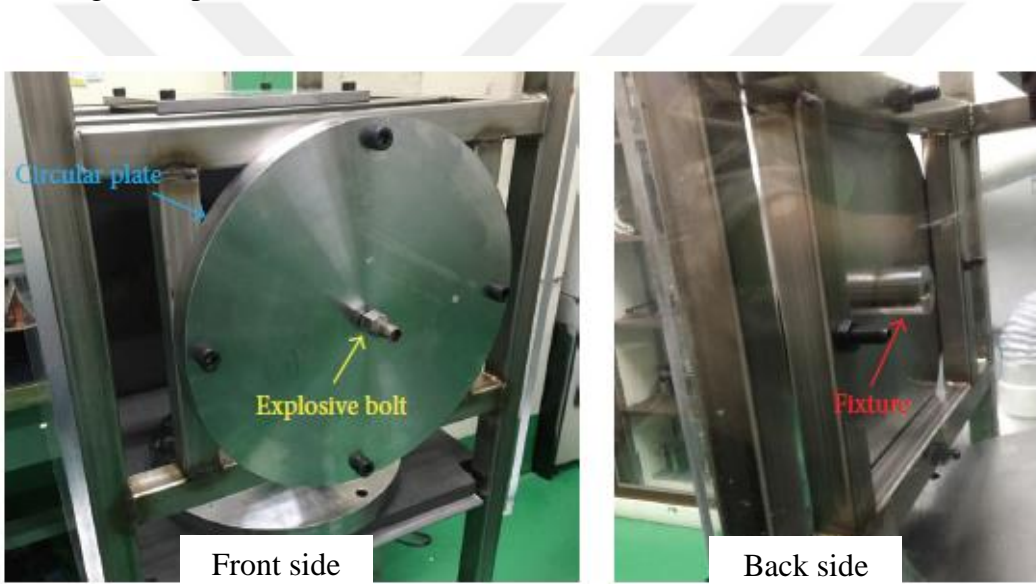
Figure 4: The experimental setup is used to measure the effects of pyroshock on the fixture during the ignition and separation of the explosive bolt. Shock transmission and propagation can be measured with Laser Doppler Vibrometers to compare the analysis and experimental results [13].

Dae-Hyun, Juho and Jae-Hung [14] performed a numerical study on a ball-type separation bolt in 2016. This bolt is a pressure type explosive bolt and it does not generate any fragments like in the pressure type explosive bolts. In this study, firstly, a simplified one-dimensional mathematical model was established. This model consisted of a simple combustion part for the initiator and 5–stages differential

equations of motions for the piston movement as shown in Figure 5. The combustion model used mass generation quantity for both gas and non-ideal gas products. Then, the history of the pressure coming from mathematical model was imported to AUTODYN.

Figure 5: The separation of the ball-type explosive bolts can be realized in five stages. At the first stages, the initiator is electrically ignited and consequently, the gas flows through the piston and shear pin breaks after reaching the critical value at Stage 2. After a while, at Stage 3, the balls between the bolt body and piston drop into the piston and finally, the separation starts with the collision of the piston and bolt body [14].

1.2 SCOPE OF THE THESIS

Explosive bolts, a kind of one-shot device, are used where mission-critical function is needed and they cannot be used for second mission. Failure of the explosive bolts can lead to missile separation failures. Therefore, it should have very high reliability level.

The purpose of this study is to improve the reliability of pressure or pyrotechnic explosive bolt for release systems. According to NASA Standard, NASA-SD-8729.1A [15], reliability is that the probability that an item will perform its intended function for a specified interval under stated conditions. The clean separation without creating fragmented parts, minimum dissipation of energy during the combustion and separation mechanisms are the main criteria in attaining higher reliability. For a given objective, three different shape piston models are developed. The varied separation behaviors can be observed since stress concentrations on the separated section of the bolt body can change for these models. Also, an analysis procedure is developed in two steps to simulate the separation of the developed models with different piston geometries.

In the first step, pyrotechnic combustion analysis is studied. A 0-D ballistic solver is developed and used to simulate the performance of the initiator until the piston impacted to the bolt body. This solver is based on the multi-phase flow theory to account incompressible solid pyrotechnics reactants, incompressible condensed phase and gas phase products. After prediction of the performance of the initiator, the predicted pressure is validated with closed bomb experiment. In this experiment, the pressure data is collected by using data gathering system. This closed bomb is a version of the pyrotechnic explosive bolt to simulate the expansion chamber with piston without failure and separation.

In the second step of the multi-disciplinary procedure, a numerical analysis is developed to simulate the separation of these different configurations in LS-DYNA. To simulate the expansion chamber of the explosive bolt in LS-DYNA, the pressure history data coming from the pyrotechnic combustion analysis in the first step are

predefined on the front area of piston and the velocity at the impact time is defined as initial velocity.

Finally, the separation time, stress concentration at the separation section, the velocity of the separated part of the bolt body and shape of the separation section are compared to provide better design for three models.

1.3   CONTENT OF THE THESIS REPORT

In Chapter 2, information about the developed pressure type of explosive bolt is presented. Firstly, the details of subparts of the explosive bolts are given. Secondly, the operation or working principles are described to understand the combustion and separation behaviors.   Finally, the analysis methodology to solve the problem is discussed.

Chapter 3 is based on the first step of the analysis procedure. In this part, modeling approaches and assumptions for the preliminary model are defined to develop pyrotechnic combustion model. The governing equations which describe the physics of a pyrotechnic combustion are specified. Then, these equations are simplified with some mathematical reductions. As a result, the final form of the pyrotechnic combustion model is constituted. The closed bomb tests are performed in order to validate the pyrotechnic combustion model.

In Chapter 4, the second and final step of the numerical analysis that is performed in LS-DYNA is described. Before creating the analysis model, the basic concepts and analysis methodology used in analysis are defined. According to that background and analyses at the literature, the analysis parameters are defined with initial and boundary conditions.

In Chapter 5, three distinct piston models, which are developed and defined in Chapter 3, are analyzed in LS-DYNA and their failure behaviors are compared. The velocity and internal energy of the different sections of each explosive bolts are compared with each other. Also, the stress and plastic strain parameters are analyzed to understand the different separation behavior at the proposed models.

CHAPTER 2

MODELING OF THE PROBLEM

2.1 MODEL DESCRIPTION

The present cross-sectional geometry depicted in Figure 6 is a kind of non-fragmenting and pressure type explosive bolt that has three main sub-parts; a pyrotechnic initiator, piston and a bolt body, respectively. This pressure type explosive bolt, having a M5 threaded part at the front of the body, is capable of carrying 6000 N in tensile direction. It is used for tank separation, rocket sled release, thrust termination and separation of the parts/caps at the fuse systems. As a matter of fact, a couple of higher threaded type bolt like M16 can be used in the stage separation of the multistage systems.
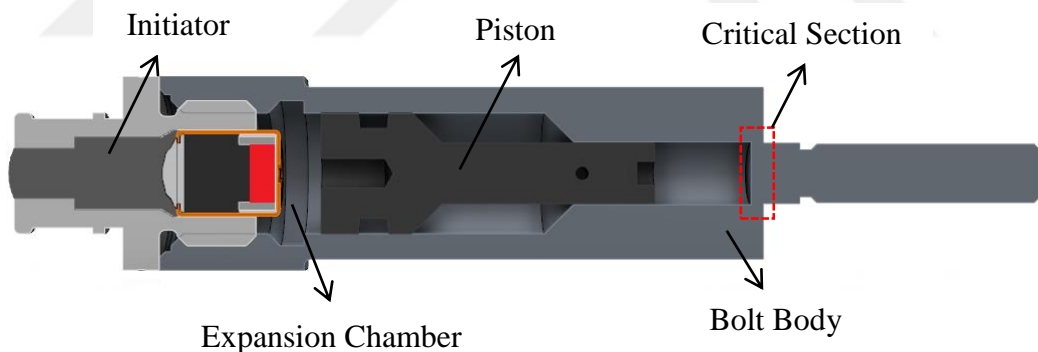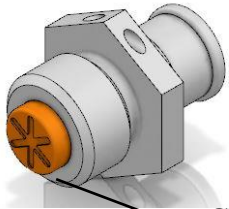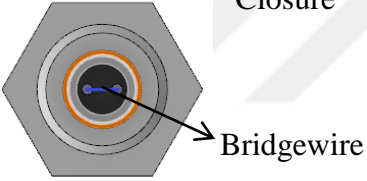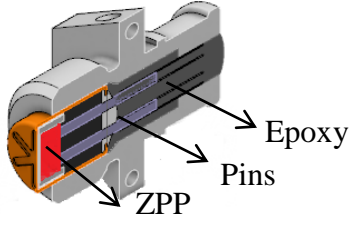
Figure 6: Non-fragmenting pressure type explosive bolt

The NSI was originally developed as an initiator to ignite the igniter charge in the solid rocket motors. In the process of time, it has been adapted for the pyrotechnic actuated devices, such as pin puller, cable cutter and explosive bots. It is composed of a glass to metal seal body that contains an electrical header with two pins, 114 milligrams propellant mix of Zirconium/Potassium Perchlorate as pyrotechnic charge; a 50 micrometer diameter of the stainless steel 304 bridgewire to electrically ignite the pyrotechnic charge; an epoxy for the housing of the charge; a washer and disk to

11

insulate the charge and a cap to prevent the aging and get better performance. Bridgewire resistance is between 0.95 and 1.15 ohm and it can be ignited by applying 3.5 Ampere throughout 50 milliseconds between two pins at the electrical header [16].

The pyrotechnic initiator in this model is very similar to the NSI. The main component of this initiator is a squib. It consists of the electrical header in form of an epoxy mixture with two pins, the pyrotechnic charge, bridgewire and closure disk for the insulation. The detailed specifications for this initiator are given in Table 1.

Table 1: Specifications of the initiator used in the model

Cup, Closure Bridgewire Epoxy Pins ZPP	Bridge-wire: • Diameter: 50 μm • Material: Nickel-chromium alloy
	Pyrotechnical specifications: • 100 milligrams Zirconium/Potassium Perchlorate • ZPP is composed of; - Zirconium (Zr) as fuel - Potassium Perchlorate as oxidizer
	Electrical specifications: • Resistance: 1.1±0.1 ohm • Firing current: 3.5 Ampere - 50 milliseconds

The focus of this study is to present the separation characteristics for different contact region between the piston and bolt body. Three different piston models shown in Figure 7 are designed within this scope. The different section at the end of the piston can affect the separation behavior of the bolt such as separation time, velocity of the separated part and cleanliness of the separation plane or surface. Here, the main reason is that the stress concentrations can change at the critical section as shown in Figure 6

12

for different contact regions. The pressure into the expansion chamber is transmitted as a force by the piston. If this force is as far as possible applied to the critical region on the body, the separation should become easier. Moreover, the deformation of the piston should be minimized to use high energy for the separation. Therefore, 17-4 PH stainless steel, which has high tensile strength, is chosen as the material of the body. The seal interface is formed on the piston to prevent the passing over the ignition products and a hole is modeled on the piston for stabilizing the piston during the non-working operations such as transportation of the system.

a) Piston-1
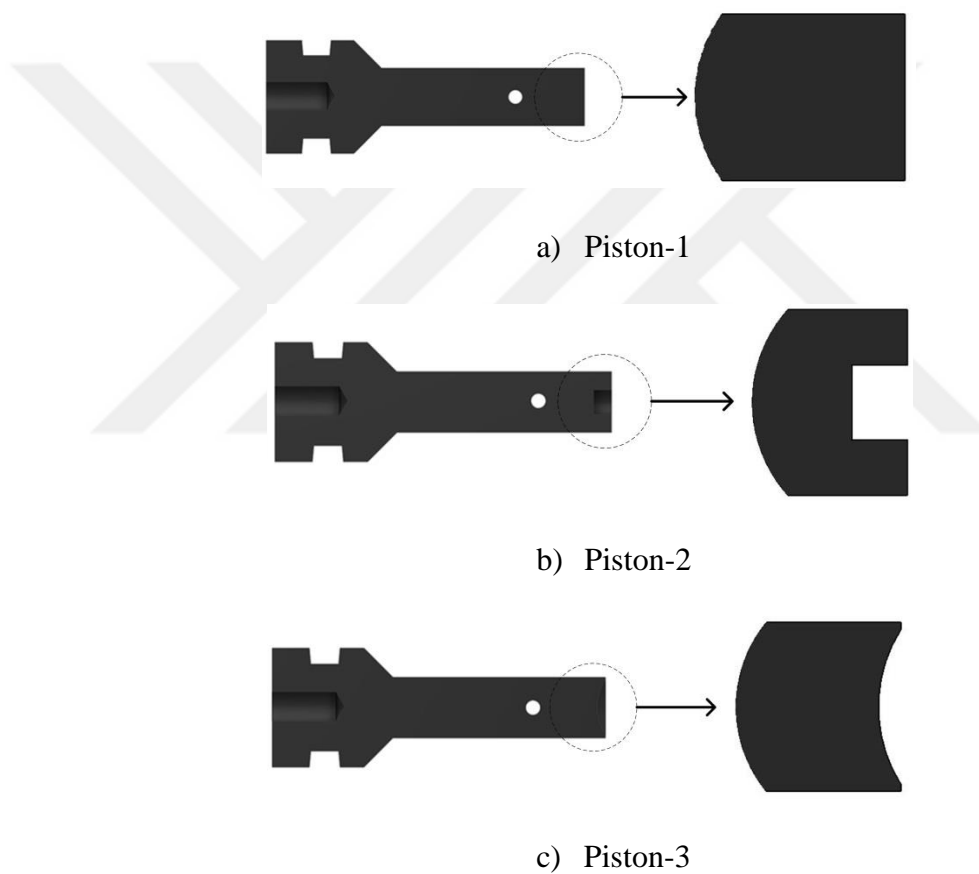
b) Piston-2

c) Piston-3

Figure 7: Piston-1 has a circular cross sectional area while Piston-2 has a hole and Piston-3 has a dome shape at the end of the piston.

The bolt body that has an effect on the separation characteristics of the explosive bolt is another component. This part must fulfill a requirement as carrying some amount of force before the separation and also, it must cleanly separate to accomplish its mission

under this loading. The bolt starts to separate from the weakened parts of the bolt body shown in Figure 8. Therefore, the most critical design parameter at that point is the thickness of that part. The material of the body is preferred as 4340 Steel due to the separation and defined requirements in beginning of the model description.
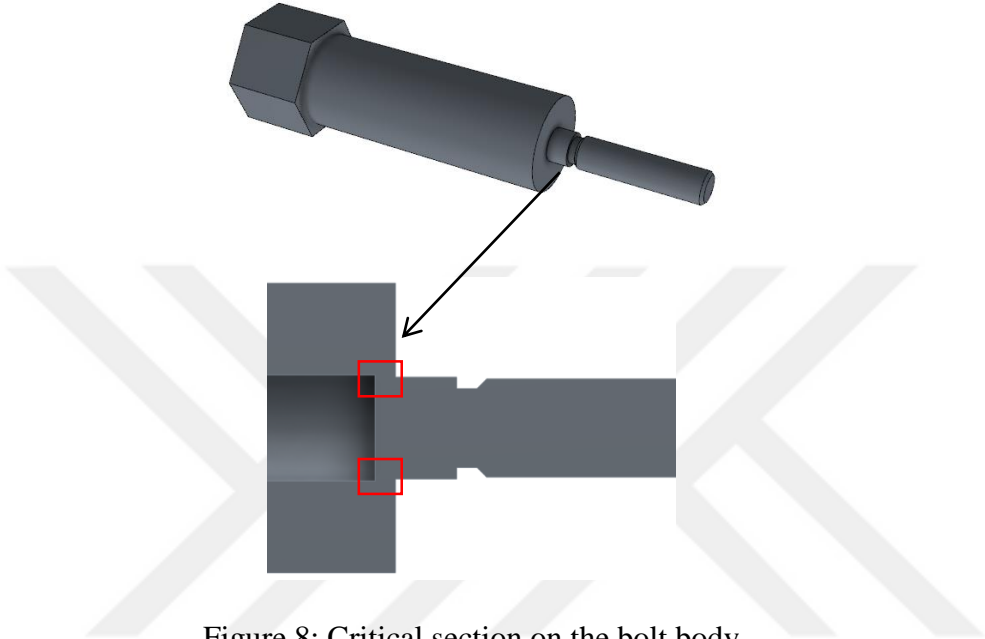
Figure 8: Critical section on the bolt body

2.2 WORKING PRINCIPLE

The working of explosive bolt can be divided and observed in four steps as shown in Figure 9. The first one is the activation of the pyrotechnic charge inside the initiator. The bridgewire positioned between two pins on the initiator underlies the charge and heats when applying the current between these two pins. As a result of this electrical to thermal energy transfer, the temperature of the bridgewire reaches critical value to ignite ZPP. Before tearing the capture, condensed and gas phase products are generated with rapid chemical reaction and they start to constitute a pressure inside the cavity. After tearing the capture of the squib, the particles in ZPP and some products of the ignition reaction continue to react at the expansion chamber of the bolt. The shear pin on the piston brakes when an enough force creates to failure. After that, the second step starts with the motion of the piston. Until the piston crashes to the critical section of the bolt body, the pressure continues increasing at the expansion chamber in spite

14

of increasing of this chamber volume. During the third step of the work, the bolt body undergoes dynamic material failure with a high impact load between the piston and body. After the stresses at the separation part reach the critical value, the threaded part on the bolt starts to separate without any forming fragmenting parts.
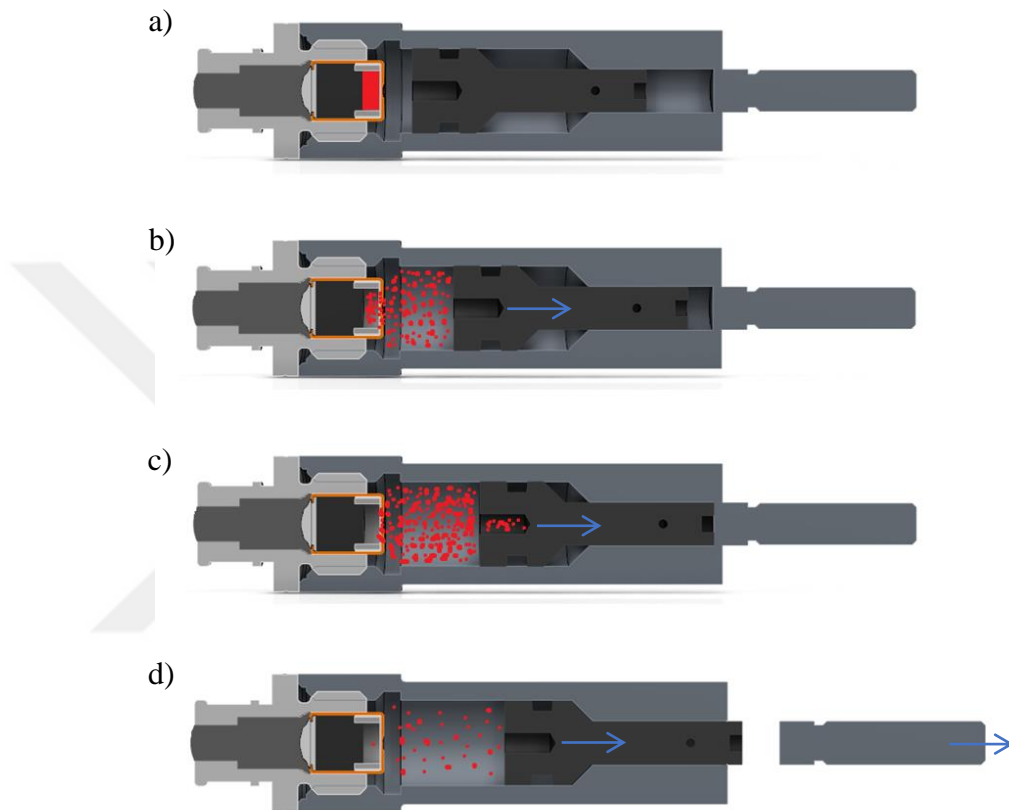
Figure 9: The first figure shows the combustion of the pyrotechnic. The initiator is electrically ignited and it starts to create pressure inside the cap. After tearing the closure of the initiator, the condensed and gas phase products go through into the expansion chamber like in the second figure. Last two figures represent the separation period.

2.3   ANALYSIS METHODOLOGY

In this study, the performed numerical analysis to simulate the separation of the explosive bolt is composed of two different parts as shown in Figure 10. The first part is the pyrotechnic combustion to predict the performance of the initiator. The second

part is the finite element analysis to simulate the separation of the pyrotechnic explosive bolt.
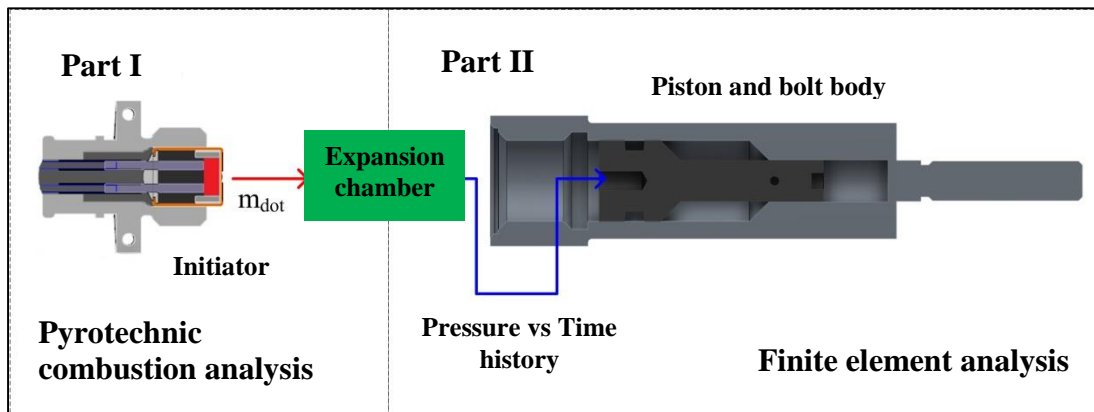
Figure 10: Pyrotechnic combustion analysis part is based on the ignition of the initiator at the expansion chamber. As a result of this numerical analysis, a change of the pressure at the chamber and the velocity of the piston are gained with respect to time. The pressure and velocity histories are applied on the front of the piston area and piston to simulate the separation in the finite element analysis part, respectively.

Pyrotechnic combustion flow chart of which is shown in Figure 11 simulates the ignition of the initiator at the expansion chamber of the explosive bolt. During the ignition, the condensed and gas phased particles are generated as a result of the chemical reaction of solid pyrotechnic ZPP. These high pressure products cause the failure of the shear pin. Up to that point, the mass flow rate and pressure inside the expansion chamber are calculated at the constant volume. After the movement of the piston, they are calculated with the position and velocity of the piston by considering the variable volume. Then, the volume is a constant when the piston crashes to the body. The combustion analysis continues until the desired function time of the explosive bolts. Moreover, the pressure-time history data gained from the combustion analysis is validated with the closed bomb tests. The pressure data are collected in these tests by a data acquisition system.
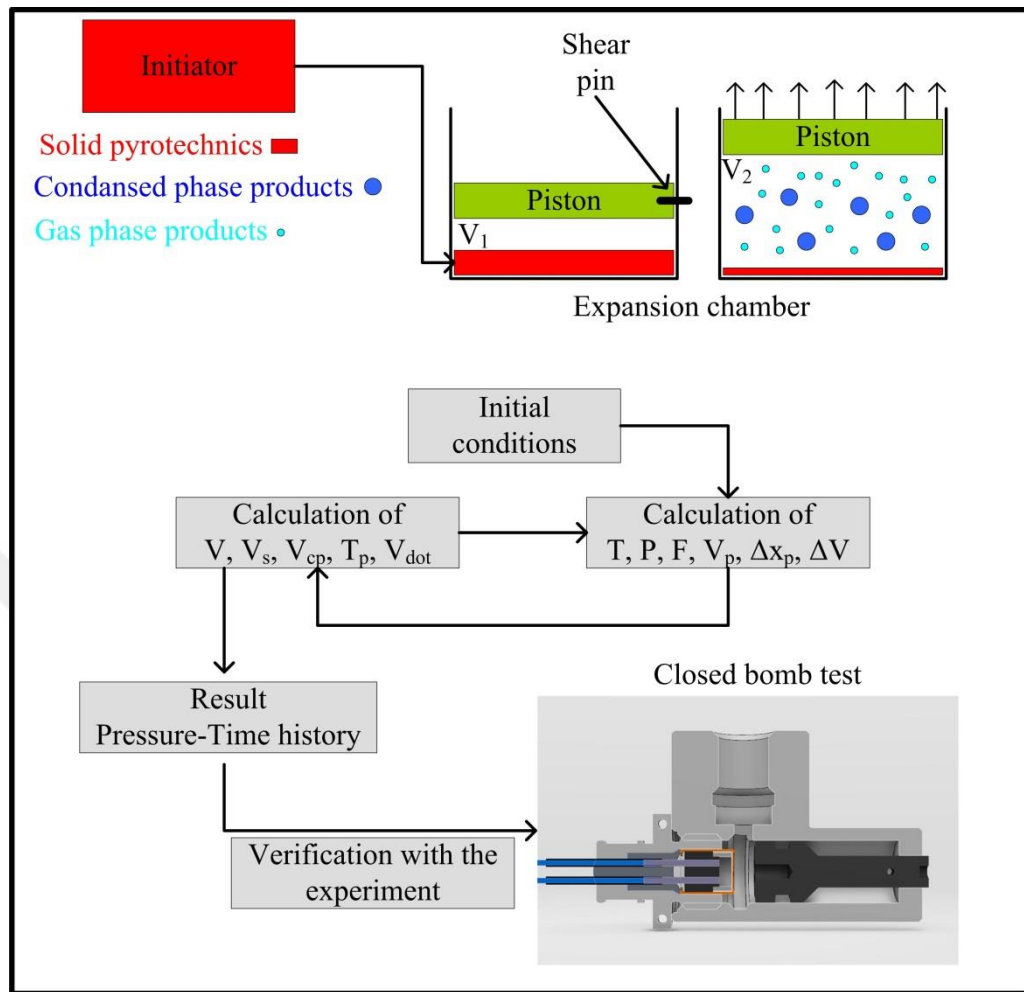
Figure 11: Flow chart of the pyrotechnic combustion analysis part

In the finite element analysis part, failure analyses are established to simulate the separation of the explosive bolts. Firstly, the geometrical modeling is prepared by using ANSYS Workbench and Design Modeler. Then, this model is imported to LS-DYNA to simulate the failure of the explosive bolt. Here, the pressure-time and velocity-time history data in the pyrotechnic combustion analysis part are defined on the front of the piston surface and piston, respectively. Also, the gauge points are defined at the separated part, piston and bolt body to observe the stresses, velocities and separation times. This procedure is performed for each three distinct models. Then, these data are compared to establish the differences between three piston models for higher reliability.

CHAPTER 3

PYROTECHNIC COMBUSTION MODEL

3.1 MODELING APPROACH

The pyrotechnic combustion driven system described in article [3] is taken as a reference work with some modifications for this study. This system is developed by considering the multiphase flow theory [17], because three different phases, that are solid pyrotechnic reactants, gas and condensed phase products, can occur during the ignition of the pyrotechnics. Therefore, the system is modeled by using these subsystems as shown in Figure 12. The conservation of mass and energy for these subsystems and newton second law for the motion of the piston are used to model the ballistic part of the problem with initial and boundary conditions.
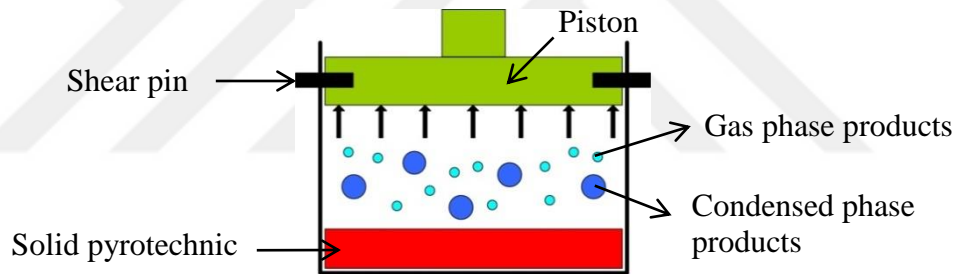
Figure 12: Modeling of the ballistic problem

The ballistic model presented in this section has different programming methodology, solver for derived first-order ordinary differential equations come from the conservation of mass and energy with Newton's second law and used thermochemistry data for ZPP than the reference model.

3.2 ASSUMPTIONS

Before deriving the differential equations from the governing equations, the following simplifying assumptions are made:

o Burning area of the solid pyrotechnic (ZPP) is assumed to be equal to the area of the front surface of piston.

o The solid pyrotechnic mass is a time dependent quantity.

o The condensed and gas phase products are generated with the ignition of ZPP and they are modeled separately as condensed and gas phase parts.

o The shear pin is broken as a result of the expansion work which is created by gas phase products.

o The friction force between the body and piston is neglected.

o Burn rate of ZPP is calculated with respect to Equation (11).

o The combustion products are assumed to be an ideal gas.

o The specific heats of the combustion products can be obtained via term by term fourth order polynomial function that depends on the temperature. These specific heat constants are taken from the equilibrium thermochemistry code CET93 [18] and BURCAT [19]. Then, they are integrated to the pyrotechnic combustion model.

o ICT [20], thermochemistry program, is used to estimate the mole fraction of the combustion products with ignition of 5 gr ZPP at 200 cc constant volume.

o The heat transfer rate between the gas and condensed phase products is assumed to be sufficiently high. Therefore, their temperatures are assumed to be equal.

o The effect of the shear pin on the system is assumed to fix the piston up to release. There isn't any other effect on the motion of the piston.

o Heat transfer from the body wall to the surrounding (through the expansion chamber) is assumed to be formed in convective and radiation.

o The internal energy of the solid pyrotechnic is assumed to be a constant.

o It is assumed that there is not any mass exchange between the total system and surroundings.

o It is assumed that there is not any work exchange between the subsystems like between gas and condensed phase products or gas phase products and solid pyrotechnic.

3.3   GOVERNING EQUATIONS

The conservation equations can be written for each system by taking the multi-phase flow theory [17] into consideration. Mass evolution equation for the solid pyrotechnics contained in the initiator and expansion chamber is given by

$$\frac{d}{dt}(\rho_s V_s) = -\rho_s A_p r, \tag{1}$$

where the subscript "s" is used to label quantities associated with the solid pyrotechnics. Therein, the independent variable is time t and cross section area of the piston A_p whereas dependent variables are the solid particle volume V_s and the pyrotechnic burn rate r. The solid pyrotechnics density ρ_s is assumed to be constant.

At the assumption part, mass exchange can be defined as from reactants to gas and condensed phase products. Therefore, mass evolution equation for the condensed phase products can be defined as

$$\frac{d}{dt}(\rho_{cp} V_{cp}) = \eta_{cp}\rho_s A_p r. \tag{2}$$

Therein, it can be calculated from the reactant of solid pyrotechnic with multiplied mass fraction of products in the condensed phase η_{cp}. The subscript "cp" is used to label quantities associated with the condensed phase products. The independent variable is time t whereas dependent variables are the solid particle volume V_{cp} and the pyrotechnic burn rate r. The condensed phase density ρ_{cp} is assumed to be constant.

Similarly, for the gas phase products, mass evolution equation can be expressed

$$\frac{d}{dt}(\rho_g V_g) = (1 - \eta_{cp})\rho_s A_p r, \tag{3}$$

where the subscript "g" is used to label quantities associated with the gas phase products. Therein, the independent variable is time t whereas dependent variables are the gas phase products density ρ_g; the volume V_g and the pyrotechnic burn rate r.

Energy evolution equation for the solid pyrotechnics,

$$\frac{d}{dt}(\rho_s V_s e_s) = -\rho_s A_p e_s r, \tag{4}$$

can be found by multiplying the mass evolution equation with an another dependent variable, its specific internal energy or caloric equations of state e_s.

In the system, the heat transfer can occur during the combustion of solid pyrotechnics in two ways: from the condensed to gas phase products and from surrounding to condensed phase products, as later indicated in Figure 13. With this knowledge, the energy evolution equation for the condensed phase products can be described as

$$\frac{d}{dt}(\rho_{cp} V_{cp} e_{cp}) = \eta_{cp} \rho_s A_p e_s r - \dot{Q}_{cp,g} + \dot{Q}_{cp}. \tag{5}$$

Therein, dependent variables different from Equation (2) are the specific internal energy of condensed phase products e_{cp}; heat transfer rates from the condensed to gas phase products $\dot{Q}_{cp,g}$ and from surroundings to condensed phase products $\dot{Q}_{cp}$.

When considering the energy transfer for gas phase products, there is one extra relation different from the condensed one. It is the work rate done by gas phase products inside the expansion chamber. For the gas phase products,

$$\frac{d}{dt}(\rho_g V_g e_g) = (1 - \eta_{cp})\rho_s A_p e_s r + \dot{Q}_{cp,g} + \dot{Q}_g - \dot{W}_g \tag{6}$$

can be used as energy evolution equation. Therein, e_g represents the specific internal energy for gas phase products; $\dot{Q}_g$ represents the heat transfer rates from the surroundings to gas phase products and $\dot{W}_g$ is the rate of work done by the gas phase products in moving the pin.

Equation of motion for the piston can be defined by using the Newton's second law. For one dimensional linear motion, it can be defined as

$$m_p \frac{d^2 z_p}{dt^2} = F_p. \tag{7}$$

Therein, the piston position z_p and net force on the piston F_p are the other dependent variables. Besides, the mass of the piston m_p is a constant parameter.

To close the equations for mass and energy release principles, geometrical and constitutive relations should be used. Therefore, the total volume of the system V and the position of the piston z_p can be used as a geometrical constrain. The volume of the system can be calculated from the mixture theory principles, i.e.

$$V = V_s + V_{cp} + V_g. \tag{8}$$

The position of piston

$$z_p = \frac{V}{A_p} \tag{9}$$

can be expressed as by using the cross-section area of the piston A_p and total volume defined in Equation (8).

According to the ideal gas assumption, the pressure which develops with the gas phase products should be defined such that

$$P_g = \rho_g R T_g. \tag{10}$$

Therein, ρ_g represents the gas phase density; T_g represents gas phase temperature and R is ideal gas constant.

As commonly done in pyrotechnic combustion modeling, the burning rate

$$r = r[P_g] = bP_g^n, \tag{11}$$

that is dependent to the gas phase pressure, can be modeled as a linear pyrotechnic burn rate. Therein, b and n are burning constants whose values can change with type of pyrotechnics at the system. During the modeling of the pyrotechnic combustion, brackets [ ] are used to denote a functional dependence on the enclosed variable. It can be used as the constitutive relations for deriving the gas phase products density ρ_g.

An important, yet undefined, the internal energies per unit mass of the solid pyrotechnic, condensed and gas phase products are changed with their temperatures. Since there are a lot of solid particles, condensed and gas phase products during the ignition, the caloric equations of the states, namely specific internal energies, can be get from the summation operator as

$$e_s[T_s] = \sum_{i=1}^{N_s} Y_{s_i} e_{s_i}[T_s] \tag{12}$$

for solid pyrotechnics,

$$e_{cp}[T_{cp}] = \sum_{i=1}^{N_{cp}} Y_{cp_i} e_{cp_i}[T_{cp}] \tag{13}$$

for condensed phase products and

$$e_g[T_g] = \sum_{i=1}^{N_g} Y_{g_i} e_{g_i}[T_g] \tag{14}$$

for gas phase products.

Therein, $Y_{s_i}, Y_{cp_i}, Y_{g_i}, N_s, N_{cp}$ and N_g are the constant mass fractions and number of components species of three subsystems while the subscript i shows the individual species.

Since the internal energy is a function of temperature as indicated in Equations (12-14), the specific heat at constant volume should be taken in consideration instead of

24

one at constant pressure. Then, the specific heats at the constant volume of the reactants and products can be calculated

$$c_{v_s}[T_s] = \sum_{i=1}^{N_s} Y_{s_i} \frac{d}{dT_s}(e_{s_i}[T_s]), \tag{15}$$

$$c_{v_{cp}}[T_{cp}] = \sum_{i=1}^{N_{cp}} Y_{cp_i} \frac{d}{dT_{cp}}(e_{cp_i}[T_{cp}]), \tag{16}$$

$$c_{v_g}[T_g] = \sum_{i=1}^{N_g} Y_{g_i} \frac{d}{dT_g}(e_{g_i}[T_g]), \tag{17}$$

by taking derivative of these caloric equations with respect to time. Since, the internal energy per unit mass is dependent on the temperature, the specific heat also changes with temperature. Therein, $Y_{s_i}, Y_{cp_i}, Y_{g_i}, N_s, N_{cp}$ and N_g are the same parameters with defined in Equations (12-14).

The following heat transfer equation,

$$\dot{Q}_{cp,g}[T_{cp}, T_g] = h_{cp,g} A_{cp}(T_{cp} - T_g), \tag{18}$$

represents the heat loss from the condensed phase to gas phase products inside the expansion. Also, $\dot{Q}_{cp}$ represents the heat transfer between the surrounding and condensed phase products and $\dot{Q}_g$ represents the heat transfer between the surrounding and gas phase products as shown in Figure 13.
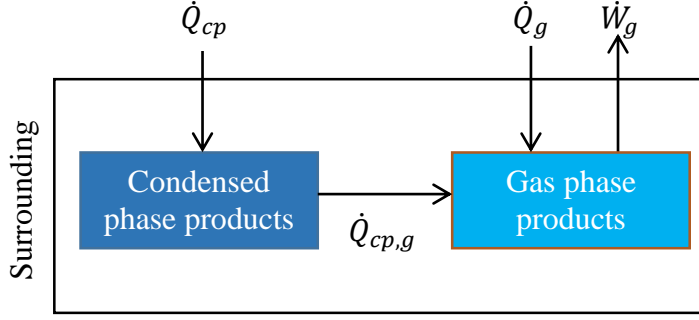
Figure 13: The heat transfers in the system

The ignition of pyrotechnics completes in order of the milliseconds in the pyrotechnic actuated devices like pyrotechnic explosive bolt. The chemical reactions of these energetic materials are highly exothermic during the ignition and therefore, the temperatures of condensed and gas phased products are significantly higher than the ambient temperature [3]. As a result of this large heat transfer rate, the temperature of the condensed and gas phased products can be taken as equal to each other and it can be defined as temperature of products T_p. In this case, $\dot{Q}_{cp}$ goes to zero and therefore, the heat transfer between the condensed and gas phase products can be neglected. Hereby,

$$\dot{Q}_{cp} = \dot{Q}_{cp}[V, V_s, T_{cp}] \tag{19}$$

$$\dot{Q}_g = \dot{Q}_g[V, V_s, T_g] \tag{20}$$

$$
\begin{aligned}
\dot{Q}_p[V, V_s, T_p] &= \dot{Q}_{cp}[V, V_s, T_p] + \dot{Q}_g[V, V_s, T_p] \\
&= hA_w[V, V_s](T_w - T_p) \\
&\quad + \sigma A_w[V, V_s](\alpha T_w^4 - \varepsilon T_p^4)
\end{aligned} \tag{21}
$$

can be used for the rate of heat transfer between the surrounding and combustion products. It consists of the convective and radiative heat transfer between the inside wall of the bolt body. This section changes with the movement of the piston. Therein, the constant parameters are convective heat transfer coefficient h, temperature of the

26

bolt body wall T_w, Stefan-Boltzman constant σ, absorptivity of the bolt body α and the net emissivity of the product mixture ε. Besides,

$$A_w[V, V_s] = 2\sqrt{(\pi/A_p)(V - V_s)} \tag{22}$$

represents an instantaneous surface area between the bolt body and piston.

After the ignition of the initiator, the force on the piston can be calculated based on two conditions,

$$F_p = 0 \; if \; P_g A_p < F_{crit}; \; F_p = P_g A_p \; if \; P_g A_p \geq F_{crit}. \tag{22}$$

After the movement of the piston, the pressure-volume work

$$\dot{W}_g = P_g \frac{dV}{dt}, \tag{24}$$

which is generated by the expanding gas phase products, can be modeled.

3.4   MATHEMATICAL MODEL

After defining the equations at the previous section, the derived differential equations can be reduced to form a final model of the ballistic formulation that contains a set of first order differential equations. Before the reduction step, time derivative of the expansion chamber volume can be defined

$$\dot{V} = \frac{dV}{dt}. \tag{25}$$

First, Equations (1-3) can be added and defined as the conservation of the combined systems

$$\frac{d}{dt}(\rho_s V_s + \rho_{cp} V_{cp} + \rho_g V_g) = 0. \tag{26}$$

Therein, the density of the solid particles and condensed phase products are constant and they cannot be affected from the change of the volume. However, the density of the gas phase products change with the movement of the piston.

Equation (26) can be integrated by applying the initial conditions which are denoted by the subscript "0". The volume of the gas phase products, V_g, can be defined in terms of V, V_s and V_{cp} by using Equation (8). Then, ρ_g can be calculated as follows

$$\rho_g[V, V_s, V_{cp}] = \frac{\rho_s V_{s0} + \rho_{cp} V_{cp0} + \rho_{g0} V_{g0} - \rho_s V_s - \rho_{cp} V_{cp}}{V - V_s - V_{cp}}. \tag{27}$$

Thermal equation of gas phase products or gas phase pressure,

$$P_g[V, V_s, V_{cp}, T_p] = \rho_g[V, V_s, V_{cp}]RT_p, \tag{28}$$

can be expressed by using Equation (27) as a function of V, V_s, V_{cp}, T_p.

After defining P_g, the burn rate,

$$r = r[V, V_s, V_{cp}, T_p] = bP_g^n[V, V_s, V_{cp}, T_p], \tag{29}$$

can be defined as a function of V, V_s, V_{cp}, T_p by using the Equation (28).

The force on the piston due to gas phase pressure,

$$F_p = F_P[V, V_s, V_{cp}, T_p], \tag{30}$$

can also be expressed as a function of V, V_s, V_{cp}, T_p by using the Equation (28).

The mass evolution equation of the solid particles can be redefined

$$\frac{dV_s}{dt} = -A_p r[V, V_s, V_{cp}, T_p] \tag{31}$$

by taking consideration of the assumption of the constant density and burn rate definition in Equation (29).

The mass evolution equation of the condensed phase products,

$$\frac{dV_{cp}}{dt} = \eta_{cp}\left(\frac{\rho_s}{\rho_{cp}}\right)A_p r[V, V_s, V_{cp}, T_p],\tag{32}$$

can be simplified like at the same manner of solid particles by considering the assumption of the constant density and burn rate definition in Equation (29).

The internal energy of the solid pyrotechnics,

$$e_s\frac{d}{dt}(\rho_s V_s) + \rho_s V_s\frac{d}{dt}(e_s) = -\rho_s A_p e_s r\tag{33}$$

$$\left\{\frac{d}{dt}(\rho_s V_s) = -\rho_s A_p r\right\}e_s\tag{34}$$

$$\frac{de_s}{dt} = 0 \rightarrow e_s = e_{s0},\tag{35}$$

is constant during the combustion with the assumption of no heat transfer to it. Therein, the derivation part of the energy evolution equation for solid particles in Equation (4) can be rendered different form as shown in Equation (33). Before simplifying, the mass evolution equation of the solid particles is multiplied with the e_s like in Equation (34). Then, the derivative of the internal energy with respect to time for solid particles can be obtained by subtracting Equation (33) and (34).

The derivative of the internal energy for the condensed phase particles with respect to time can be obtained as follows

$$e_{cp} \frac{d}{dt}(\rho_{cp} V_{cp}) + \rho_{cp} V_{cp} \frac{d}{dt}(e_{cp}) = \eta_{cp} \rho_s A_p e_s r - \dot{Q}_{cp,g} + \dot{Q}_{cp} \qquad (36)$$

$$\left\{ \frac{d}{dt}(\rho_{cp} V_{cp}) = \eta_{cp} \rho_s A_p r \right\} e_{cp} \qquad (37)$$

$$\rho_{cp} V_{cp} \frac{d}{dt}(e_{cp}) = \eta_{cp} \rho_s A_p r (e_{s0} - e_{cp}) - \dot{Q}_{cp,g} + \dot{Q}_{cp}. \qquad (38)$$

First, Equation (5) can be redefined as shown in Equation (36). Therein, the internal energy of the solid particles e_s can be taken as e_{s0} founded in Equation (35). Before subtracting, the mass evolution equation of the condensed phase products is multiplied with the e_{cp} like in Equation (34). Then, the derivative of the internal energy for the condensed phase particles with respect to time can be obtained by subtracting Equation (36) and (37).

The derivative of the internal energy for gas phase products with respect to time can be also obtained

$$e_g \frac{d}{dt}(\rho_g V_g) + \rho_g V_g \frac{d}{dt}(e_g) = (1 - \eta_{cp})\rho_s A_p e_s r + \dot{Q}_{cp,g} + \dot{Q}_g - \dot{W}_g \qquad (39)$$

$$\left\{ \frac{d}{dt}(\rho_g V_g) = (1 - \eta_{cp})\rho_s A_p r \right\} e_g \qquad (40)$$

$$\rho_g V_g \frac{d}{dt}(e_g) = (1 - \eta_{cp})\rho_s A_p r (e_{s0} - e_g) + \dot{Q}_{cp,g} + \dot{Q}_g - \dot{W}_g. \qquad (41)$$

Firstly, Equation (6) can be re-expressed like in Equation (39). Before simplifying, the mass evolution equation of the gas phase products is multiplied with the e_g as shown in Equation (40). Then, the derivative of the internal energy for the gas phase particles with respect to time can be obtained by subtracting Equation (39) and (40).

The internal energy evolution equations of combined product system,

$$\rho_{cp}V_{cp}\frac{d}{dt}(e_{cp}) + \rho_g V_g \frac{d}{dt}(e_g) = \{e_{so} - \eta_{cp}e_{cp} - (1 - \eta_{cp})e_g\}\rho_s A_p r$$

$$+ \dot{Q}_p[V, V_s, T_p] - \dot{W}_g, \qquad (42)$$

can be expressed by addition of Equation (38) and (41). Therein, the summation of $\dot{Q}_{cp}$ and $\dot{Q}_g$ variables can be defined as $\dot{Q}_p$ by using Equation (21).

The Equation (16) can be re-expressed as

$$c_{v_{cp}}[T_p] = \frac{de_{cp}[T_p]}{dT_p} \quad \rightarrow \quad \frac{de_{cp}[T_p]}{dt} = \frac{dT_p}{dt}c_{v_{cp}}[T_p]. \qquad (43)$$

Also, the Equation (17) can be expressed similarly

$$c_{v_g}[T_p] = \frac{de_g[T_p]}{dT_p} \quad \rightarrow \quad \frac{de_g[T_p]}{dt} = \frac{dT_p}{dt}c_{v_g}[T_p]. \qquad (44)$$

Then, Equation (42) can be simplified by subtracting the time derivative of internal energies in terms of T_p in Equations (43) and (44). Also, Equation (24) can be used to eliminate $\dot{W}_g$. As a result, the derivative of T_p becomes

$$\frac{dT_p}{dt} = \frac{\{e_{so} - \eta_{cp}e_{cp}[T_p] - (1 - \eta_{cp})e_g[T_p]\}\rho_s A_p r[V, V_s, V_{cp}, T_p]}{\rho_g[V, V_s, V_{cp}](V - V_s - V_{cp})c_{vg}[T_p] + \rho_{cp}V_{cp}c_{v_{cp}}[T_p]}$$

$$+ \frac{\dot{Q}_p[V, V_s, T_p] - P_g[V, V_s, V_{cp}, T_p]\dot{V}}{\rho_g(V, V_s, V_{cp})(V - V_s - V_{cp})c_{vg}[T_p] + \rho_{cp}V_{cp}c_{v_{cp}}[T_p]}. \qquad (45)$$

Lastly, the second-order ordinary differential equation for the Newton's second law governing piston motion in Equation (7) can be split into two-first order differential equations. The first one of them is defined in Equation (25). The second equation

$$\frac{d\dot{V}}{dt} = \frac{A_p}{m_p}F_p[V, V_s, V_{cp}, T_p], \qquad (46)$$

which can be derived from the equation of motion by using Equation (25), position of the piston defined in Equation (9) and force on the piston in Equation (30).

3.5 PRELIMINARY MODEL

In the previous section, some equations, which underlie the pyrotechnic combustion model, are derived to calculate the basic parameter for the combustion like burn rate and pressure. These equations can be arranged and five first order differential equations can be governed.

Within this framework, the first differential equation is the time derivative of combine system volume

$$\dot{V} = \frac{dV}{dt}. \tag{25}$$

The second differential equation in the previous section,

$$\frac{dV_s}{dt} = -A_p r[V, V_s, V_{cp}, T_p], \tag{31}$$

is the time derivative of volume of the solid pyrotechnics. Therein, the volume of solid pyrotechnic can be calculated at any time during the combustion. It changes according to the burn rate parameter defined in Equation (29).

The third differential equation at the previous section,

$$\frac{dV_{cp}}{dt} = \eta_{cp}(\frac{\rho_s}{\rho_{cp}})A_p r[V, V_s, V_{cp}, T_p], \tag{32}$$

is the time derivative of volume of the condensed phase products. Therein, the volume of the condensed phase products can be calculated at any time during the combustion. It changes according to the burn rate parameter defined in Equation (29).

Another first order differential equation in the previous section,

$$\frac{dT_p}{dt} = \frac{\{e_{so} - \eta_{cp}e_{cp}[T_p] - (1 - \eta_{cp})e_g[T_p]\}\rho_s A_p r[V, V_s, V_{cp}, T_p]}{\rho_g[V, V_s, V_{cp}](V - V_s - V_{cp})c_{vg}[T_p] + \rho_{cp}V_{cp}c_{v_{cp}}[T_p]}$$

$$+ \frac{\dot{Q}_p[V, V_s, T_p] - P_g[V, V_s, V_{cp}, T_p]\dot{V}}{\rho_g(V, V_s, V_{cp})(V - V_s - V_{cp})c_{vg}[T_p] + \rho_{cp}V_{cp}c_{v_{cp}}[T_p]}, \tag{45}$$

is time derivative of temperature of both subsystems, namely temperature of the products. At the beginning of the modeling, the temperatures of condensed and gas phase products are assumed as equal to each other.

The last differential equation at the previous section,

$$\frac{d\dot{V}}{dt} = \frac{A_p}{m_p} F_p[V, V_s, V_{cp}, T_p], \tag{46}$$

is derived from Newton's second law. Therein, the volume change of combined system can be calculated at any time. It changes according to the force on piston defined in Equation (30).

These five order differential equations consist of five dependent variables. They are the combined system volume V, volume of solid pyrotechnics V_s, volume of condensed phase products V_{cp}, temperature of product system T_p and time derivative of combined system volume $\dot{V}$. To complete the preliminary model, it is necessary to define the following initial conditions:

$$V(t = 0) = V_0, V_s(t = 0) = V_{s0}, V_{cp}(t = 0) = V_{cp0}, T_p(t = 0) = T_0, \dot{V}(t = 0) = 0.$$

These differential equations can be solved with the initial conditions by using the fourth order Runge-Kutta integration method [21]. Runge-Kutta method, a kind of predictor and corrector model, is a numerical solution methodology for the first order differential equations. Here, the basic idea is to move function f(y, x) from step n to n+1 by multiplying some estimated slope, whose number can change one to four depending on the solving approach.

In the Fourth-order Runge-Kutta method, there are four preliminary estimates to get one slope as shown in Figure 14.
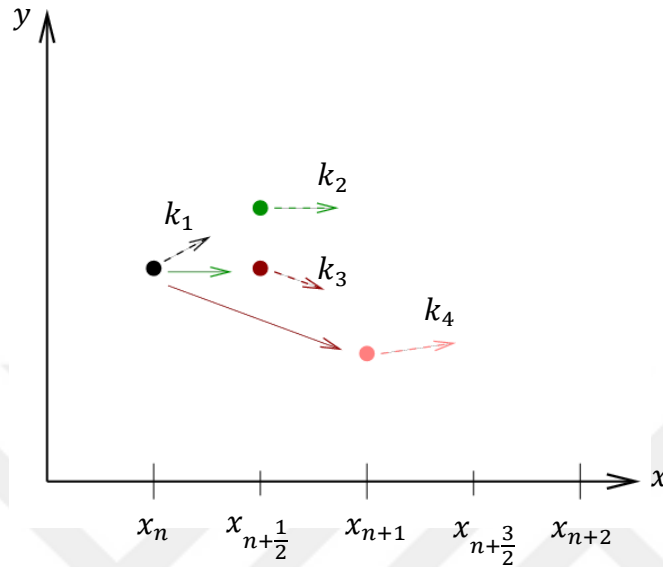
Figure 14: Graph representation of four preliminary estimate slopes

k_1 is the slope at the beginning of time step

$$k_1 = f(x_n, y_n). \tag{47}$$

If k_1 is used to step halfway through the time step,

$$k_2 = f(x_n + \frac{1}{2}h, y_n + \frac{1}{2}hk_1) \tag{48}$$

is the slope at the midpoint. If k_2 is used to step halfway through the time step,

$$k_3 = f(x_n + \frac{1}{2}h, y_n + \frac{1}{2}hk_2) \tag{49}$$

is another slope at the midpoint. Finally, k_4 is the slope at the endpoint

$$k_4 = f(x_n + h, y_n + hk_3). \tag{50}$$

34

As a result of this re-evaluating function $f(y_n, x_n)$ together with the estimated slopes, which is taken between two steps n and $n + 1$, the function values y_{n+1} can be calculated

$$y_{n+1} = y_n + \frac{1}{6} h(k_1 + 2k_2 + 2k_3 + k_4). \tag{51}$$

3.6 PYROTECHNIC COMBUSTION MODEL

The developed pyrotechnic combustion model is different from the Gonthier and Powers work [3]. These differences are the logic of the programming, method of numerical integration and thermochemistry data for the pyrotechnics. The code is developed by using the thermochemistry parameters for the pyrotechnics, the geometrical and constitutive variables at the explosive bolt. It can compute the performance parameters of the pressure type explosive bolts depend on time by using these inputs, and equations defined in the previous section. The combustion of pyrotechnics inside the body is modeled as multiphase systems. The advantage of this approach is that the unreacted solid pyrotechnics, gas and condensed phase products can be accounted separately. Also, mass, momentum and energy transfer between the phases can be calculated. Moreover, three different boundary conditions are defined to control the calculation inside the code. The first one is the stroke. The calculated stroke value at any time is compared with the maximum stroke value. If stroke value becomes higher than the maximum stroke, the analysis methodology changes to constant volume from changeable volume. After checking the stroke value, the mass of solid pyrotechnics is controlled. If it becomes zero, the volume of solid particles can be taken as a constant and the volume of solid pyrotechnics should be taken as zero. In other case, the governing equations can be calculated according to their expressions. In the last step, the calculated parameters can be written to the output folder and the analysis time can be checked whether is reach the defining maximum analysis time. Then, the code can return to beginning or close to the program according to the condition. The detailed flow chart for the pyrotechnic combustion model is shown in Figure 15.

3.6.1 Analysis Methodology
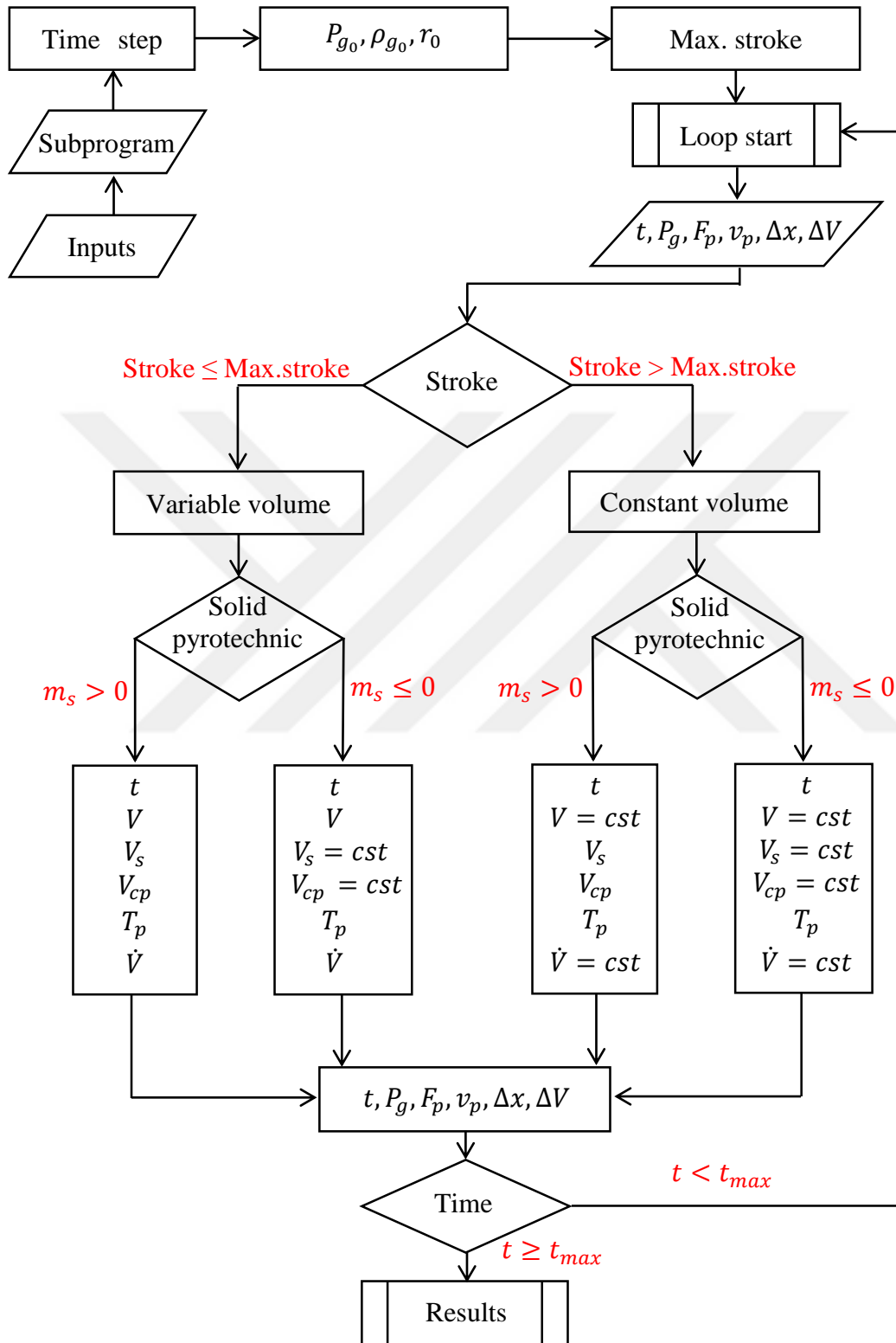
Figure 15: Flow chart of the ballistic simulation

3.6.2 Pyrotechnic Combustion

In this section, the combustion of pyrotechnics is examined in details. They are the chemical equation with the mole fractions and thermodynamic data for the products of this chemical equation. By using these parameters, the specific heats and internal energies of gas and condensed phase products, which are required to solve ordinary differential equations, can be calculated.

3.6.2.1 The Chemical Equation

The chemical equation used in the ballistic combustion model, can be predicted by the constant volume combustion calculation performed with ICT chemical equilibrium code [20]. Within this scope, ignition of 5 gr ZPP is simulated at 200 cc closed bomb. ZPP contains 52% zirconium (Zr) and 48% potassium perchlorate ($KClO_4$). As a result of this simulation, the reaction products can be obtained with the mole and weight fractions. They are presented in Table 2. By using the mole number of the reactants and products, the chemical reaction used in the ballistic simulation becomes like in Table 3.

Table 2: Mole fraction of reaction products

Name	Mole Number	Mole %	Wgt. %
O(g)	1.05605E+00	9.066	1.690
Cl(g)	6.7547E-01	5.799	2.395
K(g)	5.6758E-01	4.873	2.219
Zr(g)	7.50782E-05	0.001	0.001
O_2(g)	7.39858E-01	6.352	2.367
O_3(g)	1.38579E-05	0.000	0.000
ClO(g)	1.08874E-02	0.093	0.056
Cl_2(g)	1.40269E-03	0.012	0.010
KCl(g)	2.77532E+00	23.826	20.690
KO(g)	1.20610E-01	1.035	0.665
K_2(g)	4.84986E-04	0.004	0.004
ZrO(g)	2.10239E-01	1.805	2.254
ZrO_2(g)	2.93749E+00	25.218	36.195
ZrO_2(cp)	2.55270E+00	21.915	31.454

Table 3: Chemical reaction of ZPP used in pyrotechnic combustion simulation

$5.7005Zr(s) + 3.46448KClO_4(s) \rightarrow 2.5527ZrO_2(cp) + 1.05605(g) + 2.77532KCl(g)$
$+0.67547Cl(g) + 0.56758K(g) + 0.739858O_2(g)$
$+2.93749ZrO_2(g) + 0.12061KO(g)$
$+0.210239ZrO(g) + 0.0108874ClO(g)$
$+0.000484986K_2(g) + 0.00140269Cl_2(g)$
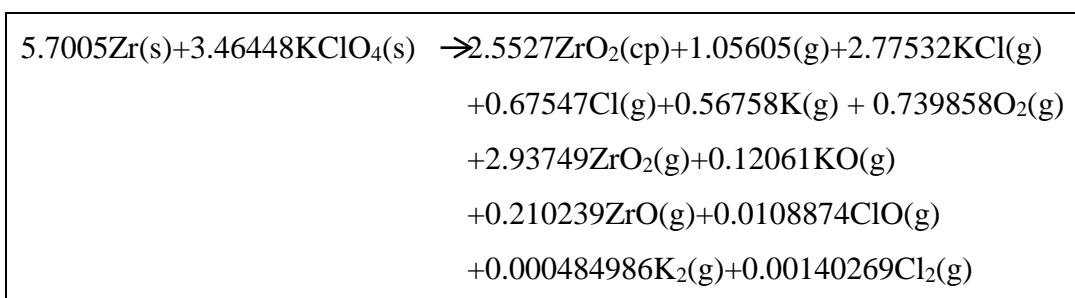
3.6.2.2 Thermochemistry Data

To solve the deriving first order differential equations, we need to calculate the specific heats and internal energies for both condensed and gas phased products listed in Table 2. For each product, the thermodynamic functions for specific heat and enthalpy, that can be used to calculate the internal energy, are given in the form of least-square coefficients like in Gordon and McBride work at 1976 [22].

According to this work and the chemical equilibrium program during the last 25 years, a fourth-order polynomial equation has been used to define the molar heat capacitance at constant pressure, which is shown with C_p^0, for the ideal gas as follows

$$\frac{C_p^0}{R} = a_1 + a_2 T + a_3 T^2 + a_4 T^3 + a_5 T^4. \tag{52}$$

At the upper and following fourth-order polynomial thermodynamic equations, a_1 to a_6 represents the least square constants and T is the temperature of the products. For each constant, there are low and high temperature intervals, especially for the gases. For example, ZrO_2, which is one of the combustion products of ZPP, has 200-1000 K and 1000-5000 K temperature intervals.

However, the specific heats of the products at constant volume must require solving the derived first order differential equations system. The relationship between C_p and C_v for ideal gas,

$$C_p = C_v + R, \tag{53}$$

can be found by using the definition of enthalpy with derivation as follows

$$h = e + Pv, \tag{54}$$

$$dh = de + d(Pv),\tag{55}$$

$$C_p^0 dT = C_v^0 dT + R dT.\tag{56}$$

The molar heat capacitance at constant volume,

$$\frac{C_v^0}{R} = a_1 + a_2 T + a_3 T^2 + a_4 T^3 + a_5 T^4 - 1,\tag{57}$$

can be expressed by using Equations (52-53).

Moreover, the same methodology can be used to define the specific heat at constant volume for condensed phase species. It is worth noting that the last term of the right hand side of Equation (53) is equal to zero for condensed particles since the change of the volume cannot create works on the system. Within this scope, the specific heats at constant pressure and constant volume can be taken as equal. As a result, the molar heat capacity at constant volume can be defined as follows:

$$\frac{C_v^0}{R} = a_1 + a_2 T + a_3 T^2 + a_4 T^3 + a_5 T^4.\tag{58}$$

Besides the specific heats, the internal energies for each product should be calculated. In Gordon and Mc. Bride work, the enthalpy function,

$$\frac{H^0}{RT} = a_1 + \frac{a_2}{2}T + \frac{a_3}{3}T^2 + \frac{a_4}{4}T^3 + \frac{a_5}{5}T^4 + \frac{a_6}{T},\tag{59}$$

can be expressed as fourth-order polynomial with least square constants.

The relationship between the internal energy (U^0) and enthalpy (H^0) for ideal gas can be defined as

$$U^0 = H^0 - RT. \tag{60}$$

Then, the internal energy becomes

$$\frac{U^0}{RT} = a_1 + \frac{a_2}{2}T + \frac{a_3}{3}T^2 + \frac{a_4}{4}T^3 + \frac{a_5}{5}T^4 + \frac{a_6}{T} + 1. \tag{61}$$

For the internal energy of the condensed phase products, the same methodology can be used like in the specific heat calculation. The internal energy and enthalpy are equal to each other under normal circumstances for condensed phased particles. Within this scope, the internal energy becomes

$$\frac{U^0}{RT} = a_1 + \frac{a_2}{2}T + \frac{a_3}{3}T^2 + \frac{a_4}{4}T^3 + \frac{a_5}{5}T^4 + \frac{a_6}{T}. \tag{62}$$

To solve these thermodynamic relations, least square coefficients and temperature of the particles are required. Temperature of the particles can be obtained from the ballistic simulation at each step while these thermodynamic constants can be obtained from the CET93 chemical equilibrium code [18] presented in Table 4 and BURCAT thermos data [19] presented in Table 5. In these tables, "I" represents the temperature interval between 2950 and 5000 K; "II" represents the temperature interval between 200 and 1000 K; "III" represents the temperature interval between 1000 and 6000 K; "IV" represents the temperature interval between 300 and 1000 K and "V" represents the temperature interval between 1000 and 5000 K.

Table 4: Least square coefficients at CET93 thermochemical database

Sub.	Temp. Range [K]	a_1	a_2	a_3	a_4	a_5	a_6
ZrO_2 (cp)	I	1.06E+01	0.00E+00	0.00E+00	0.00E+00	0.00E+00	-1.28E+05
O (g)	II	3.17E+00	-3.28E-03	6.64E-06	-6.13E-09	2.11E-12	2.91E+04
	III	2.54E+00	-2.73E-05	-4.19E-09	4.95E-12	-4.80E-16	2.92E+04
Cl (g)	II	2.26E+00	1.54E-03	-6.80E-07	-1.60E-09	1.15E-12	1.39E+04
	III	2.95E+00	-3.86E-04	1.36E-07	-2.17E-11	1.29E-15	1.37E+04
K (g)	II	2.50E+00	-7.25E-08	2.59E-10	-3.79E-13	1.93E-16	9.96E+03
	III	2.26E+00	5.62E-04	-4.49E-07	1.36E-10	-1.03E-14	1.00E+04
Zr (g)	II	1.24E+00	1.28E-02	-2.72E-05	2.33E-08	-7.09E-12	7.26E+04
	III	2.54E+00	6.23E-04	-1.07E-07	2.39E-11	-2.18E-15	7.28E+04
O_2 (g)	II	3.17E+00	-3.28E-03	6.64E-06	-6.13E-09	2.11E-12	2.91E+04
	III	2.54E+00	-2.73E-05	-4.19E-09	4.95E-12	-4.80E-16	2.92E+04
ClO (g)	IV	2.82E+00	4.45E-03	-4.41E-06	1.59E-09	-1.45E-14	1.12E+04
	V	4.09E+00	5.00E-04	-1.88E-07	3.51E-11	-2.42E-15	1.09E+04
Cl_2 (g)	II	2.74E+00	7.84E-03	-1.45E-05	1.26E-08	-4.13E-12	-1.06E+03
	III	4.75E+00	-4.89E-04	2.68E-07	-2.43E-11	-1.04E-15	-1.51E+03
KCl (g)	IV	3.99E+00	2.11E-03	-3.18E-06	2.25E-09	-5.91E-13	-2.71E+04
	V	4.46E+00	1.22E-04	-9.17E-09	9.26E-13	-1.04E-17	-2.72E+04
KO (g)	IV	3.74E+00	3.12E-03	-4.80E-06	3.47E-09	-9.36E-13	7.34E+03
	V	4.42E+00	1.99E-04	-3.71E-08	7.13E-12	-5.04E-16	7.21E+03
K_2 (g)	II	4.51E+00	-4.36E-04	3.27E-06	-4.18E-09	1.20E-12	1.35E+04
	III	6.95E+00	-3.60E-03	1.18E-06	-1.74E-10	9.70E-15	1.26E+04
ZrO (g)	II	4.12E+00	-1.32E-02	6.93E-05	-9.59E-08	4.10E-11	9.01E+03
	III	9.30E+00	-2.90E-03	1.16E-06	-1.80E-10	1.02E-14	7.68E+03
ZrO_2 (g)	IV	3.21E+00	1.16E-03	-1.56E-05	1.00E-08	-2.54E-12	-3.58E+04
	V	6.14E+00	9.77E-04	-4.33E-07	8.50E-11	-6.13E-15	-3.64E+04

Table 5: Least square coefficients at BURCAT thermochemical database

Sub.	Temp. Range [K]	a_1	a_2	a_3	a_4	a_5	a_6
ZrO_2 (cp)	I	1.20E+01	0.00E+00	0.00E+00	0.00E+00	0.00E+00	-1.30E+05
O (g)	II	3.17E+00	-3.28E-03	6.64E-06	-6.13E-09	2.11E-12	2.91E+04
	III	2.54E+00	-2.73E-05	-4.19E-09	4.95E-12	-4.80E-16	2.92E+04
Cl (g)	II	2.26E+00	1.54E-03	-6.80E-07	-1.60E-09	1.15E-12	1.39E+04
	III	2.95E+00	-3.86E-04	1.36E-07	-2.17E-11	1.29E-15	1.37E+04
K (g)	II	2.50E+00	-7.52E-08	2.70E-10	-3.95E-13	2.00E-16	9.96E+03
	III	2.11E+00	8.27E-04	-5.99E-07	1.70E-10	-1.29E-14	1.01E+04
Zr (g)	II	1.24E+00	1.28E-02	-2.72E-05	2.34E-08	-7.11E-12	7.13E+04
	III	2.50E+00	6.91E-04	-1.35E-07	2.71E-11	-2.16E-15	7.15E+04
O_2 (g)	II	3.78E+00	-3.00E-03	9.85E-06	-9.68E-09	3.24E-12	-1.06E+03
	III	3.66E+00	6.56E-04	-1.41E-07	2.06E-11	-1.30E-15	-1.22E+03
ClO (g)	II	3.11E+00	5.02E-03	-7.55E-06	5.51E-09	-1.56E-12	-1.33E+04
	III	4.29E+00	3.03E-04	-8.42E-08	1.44E-11	-8.52E-16	-1.36E+04
*Cl_2 (g)	II	2.74E+00	7.84E-03	-1.45E-05	1.26E-08	-4.13E-12	-1.06E+03
	III	4.75E+00	-4.89E-04	2.68E-07	-2.43E-11	-1.04E-15	-1.51E+03
*KCl (g)	IV	3.99E+00	2.11E-03	-3.18E-06	2.25E-09	-5.91E-13	-2.71E+04
	V	4.46E+00	1.22E-04	-9.17E-09	9.26E-13	-1.04E-17	-2.72E+04
KO (g)	II	2.98E+00	7.86E-03	-1.62E-05	1.52E-08	-5.31E-12	6.66E+03
	III	4.89E+00	-7.60E-04	5.60E-07	-1.15E-10	6.95E-15	6.26E+03
*K_2 (g)	II	4.51E+00	-4.36E-04	3.27E-06	-4.18E-09	1.20E-12	1.35E+04
	III	6.95E+00	-3.60E-03	1.18E-06	-1.74E-10	9.70E-15	1.26E+04
ZrO (g)	II	4.12E+00	-1.32E-02	6.93E-05	-9.58E-08	4.10E-11	9.01E+03
	III	7.29E+00	-2.89E-03	1.16E-06	-1.2E+01	1.05E-14	7.69E+03
ZrO_2 (g)	II	3.94E+00	6.13E-03	-1.28E-06	-5.40E-09	3.37E-12	-3.96E+04
	III	5.98E+00	1.40E-03	-8.01E-07	2.02E-10	-1.55E-14	-4.01E+04

* These data were taken from the CET93 since there is no data for these species at BURCAT.

3.6.3 Input Parameters

To start the numerical algorithm, it is necessary to describe the input parameters for ballistic performance. These baseline parameters used in the simulation of the pyrotechnic explosive bolts are presented in Table 6.

Table 6: Input parameters used in pyrotechnic combustion modeling for performance prediction of pyrotechnic explosive bolt

Parameter	Definition	Unit	Value
η_{cp}	Mass fraction of products in the condensed phase	-	0.31
A_p	Cross section area of the piston	cm^2	0.82
m_p	Mass of the piston	g	7.16
ρ_s	Solid pyrotechnics density	g/cm^3	3.59
ρ_{cp}	Condensed phase product density	g/cm^3	8.44×10^{-7}
h	Convective heat transfer coefficient	$g/s^3/K$	1.25×10^6
σ	Stefan Boltzmann constant	$g/s^3/K$	5.67×10^{-5}
ε	Net emissivity of the product mixture	-	0.6
α	Absorptivity of the bolt body	-	0.6
F_{crit}	Critical force for failure of the shear pin	dyne	3.56×10^7
b	Pressure constant	$(dyne/cm^2)^{-0.74}$ cm/s	0.0012
n	Pressure constant	-	0.69
e_s	Internal energy for the solid pyrotechnics	$g.cm^2/s^2$	1.5×10^{10}

3.6.4 Initial Conditions

At the numerical algorithm, the initial conditions should be defined to solve the first order differentiations. All these conditions for the pyrotechnic explosive bolt are presented in Table 7.

Table 7: Initial conditions used in pyrotechnic combustion modeling for performance prediction of pyrotechnic explosive bolt

Parameter	Initial Condition	Unit	Value
V_0	Initial volume of the expansion chamber	cm^3	0.7
V_{s0}	Initial volume of the solid pyrotechnics	cm^3	0.028
V_{cp0}	Initial volume of the condensed phase products	cm^3	5.9×10^{-7}
T_0	Initial temperature	K	288
$\dot{V}_0$	Initial time derivative of volume change	cm^3/s	0.0

3.6.5 Analysis Results

In this part, the ballistic solution, which is developed to solve the performance of the pyrotechnic systems at closed volume, is presented for the designed pyrotechnic explosive bolt.

In Figure 16, the pressure histories are given for the pyrotechnic explosive bolt. The x-axis of the graph represents the pressure data coming from the simulation as unit of MPa and y-axis simulates the time in second units. Here, after a rapid pressure rising, the maximum pressure value becomes near 52 MPa at 0.14 ms. Then, it starts to decrease around 22 MPa due to the heat transfer between the products and wall of the bolt.
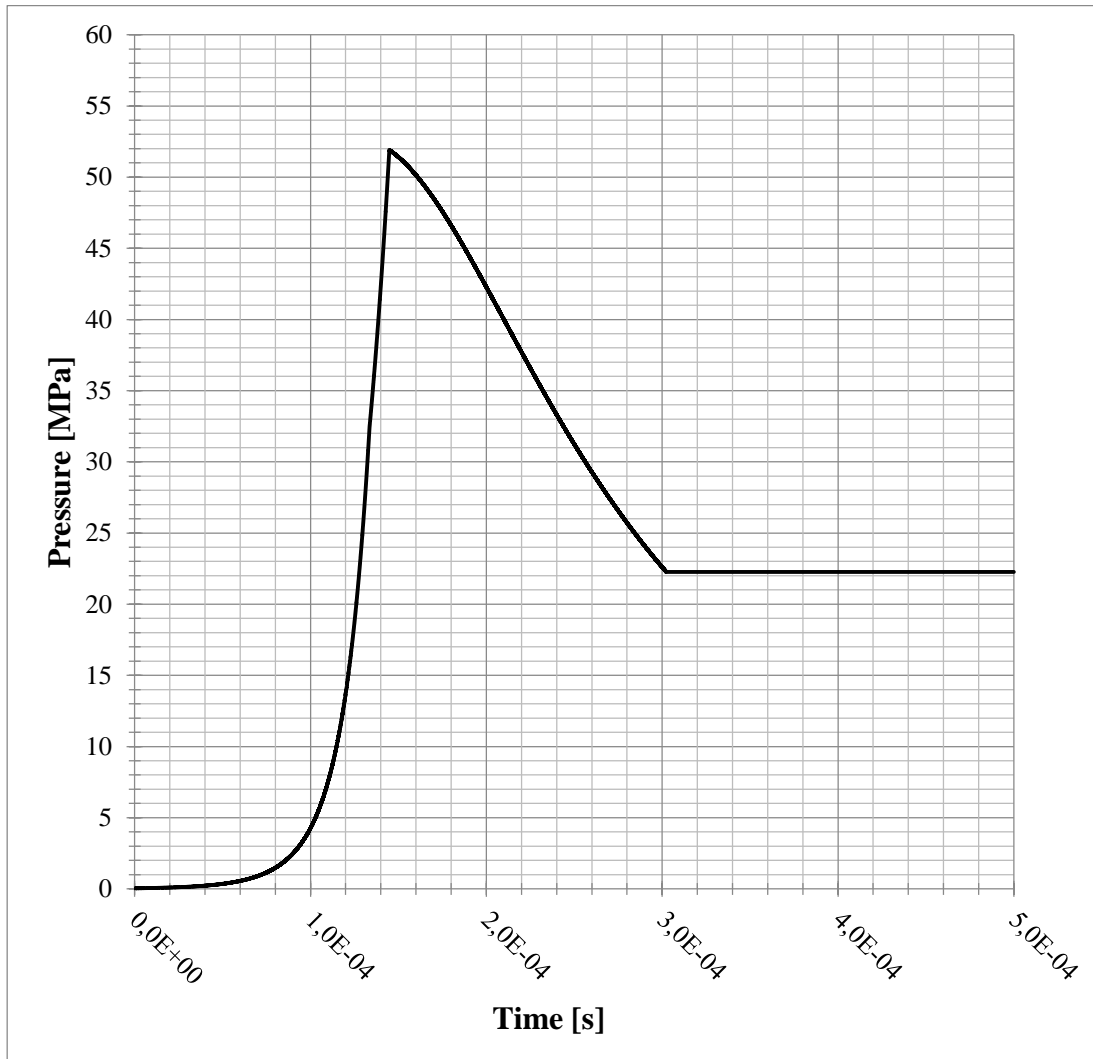
Figure 16: Pressure histories vs time graph for the ballistic simulation of pyrotechnic
explosive bolts

Figure 17 illustrates the temperature change of the products during the ignition of ZPP. The x-axis of the graph represents the temperature data coming from the simulation as unit of K and y-axis simulates the time in second units. As combustion proceeds, the temperature rises up to 3500 K at 0.12 ms. Also, the condensed phase of ZrO_2 starts to occur after the temperature reaches to 2950 K. Temperature of the products starts to subsequently decay with the consumption of solid pyrotechnics as shown in Figure 18.
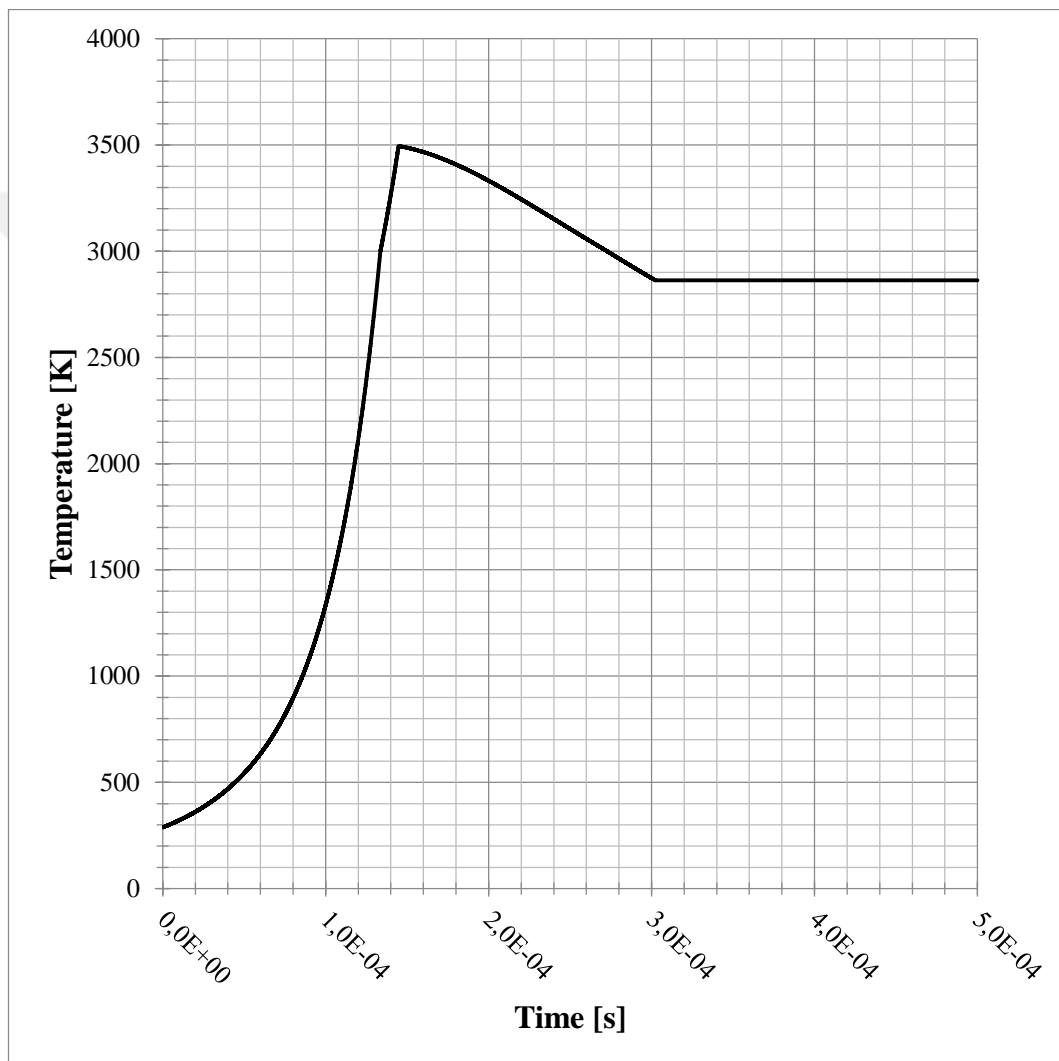
Figure 17: Temperature histories vs time graph for the ballistic simulation of pyrotechnic explosive bolts
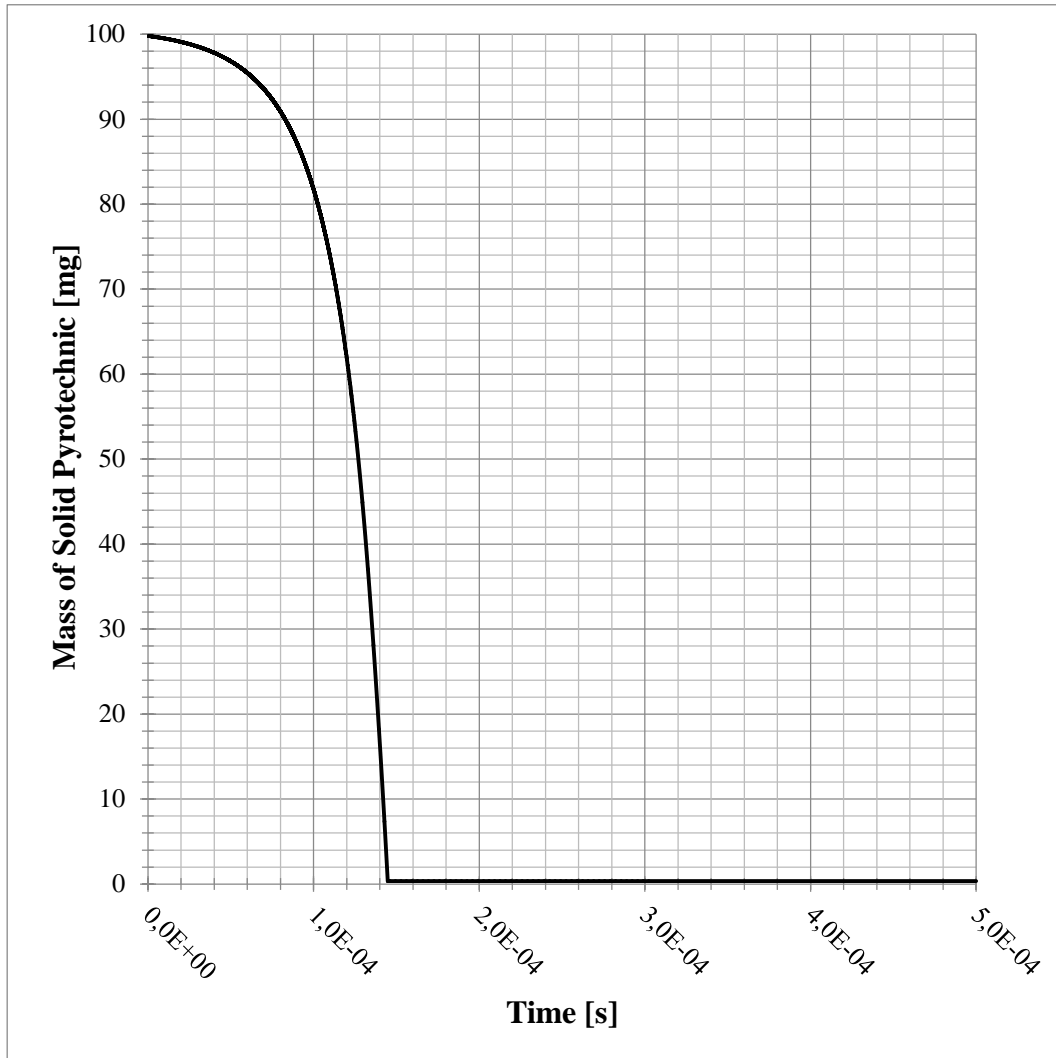
Figure 18: Change of ZPP during the combustion at the ballistic simulation of pyrotechnic explosive bolts

To understand the relationship between the pressure at the expansion chamber and velocity of the piston, they can be illustrated in the same figure. The velocity of the piston, which is shown with the dashed line in Figure 19, is equal to zero up to 0.1 ms.

During that period, the pressure inside the expansion chamber continues increasing. When the force on the piston reaches the critical value, the shear pin fails. Although the pressure reaches to the peak value, the velocity of the piston has still increased up to impact to the body wall. In the ballistic simulation, after the stroke completed, like crashing the bolt body, the velocity of the piston goes down 0 m/s directly at 0.3 ms. The maximum velocity of the piston is 79 m/s at the impact time.
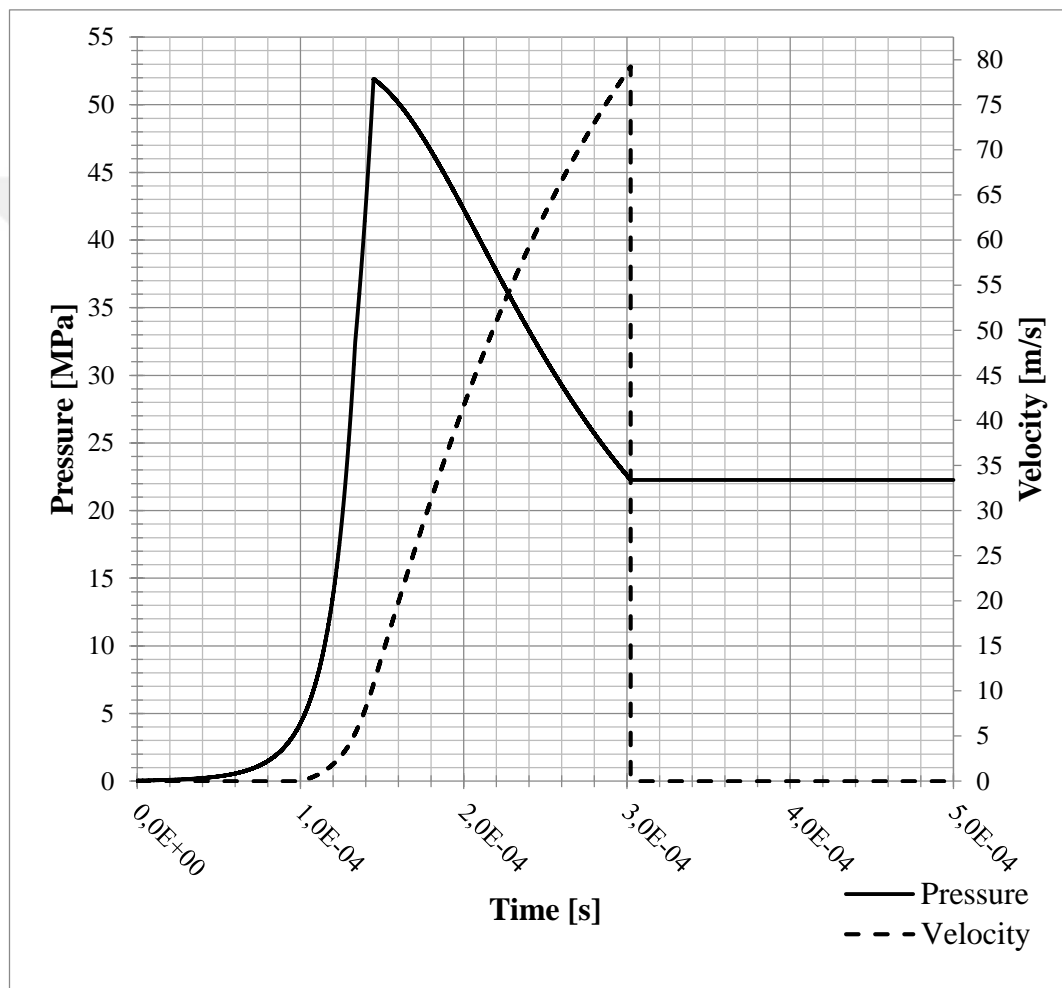
Figure 19: Change of the pressure and velocity of the piston

The predicted position of the piston can be also analyzed with the ballistic simulation of the pyrotechnic explosive bolt. The initial position can be calculated in the simulation by using the initial volume of system. As you can see from Figure 20, the

49

initial position of the piston is 8.5 mm. After failure of the shear pin, it increases to 16.5 mm at the end of stroke.
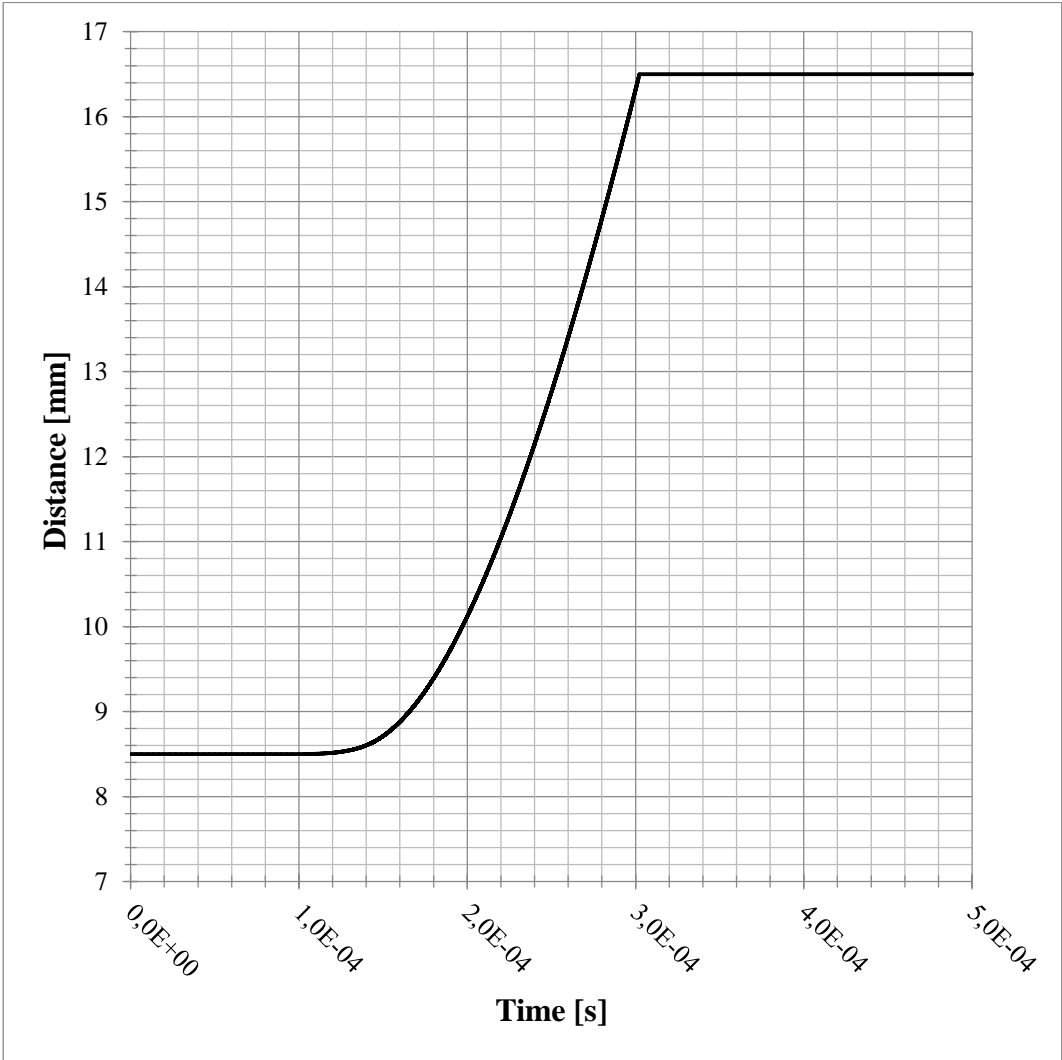
Figure 20: Position change of the piston

Like in the prediction of the position, the volume change of the expansion chamber can also be analyzed with the ballistic simulation of the pyrotechnic explosive bolt. It can be calculated by using the position of the piston at the simulation. As you can see

from Figure 21, the initial volume is around 0.7 cm^3. After failure of the shear pin, it becomes 1.36 cm^3 at the end of stroke.
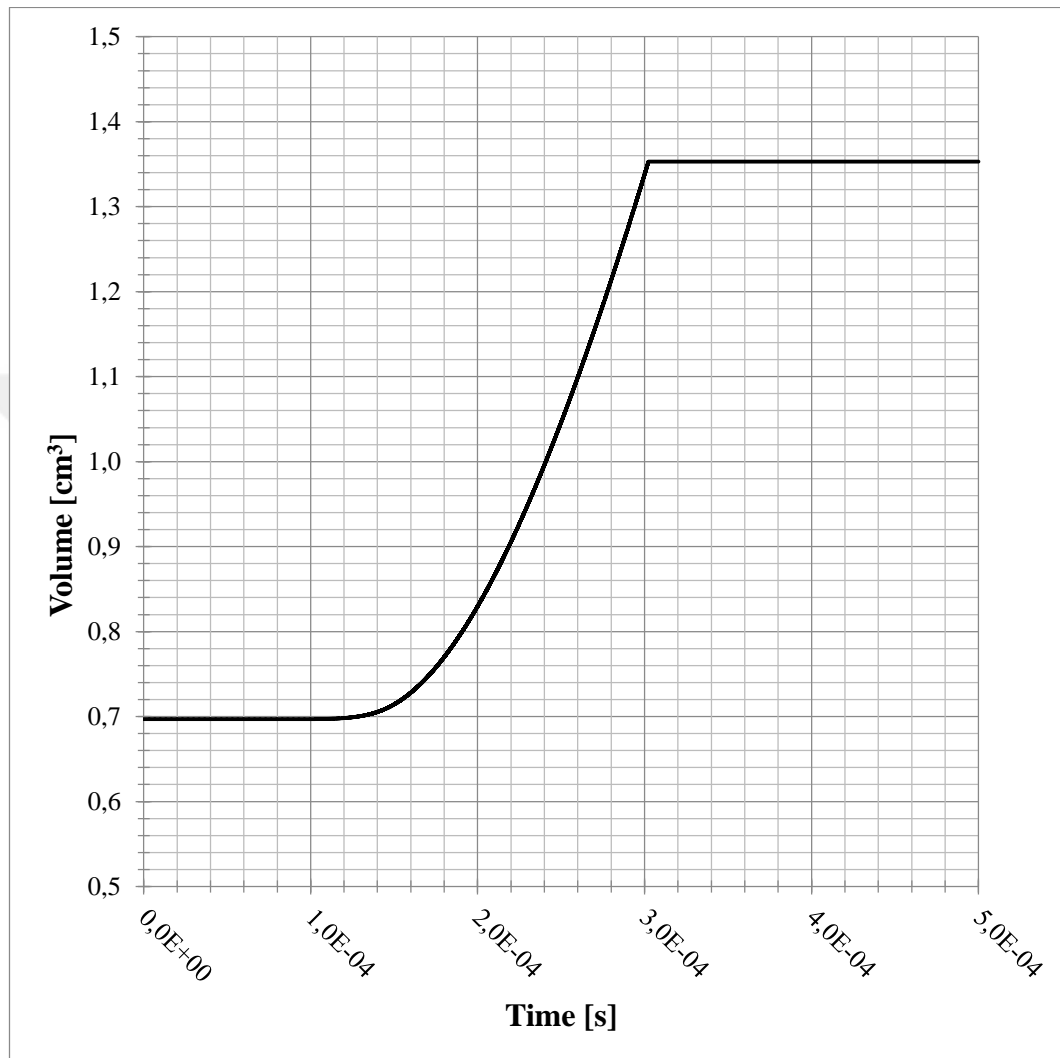
Figure 21: Volume change of the expansion chamber

3.6.6 Model Validation with Closed Bomb Experiments

The developed ballistic simulation model for the pyrotechnic explosive bolt should be validated with the experimental results. Within this framework, the closed bomb testing is the most commonly used method to measure the performance of pyrotechnic systems. According to NASA standards, a typical NASA standard initiator, which

contains 114 mg ZPP, should produce a peak pressure of 4.48±0.86 MPa into a 10 cm^3 closed volume.

To validate the model, the closed bomb experiment is performed at the 16 cc closed bomb and the closed bomb version of the pyrotechnic explosive bolt. The ignition can be performed by applying 3.5 Ampere along 50 ms with collect data by using the pressure sensor.

3.6.6.1 16 cc Closed Bomb Experiment

16 cc closed bomb experiment is very similar to the NASA standard initiator performance test apart from the volume of the closed bomb. In this test, the initiator is imperviously placed to the closed bomb and it is activated by using the current to the bridgewire into the initiator. During the test, the pressure inside the bomb is collected by using pressure sensor.

In the ballistic simulation, the input parameters are presented in Table 8 for the 16 cc closed bomb. The main differences from the ballistic simulation of the pyrotechnic explosive bolt are the convective heat transfer and pressure constants. Since the combustion chamber volume is very high with respect to the explosive bolts, the ignition behavior of ZPP shows an alteration. When the volume is high, the temperature of the products cannot reach higher values as 3500 K. Moreover, this lower temperature behavior can cause to be a non-condensed phase products and as a results of it, the heat transfer rate can become less than the explosive bolt. With this knowledge, the convective heat transfer coefficients can be taken as 1.25x10^5 g/s^3/K from Gonthier and Powers works [23] at 1992. The pressure constants are the specific variables for the using ZPP.

Table 8: Input parameters used in pyrotechnic combustion modeling for performance prediction of 16 cc closed bomb

Parameter	Definition	Unit	Value

η_{cp}	Mass fraction of products in the condensed phase	-	0.31
A_p	Cross section area of the piston	cm^2	0.2
m_p	Mass of the piston	g	0
ρ_s	Solid pyrotechnics density	g/cm^3	3.59
ρ_{cp}	Condensed phase product density	g/cm^3	1.51
h	Convective heat transfer coefficient	$g/s^3/K$	1.25×10^5
σ	Stefan Boltzmann constant	$g/s^3/K$	5.67×10^{-5}
ε	Net emissivity of the product mixture	-	0.6
α	Absorptivity of the bolt body	-	0.6
F_{crit}	Critical force for failure of the shear pin	dyne	0
b	Pressure constant	$(dyne/cm^2)^{-0.74}$ cm/s	0.004
n	Pressure constant	-	0.8
e_s	Internal energy for the solid pyrotechnics	$g.cm^2/s^2$	1.5×10^{10}

In the numerical algorithm like in the previous simulation, initial conditions should be defined to solve the first order differential equations. All these conditions for 16 cc closed bomb systems are presented in Table 9.

Table 9: Initial conditions for 16 cc closed bomb systems used in pyrotechnic combustion modeling

Parameter	Initial Condition	Unit	Value
V_0	Initial volume of the expansion chamber	cm^3	16
V_{s0}	Initial volume of the solid pyrotechnics	cm^3	0.028
V_{cp0}	Initial volume of the condensed phase products	cm^3	5.1×10^{-7}
T_0	Initial temperature	K	288
$\dot{V}_0$	Initial time derivative of volume change	cm^3/s	0.0

The predicted pressure values at the ballistic simulation and experimental pressure data are compared in Figure 22. In that figure, the dashed line shows the experimental results while the solid line represents the analysis results. Both results show the same increasing behavior and their highest pressure difference (Peak pressures are 1.9 and 2.05 MPa.) becomes very small, only 0.15 MPa. The first step of the validation (constant volume control) can be accomplished by using these results.
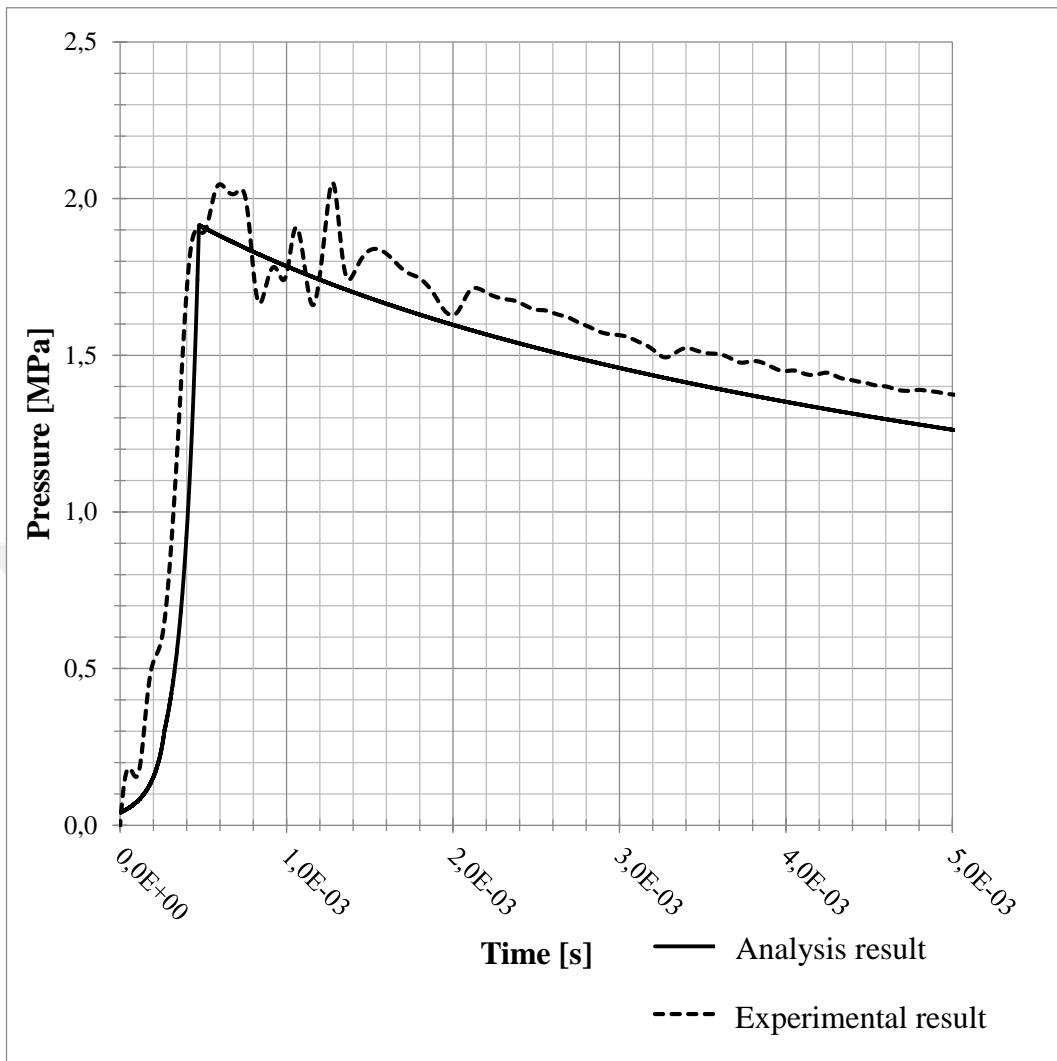
Figure 22: The comparison of the experimental and analysis results for the 16 cc closed bomb

3.6.6.2 Closed Bomb of Pyrotechnic Explosive Bolt Experiment

The closed bomb presented in Figure 23 is a version of the designed pyrotechnic explosive bolt and it simulates the expansion chamber. A hole reams out on the body to collect pressure data from the combustion chamber. Like in the designed one, there is a shear pin to fix the piston and after the force on the piston reaches the critical value, it starts moving. In the test, the initiator is imperviously placed to the closed bomb like in Figure 23 and it can be activated by using the current to the bridgewire into the initiator. During the test, the pressure is collected by using pressure sensor.
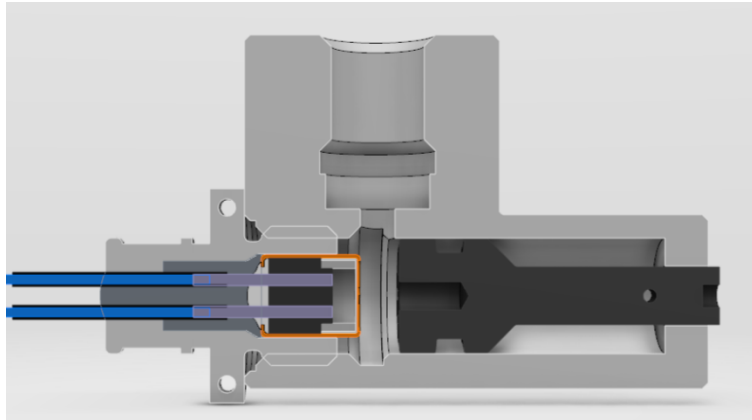
Figure 23: Closed bomb model of the pyrotechnic explosive bolt

The predicted pressure values in the ballistic simulation and experimental pressure data are compared in Figure 24. In that figure, the dashed line shows the experimental results while the solid line represents the analysis results. In this comparison, two important differences can be observed. The first one is the peak pressures. In the analysis result, the peak pressure is around the 52 MPa, but this value is collected as nearly 47 MPa for the experimental result. The gap between these peak pressures is corresponding to 10% error based on the experimental results. According to NASA standards [16], [24] and [25], the performance of the pyrotechnic initiator or NSI at the closed bomb has 19% error margin since these materials cannot be mixed homogenous and also, their particles size can be different. The last difference is related to the rising pressure at the beginning of the ignition. The predicted pressure has slowly increased up to 5 MPa with respect to the experimental result. The main reason is that the closure cap on the front of the initiator can resist the pressure at the beginning of the ignition. Therefore, the rising of the pressure has increased quickly after tearing the closure cap. However, it is not modeled in the ballistic simulation. Within this scope, the second step of the validation can also be accomplished for the variable volume control.

56
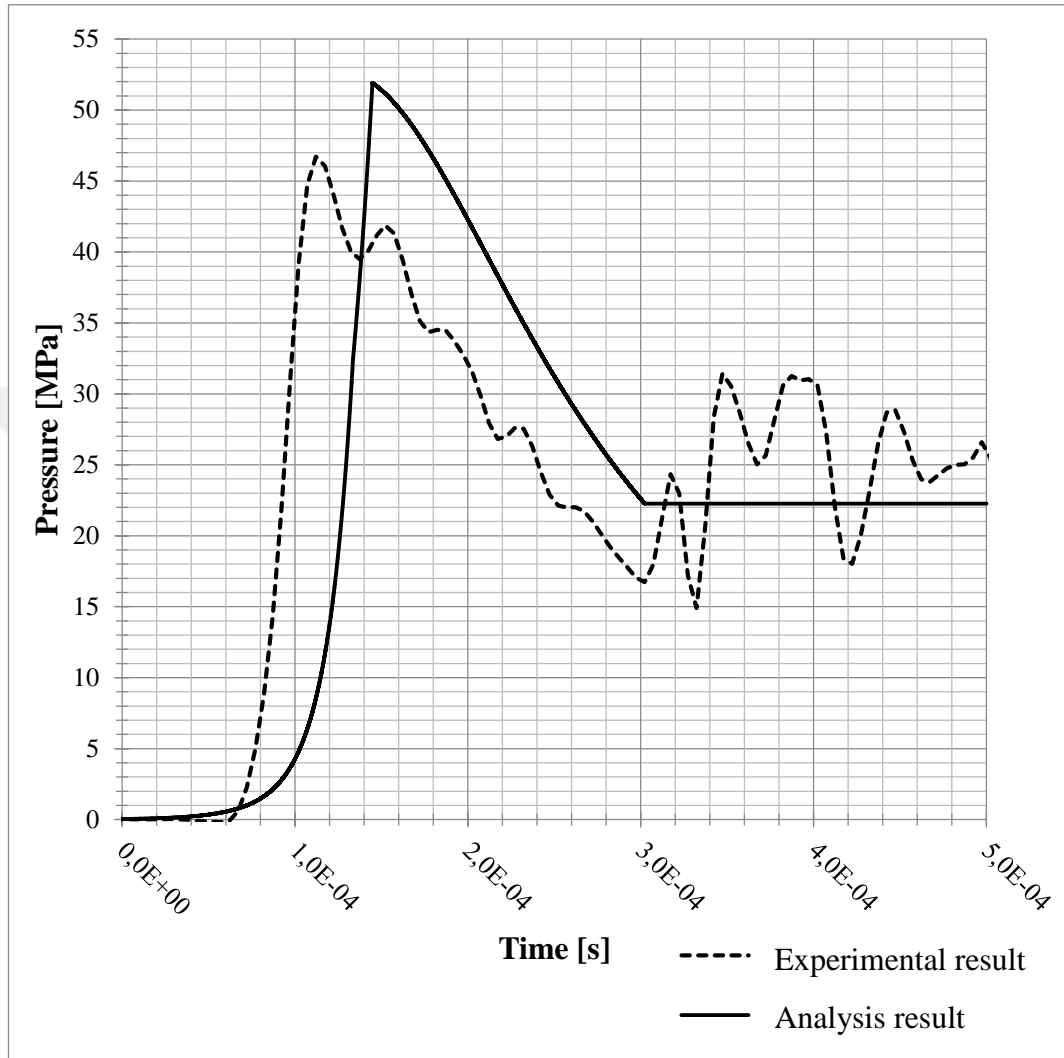
Figure 24: The comparison of the experimental and analysis results for the
pyrotechnic explosive bolt

CHAPTER 4

FINITE ELEMENT ANALYSIS

In this study, the main purpose is to observe the different separation behaviors with different piston geometries. After developing the ballistic model in the previous section, the separation can be analyzed using LS-DYNA. In the following section, a brief review of the analysis procedure is explained and then, model simplifications are defined to reduce computational costs. Before analyzing, theoretical background used in L-DYNA are defined such as solution methodologies, contacts, material models for the bolt body and piston, failure model for the bolt body. Also, meshing of the structure with their properties and analysis properties are explained.

4.1   ANALYSIS PROCEDURE

In this study, ANSYS Workbench Explicit Dynamics can be utilized to simplify the geometrical model and performed meshing of the all structure as shown in Figure 25. At this program, Design Modeler can be used to give a last geometrical form of the bolt body and piston of the pyrotechnic explosive bolt. Also, meshing of the structure can be performed at the Mechanic part of ANSYS Workbench. Then, the developed model can be imported to LS-DYNA from ANSYS Workbench. Here, the material and failure models can be defined. Finally, the analyses can be performed to understand the separation behavior of three distinct models.
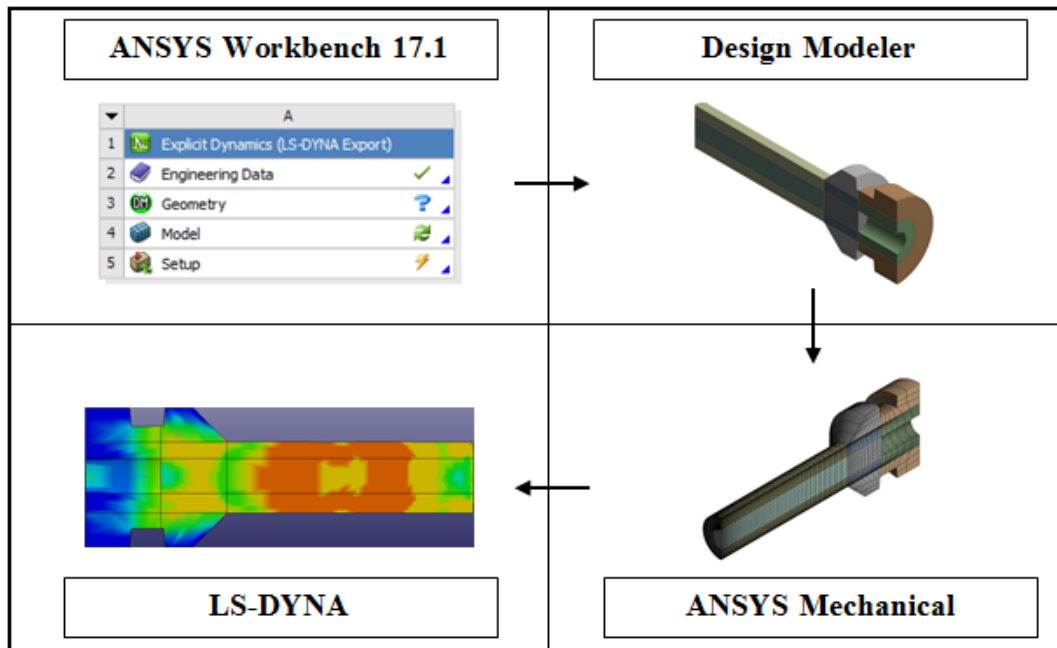
Figure 25: Analysis procedure for pyrotechnic explosive bolts

4.2 MODEL SIMPLIFICATIONS

In this section, some simplifications on the geometry models and analysis steps are given to reduce the analysis cost. These simplifications must be carefully performed without influencing the analysis results, but it should improve the computational performance of the analysis at the same time.

4.2.1 Part Simplifications

Although the piston has small dimensions, there are non-critical features within a CAD model. Firstly, the hole on the body, which is place of the shear pin, is one of these features. The material of piston, 17-4PH stainless steel, has more resistance than the bolt body material, AISI 4340 steel. Therefore, the deformation cannot be expected at the around of the hole. Within this scope, this hole on the piston can be deleted as shown in Figure 26. Also, the end of the thread on the back of the piston, which is used to enhance the mountability, should be simplified to avoid a corner sharp.
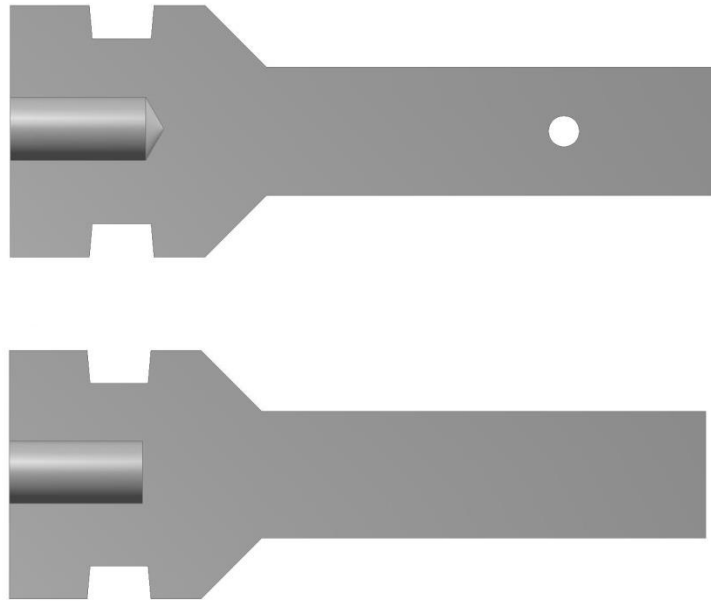
Figure 26: Piston simplification for the analysis

In the bolt body of pyrotechnic explosive bolt, a small edge inside the body should be simplified to eliminate the small size meshes on the body as shown in Figure 27. This critical feature can cause decreasing the time step of the analysis.
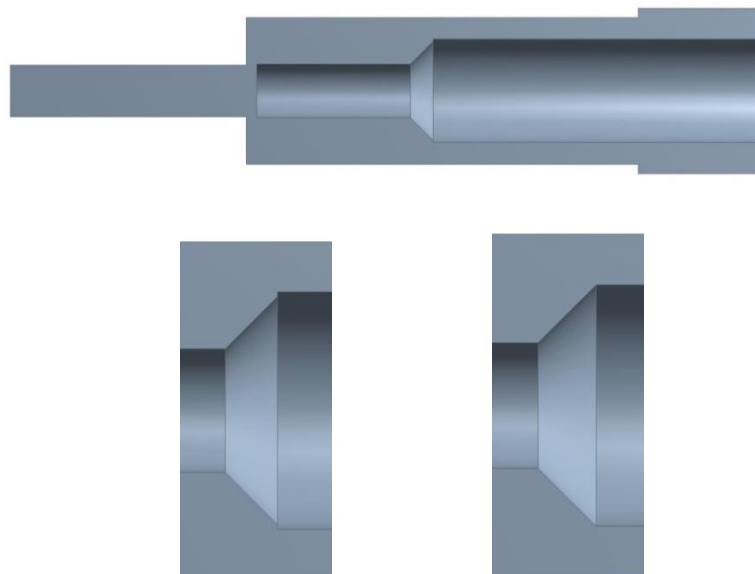
Figure 27: Bolt body simplification for the analysis

4.2.2 Assembly Simplifications

In solid mechanics, a symmetric boundary condition implies that the displacements normal to the symmetry plane and rotations about the axes in this plane are zero at the plane of symmetry. This symmetric structure means that the size of finite element model can be reduced and as a result of it, the cost or time of the analysis can be reduced. Moreover, a smaller simulation model like in this study can be analyzed with smaller element size to obtain more effective results.

The created pyrotechnic explosive bolt models can be symmetry with respect to all plane defined in xyz coordinate system. For example, xz-plane is symmetry for the pyrotechnic explosive bolt shown in Figure 28. Therefore, it can be used in the analysis models.

Another simplification on the assembly is the position of the piston. To reduce the cost, the analyses can be started at the impact time of the piston and bolt body as shown in Figure 29. The velocity can be predicted at that time by using the pyrotechnic ballistic simulation and it should be defined as initial velocity.
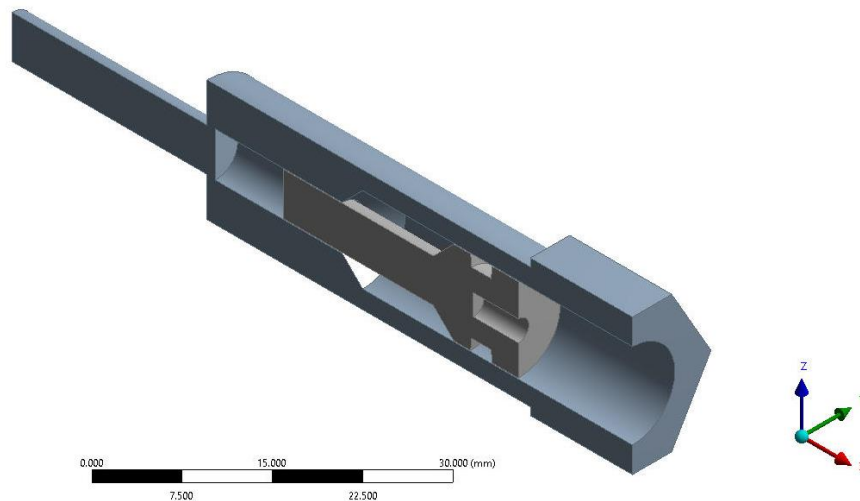
Figure 28: Symmetry model of the pyrotechnic explosive bolt
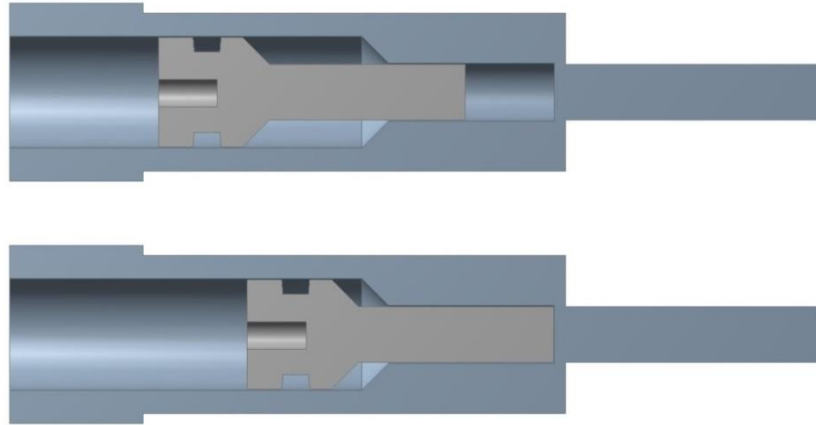
Figure 29: Position of the piston

4.3   THEORETICAL BACKGROUND

4.3.1   Solution Methodologies for Finite Element Analysis

The finite element method offers several algorithms for linear and nonlinear problems. These problems can be static, quasi-static or dynamic cases and they can be solved by using the implicit and explicit numerical methods.

For implicit method, the current quantities in one time step are based on the quantities calculated in the previous step. This integration methodology is known as Euler Time Integration Scheme. In this scheme even if large time steps are taken, the solution remains stable. This unconditionally stable implicit method can encounter some difficulties when a complicated three dimensional model is considered. The reasons are as follows [26]:

- o   The computational cost in tangent stiffness matrix is dramatically increased and this can cause the divergence problem as the reduction of the time increments.
- o   Local instabilities cause force equilibrium to be difficult to achieve.

The algorithm of the implicit procedure is defined by Hilber et al. [27]:

$$Ma^{n+1} + (1+\alpha)Ku^{n+1} - \alpha Ku^n = F^{n+1}.$$

(63)

The implicit procedure is based on the full Newton iterative solution method. In this algorithm, the inverse of stiffness matrix is used to solve directly the distance. The distance can be found at time $n + 1$ as:

$$\Delta u^{n+1} = \Delta u^n + K_n^{-1} \cdot (F^n - I^n), \tag{64}$$

where K^n is the current tangent stiffness matrix, F the applied load vector, I the internal force vector and Δu is the increment of displacement.

The displacement vector can be defined

$$u^{n+1} = u^n + \Delta t \dot{u}^n + \Delta t^2 \left[\left(\frac{1}{2} - \beta\right)\ddot{u}^n + \beta \ddot{u}^{n+1}\right], \tag{65}$$

and

$$\dot{u}^{n+1} = \dot{u}^n + \Delta t[(1 - \gamma)\ddot{u}^n + \gamma \ddot{u}^{n+1}] \tag{66}$$

with

$$\beta = \frac{1}{4}(1 - \alpha^2), \gamma = \frac{1}{2} - \alpha, \frac{1}{3} \le \alpha \le 0. \tag{67}$$

In a dynamic scenario, such as high velocity impact problems and crash tests, a time-step size that limits the advance of the pressure step to less than one computational cell per time step is critical if considering the accuracy. To overcome this problem, the explicit method is developed. It performs the analysis by using a large number of inexpensive, small time (load) increments.

In the explicit procedure, an explicit integration rule is implemented along the use of diagonal element mass matrices. The semi-discrete equations of motion at time n can be written as [28]:

$$M\ddot{u}^n = P^n - F^n + H^n, \tag{68}$$

where M is the diagonal mass matrix, P^n accounts for external and body force loads, F^n is the stress divergence vector, and H^n is the hourglass resistance.

To advance to time t^{n+1}, firstly, the nodal acceleration at time t^n can be obtained

$$\ddot{u}^n = M^{-1}(P^n - F^n + H^n).$$ (69)

Then, the central difference integration rule can be applied to update the velocity,

$$\dot{u}^{n+1/2} = u^{n-1/2} + \ddot{u}^n \Delta t^n,$$ (70)

And the displacement,

$$u^{n+1} = u^n + \dot{u}^{n+1/2}\Delta t^{n+1/2},$$ (71)

where

$$\Delta t^{n+1/2} = \frac{(\Delta t^n + \Delta t^{n+1})}{2}.$$ (72)

As a result, the geometry can be updated by adding the displacement increments to the initial geometry.

The drawback of the explicit method is that it is conditionally stable [26]. If the time increment of the problem too big, the solution becomes unstable and diverges rapidly. Also, the numerical stress wave must always propagate less than one element width per time increment. Therefore, it is necessary to define the critical time step for the given problem. For the explicit method, critical time step

$$\Delta t = \frac{L}{c},$$ (73)

where

$$c = \sqrt{\frac{E}{\rho}},$$ (74)

can be found by using the Courant-Friedrich-Lewy (CFL) condition. Therein, L and c are element size and wave speed, respectively. In the wave speed equation, E represents the Young's Modulus and ρ is the material density.

In this high velocity impact problem, the explicit software of LS-DYNA can be used to get high efficiency results with smaller time step. In this way, the cost of analysis can be reduced and the local instabilities can be prevented to satisfy the force equilibrium. The explicit solver used in LS-DYNA is summarized in Figure 30.
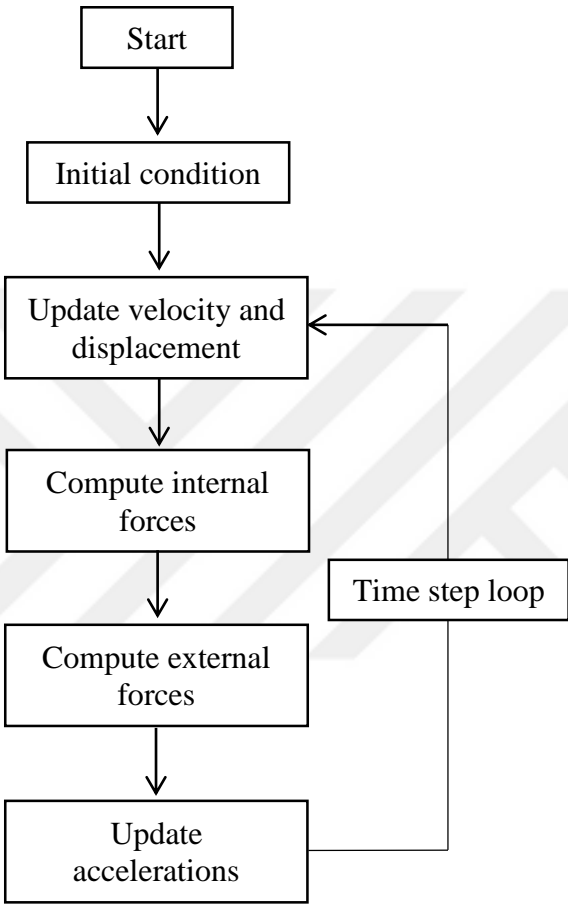
Figure 30: LS-DYNA Explicit Solver

4.3.2   Contact Theory

4.3.2.1   Contact Algorithms

Impact between the bolt body and piston is very critical in simulation because of the correct load transfer. The contact forces can influence the acceleration of the body. In LS-DYNA, there are three different methods for handling the contacts between bodies. These are the kinematic constraint method, the distributed parameter method and penalty method [28], [29].

4.3.2.1.1 Kinematic Constraint Method

The kinematic constraint method imposes constraints on the global equations with a transformation of the slave nodes displacements components along the contact interface. As a result of this transformation, the normal degrees of freedom of nodes are eliminated. The main problem for this method is that the master nodes can penetrate through the slave surface without resistance when the master surface zoning is finer than the slave one [28], [29].

4.3.2.1.2 Distributed Parameter Method

The distributed parameter method is based on constraints like in the kinematic constraint method. One-half the slave element mass of each element in contact is distributed to the covered master surface area. It uses a method of imposing constraints on the accelerations and velocities of the slave nodes to insure their movement along the master surface. This method has also same problem with the kinematic constraint method [28], [29].

4.3.2.1.3 Penalty Method

The penalty method consists of placing normal interface springs between all penetrating nodes and the contact surface. If a slave node is found to penetrate, an interface force is applied between the contact point and the penetrating node like in Figure 31. This force may be thought as the addition of the interface spring.
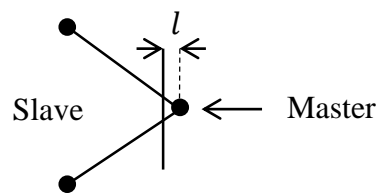
Figure 31: Penalty formation

The penalty or interface force,

$$f_S = -l k_i n_i,$$

(75)

is proportional to the stiffness factor k_i and penetration depth l with the normal vector of the master segment n_i.

The biggest disadvantage of the penalty method is related to the stiffness factor. If it is too low, the penetration will be too high. On the other hand, the high stiffness factor can cause the high frequency vibrations and the explicit time integration procedure may become unstable. Therefore, in LS-DYNA, a number of options are available for setting the penalty stiffness value. They are:

- Minimum of the master segment and slave node stiffness (default).
- Using the master segment stiffness.
- Using the slave node value.
- Using the slave node value, area or mass weighted.
- Using the slave node value, inversely proportional to the shell thickness.

The stiffness factor of these interface springs can be calculated in three different ways. In the standard method (SOFT=0), the contact stiffness,

$$k_{SOFT=0} = slsfac \cdot sf \cdot \frac{K \cdot A^2}{V},$$

(76)

is calculated based on element length and material property. Therein, K represents the bulk modulus, A represents the segment area, V represents the volume of the element, "$slsfac$" is the global scale factor and "sf" is the local scale factor [28], [29].

The second one is called soft constraint penalty contact (SOFT=1). It is based on the stability of a spring mass system considering the nodal mass m and global initial time step size Δt_c as given

$$k_{SOFT=1} = 0.5 \cdot sofscl \cdot \frac{m_n}{\Delta t_c^2}.$$

(77)

Therein, "$sofscl$" is the scale factor. It is important that the stiffness factor is the maximum of $k_{SOFT=0}$ and $k_{SOFT=1}$ for the soft constraint formulation [28], [29].

The last approach is the segment based contact

$$k_{SOFT=2} = 0.5 \cdot slsfac \cdot sfs \cdot \frac{m_1 \cdot m_2}{(m_1 + m_2) \cdot \Delta t_c^2}. \tag{78}$$

It computes the stiffness in a manner similar to SOFT=1. Moreover, the penetration of segments to segments is checked instead of nodes to segments [28], [29]. This alternative stiffness is defined by

For this study, contact-impact algorithm along the bolt body and piston, that is the flexible body contact, is taken as the penalty method and the stiffness factor are calculated by considering the segment based contact.

4.3.2.2 Contact Types

It is important that the components in contact need to be predefined in a group or groups and each of them has a specific contact algorithm with aforementioned different contact stiffness. In this section, a variety of contact types in LS-DYNA are introduced.

4.3.2.2.1 Single Surface Contact

The single surface contact algorithm checks penetrations between any two surfaces of all parts in the group and self-contacts at each time step, as schematically shown in Figure 32. It is very effective for self-contact and large deformation problems where areas of contact are not known beforehand [28], [29].

Figure 32: Single surface contact

4.3.2.2.2 Nodes to Surface Contact

Nodes to surface contact algorithm establishes contact when a contacting node penetrates a target surface. It is the fastest algorithm since it is symmetric. At each time step, each node on the surfaces of slave parts is checked for penetration through

the master surfaces, as schematically shown Figure 33. If a penetration is detected, normal and tangential forces are applied between the slave node and contacting surfaces [28], [29].
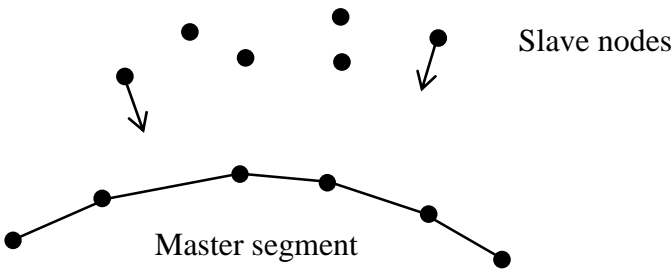
Figure 33: Nodes to surface contact

4.3.2.2.3 Surface to Surface Contact

Surface to surface contact algorithm establishes contact when the surface of one body penetrates to another surface. It is fully symmetric so that the choices of contact and target surfaces are arbitrary. At each time step, each node on the slave surface is checked for penetration through the master surface. Unlike the nodes to surface contact type, penetration will only be checked on nodes of the slave surfaces whose normal vectors are oriented towards the master surface as shown in Figure 34. Moreover, it is commonly used for bodies that have large contact areas and the contact surfaces are known [28], [29].
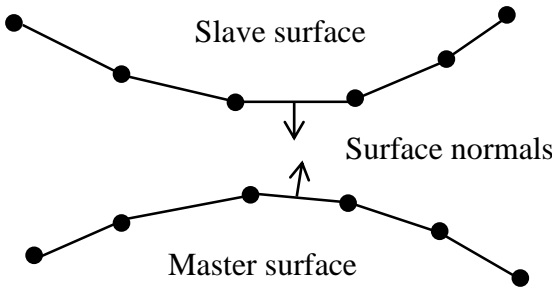
Figure 34: Surface to surface contact

4.3.3 Element Formulations

The choice of element type is in the most cases dependent on the geometry which is to be analyzed. In this study, 8-nodes hexahedral solid element type is preferred. In LS-

DYNA, four different element models are implemented for 8-nodes hexahedral solid element according to integration definitions. They are:

- o Fully integrated S/R solid intended for elements with poor aspect ratio, accurate formulation (ELFORM=-2)
- o Fully integrated S/R solid intended for elements with poor aspect ratio, efficient formulation (ELFORM=-1)
- o Constant stress solid element (ELFORM=1)
- o Fully integrated S/R solid (ELFORM=2).

The most common integration definitions used within LS-DYNA are full integration (ELFORM=2) and reduced integration (ELFORM=1). In three dimensions, the full integration definition, shown to the right in Figure 35, uses eight integration points within the area of a quadrilateral element while reduced integration elements, shown to the left in Figure 35, have only one integration points [30].
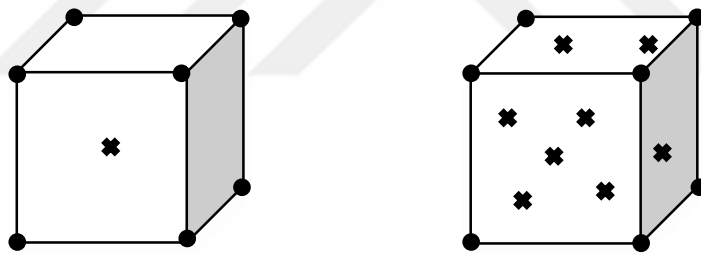
Figure 35: The reduced and full integration elements

For reduced integration, the element can only consider a state of constant stress and strain with one integration point defined over length. However, the element can consider a linear variation of stress and strain over the defined length if two integration points are taken over the length. Another disadvantage is hourglass problem in the reduced integration element. The element is susceptible to zero energy deformation modes because of the single integration point like shown in Figure 36. To prevent this problem, hourglass stabilization is defined in LS-DYNA. Although, reduced integration elements have these limitations, they can give much improved efficiency as compared to fully integration ones. Also, this method can even work for severe

deformations. On the contrary, the full integration elements are more unstable in large deformation applications [30].
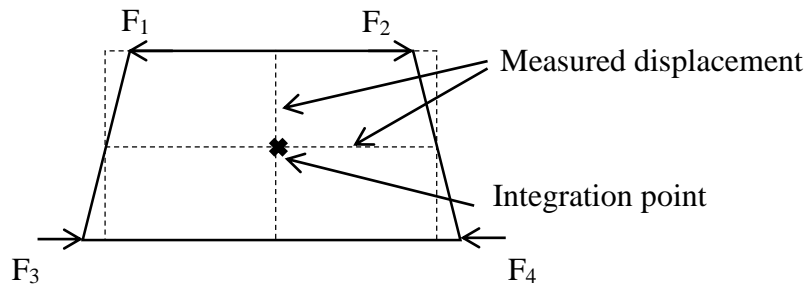
Figure 36: Hourglass mode

The main problem for the full integration definition is that the element is too stiff in many situations, especially for poor aspect ratios. It is known as the shear locking. To mitigate this problem, two new versions of fully integration definitions are implemented as "ELFORM -1" and "ELFORM -2". Although these definitions solve the transverse shear locking problem, the efficiency is still less than both reduced integration and typical full integration definitions. Within this scope, reduced integration solid elements are used in the problem to eliminate the shear lock and negative volume problems.

4.3.4   Material Models

4.3.4.1   Johnson Cook Constitutive Model

There are several constitutive models to describe the deformation behavior of materials for ballistic impact, high velocity shaping and forming, machining in which high strain rate and large strain are occurred. In this study, the working principle of pyrotechnic explosive bolts is very similar to the ballistic impact problem. The piston impacts the bolt body with high velocity. Moreover, pyrotechnic substance inside the body can create very high pressure in a few microseconds. The material properties under these dynamic cases are different from the static one due to strain rate effects. However, at high-strain rate applications, the flow stress should be defined as a function of strain, strain rate and temperature effects [10]. Therefore, Johnson-Cook constitutive model,

which is widely used for high-strain rate applications, was taken as material model for the bolt body and piston of pyrotechnic explosive bolt. Also, its parameters are more easily obtainable than the other constitutive models in the literature.G. R. Johnson and W.H. Cook developed a strength model for metals subjected to large strains, high strain rates and high temperatures at 1983 [31]

$$\bar{\sigma} = [A + B(\bar{\varepsilon})^n]\left[1 + C\ln\left(\frac{\dot{\bar{\varepsilon}}}{\dot{\bar{\varepsilon}}_0}\right)\right]\left[1 - \left(\frac{T - T_0}{T_m - T_0}\right)^m\right], \qquad (79)$$

where the first brackets describes the flow stress in terms of strain, i.e. work hardening; second one simulates the strain rate effects, i.e. strain-rate hardening, and the last part describes temperature effects on the flow stress, i.e. thermal softening [32]. Therein, $\bar{\sigma}$ is the equivalent flow stress; the parameter A represents the initial yield strength of the material at room temperature; B represents strain sensitivity; $\bar{\varepsilon}$ is the equivalent plastic strain and the parameter n is the hardening exponent. In the strain-rate hardening set, C represents strain rate sensitivity; $\dot{\bar{\varepsilon}}$ is the equivalent plastic strain rate, while $\dot{\bar{\varepsilon}}_0$ is a reference strain rate. In the temperature hardening set, T_0 is room temperature and T_m is the melting temperature of material while m represents the temperature sensitivity.

4.3.4.1.1 Bolt Body

The Johnson Cook constitutive model described in the previous section can be utilized in LS-DYNA by using "JOHNSON COOK" card to model the bolt body in AISI 4340 steel. Its material properties are stated in Table 10 [33].

Table 10: Material properties of AISI 4340 steel

Definition		Unit	Value
Reference density	ρ_0	kg/m^3	7830
Shear modulus	G	Pa	7.7×10^{10}
Poisson's Ratio	ν	-	0.28
Initial yield strength	A	Pa	7.92×10^8
Hardening constant	B	Pa	5.1×10^8
Hardening exponent	n	-	0.26
Strain rate constant	C	-	0.014
Thermal softening exponent	m	-	1.03
Melting temperature	T_m	K	1793
Room temperature	T_0	K	300
Reference strain rate	$\dot{\bar{\varepsilon}}_0$	-	1.0
Specific heat	C$_p$	J/kg.K	477

4.3.4.1.2 Piston

The Johnson Cook constitutive model described in the previous section can be utilized in LS-DYNA by using "SIMPLIFIED JOHNSON COOK" card to model the bolt body in 17-4PH stainless steel. It is a chromium-nickel-copper precipitation-hardening martensitic stainless steel. The main difference between the "JOHNSON COOK" and "SIMPLIFIED JOHNSON COOK" cards is the thermal softening set of the flow stress. Since 17-4PH stainless steel has higher resistance to fracture than AISI 4340 steel, there is not too much plastic deformations on the piston body. Material properties for 17-4PH stainless steel are stated in Table 11 [11].

Table 11: Material properties of 17-4PH stainless steel

Definition	Unit	Value

Reference density	ρ_0	kg/m^3	7750
Young's modulus	E	Pa	1.96 x10^{11}
Poisson's Ratio	ν	-	0.272
Initial yield strength	A	Pa	1.192x10^9
Hardening constant	B	Pa	4.935x10^8
Hardening exponent	n	-	0.272
Strain rate constant	C	-	0.014

4.3.4.2 Equation of State

During the impact, the shock wave propagation causes pressurize and it exceeds the material strength by several orders of magnitude. To determine the pressure in a shock-compressed solid, the Mie-Grüneisen equation of state can be used [34]

$$p = \frac{\rho_0 C_0^2 \left(1 - \frac{\rho_0}{\rho}\right)\left[1 - \frac{\Gamma_0}{2}\left(1 - \frac{\rho_0}{\rho}\right)\right]}{\left[1 - s\left(1 - \frac{\rho_0}{\rho}\right)\right]^2} + \Gamma_0 E. \tag{80}$$

Therein, C_0 is the bulk speed of sound; ρ_0 is the initial density; ρ is the current density; Γ_0 is Grüneisen's gamma at the reference state; s is a linear Hugoniot slope coefficient and E is the internal energy per unit reference volume.

In this study, the bolt body is the critical part due to the shock wave propagation. Therefore, The Mie-Grüneisen equation of state can be utilized in LS-DYNA to model the bolt body. Material properties for AISI 4340 steel are stated in Table 12 [33].

Table 12: Input parameters for the Mie-Grüneisen EOS model

Definition		**Unit**	**Value**
Bulk speed of sound	C_0	m/s	4578
Slope coefficient	s	-	1.33
Grüneisen's Gamma	Γ_0	-	1.67

4.3.5 Failure Model

The failure or fracture criterion of Johnson Cook is based on a plastic fracture strain. It depends on the ratio of hydrostatic pressure to the von Mises equivalent stress, strain

rate and temperature. In this failure model, the damage at the material element accelerates immediately during plastic straining. Failure occurs when the damage variable,

$$D = \sum \frac{\Delta \varepsilon}{\varepsilon_f}, \tag{81}$$

reaches to one. It can vary between zero, i.e. material not damaged and one. Therein, $\Delta \varepsilon$ is the increment of equivalent plastic strain and ε_f is the equivalent plastic strain at failure. The equivalent plastic strain at failure,

$$\varepsilon_f = \left[D_1 + D_2 exp \left(D_3 \frac{\sigma_m}{\sigma_{eq}} \right) \right] \left[1 + D_4 \ln \left(\frac{\dot{\varepsilon}_p}{\dot{\varepsilon}_0} \right) \right] \left[1 + D_5 \left(\frac{T - T_0}{T_m - T_0} \right) \right], \tag{82}$$

can be expressed under the current conditions of strain rate, temperature, pressure ad equivalent [31]. Therein, D_1 to D_5 are the material constants; σ_m represents the mean or hydrostatic stress; σ_{eq} is equivalent stress; $\dot{\varepsilon}_p$ is the plastic strain rate; $\dot{\varepsilon}_0$ is the strain rate at reference state; T_0 is the room temperature and T_m is the melting temperature of the material. In this study, the failure parameters for AISI 4340 steel are listed in Table 13 [10].

Table 13: Failure parameters for AISI 4340 steel

D_1	0.05
D_2	3.44
D_3	-2.12
D_4	0.002
D_5	0.61

4.4 MESH AND MESH PROPERTIES

In this section, the convergence and mesh independence of the developed models are controlled to get most accurate results in a short solving time. Convergence means that the results of the analysis should not be affected by the changing the mesh size. Normally, the system should converge to a repeatable solution with decreasing element

size in terms of stress, deformation and velocity. Nonetheless, an additional mesh refinement with the convergence does not affect the analysis if the model is independent of mesh.

4.4.1 Mesh Conditions

Hexahedral mesh model can be used to maintain high solver accuracy and speed up in solving time by applying the sweep method in ANYS-Mechanical module. Before meshing, the geometry of the bolt body and piston can be divided into several pieces to perform the sweep method as shown in Figure 37. Another advantage of this division is that the most critical regions can be modeled with a small element size while undeformed regions can be modeled with higher element size to reduce the cost of analysis.
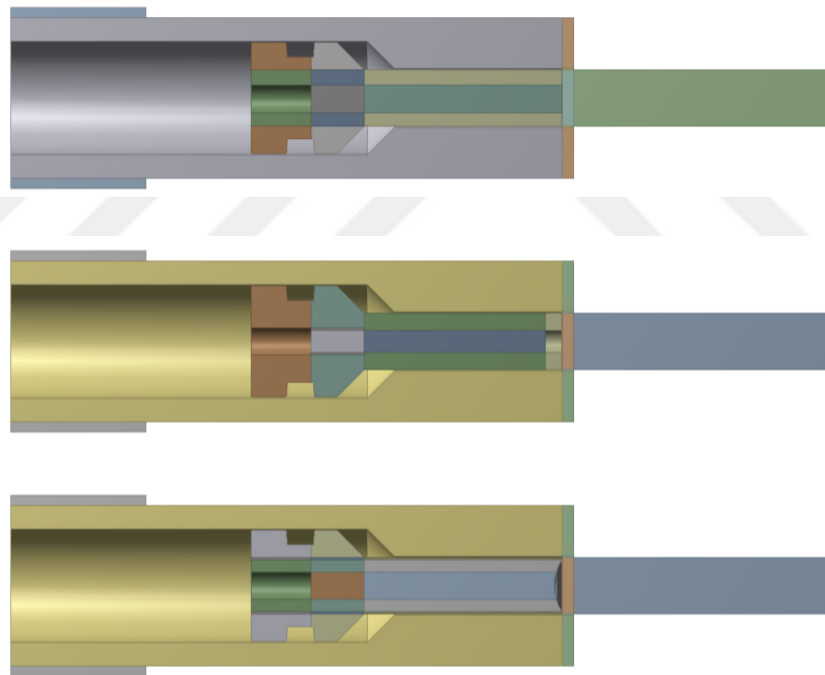
Figure 37: Divided pyrotechnic explosive bolt geometries

The most critical parts on the systems are the pistons and separation section on the bolt body. Detailed information about the mesh conditions used in the models is provided in Table 14 for these critical sections. The average skewness value is the primary quality measures for a mesh in terms of how close to ideal. It becomes around 0.25 for

all pistons and separation section. As a result, the equilateral cell, that is a best option for the analysis, can be obtained. The second quality measures are the aspect ratio. It can be defined as the ratio of the minimum and maximum edge sizes. This value can be taken as one for optimal case but it is hardly to obtain in most analyses. In this study, it became fewer than 10 for the critical sections of the pistons as shown in Figure 38. For the separation section on the bolt body, aspect ratio became around 3 as indicated in Figure 39.

Table 14: Mesh conditions of pistons and separation section

Properties	Piston-1	Piston-2	Piston-3	Separation Section
Number of Nodes	89099	101937	189664	392593
Number of Elements	84339	96669	181602	54896
Maximum Skewness	0.85956	0.96364	0.96364	0.96364
Average Skewness	0.25604	0.24271	0.25149	0.25149
Maximum Aspect Ratio	197.8	155.87	174.49	174.49
Average Aspect Ratio	6.8585	17.326	15.516	15.616
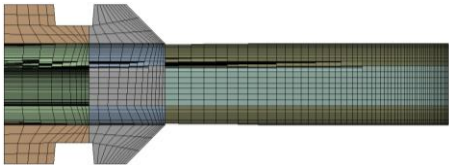
P-1: Aspect Ratio < 10   P-1: Skewness < 0.5

P-2: Aspect Ratio < 10   P-2: Skewness < 0.5
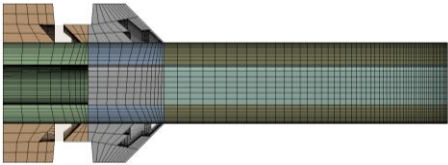
P-3: Aspect Ratio < 10   P-3: Skewness < 0.5
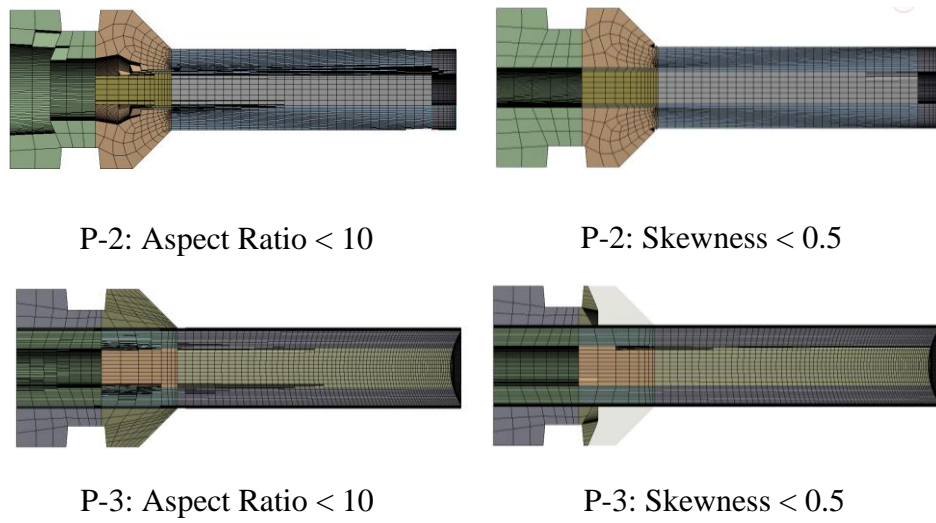
Figure 38: Aspect ratio and skewness values of the pistons

Aspect Ratio < 3   Skewness < 0.3
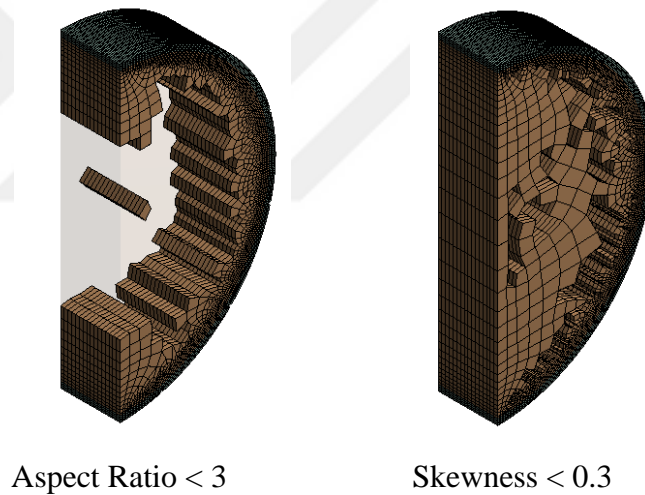
Figure 39: Aspect ratio and skewness value of the separation section

4.4.2 Mesh Independency and Converge of the Models

The critical section of the bolt body can be meshed with different element size and refinement to get the accurate analysis results. In this manner, three different meshed separation sections were created. In the first coarse model shown in Table 15, the edge represented with red arrow is divided into ten sections and element size becomes 0.05 mm at the outer part of the geometry. As a result of this modeling technique, total number of elements on the separation section and piston is 14150 and 229518,

respectively. In the second model shown in Table 16, the division of the edge is augmented to 16 and the element size decreases to 0.025 mm. With this convergence and refinement, the total number of elements becomes 55120 and 365674 for the separation section and bolt body, respectively. In the last model shown in Table 17, the edge represented with red arrow is divided into 20 pieces and the element size on the outer section, which is represented with blue arrow, decreases to 0.02 mm.

Table 15: Coarse mesh properties of the separation section
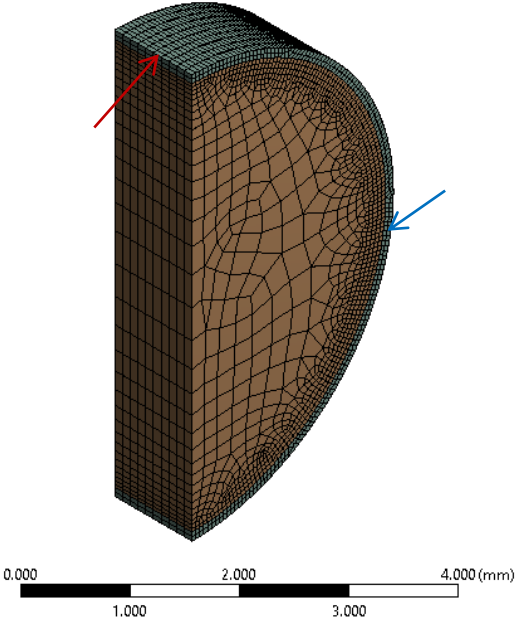
Model-1a			
Element size	:	0.05 mm	
Number of division	:	10	
Total number of elements on selected body	:	14150	
Total number elements on bolt body	:	229518	

Table 16: Medium mesh properties of the separation section

Model-1b		
Element size	:	0.025 mm
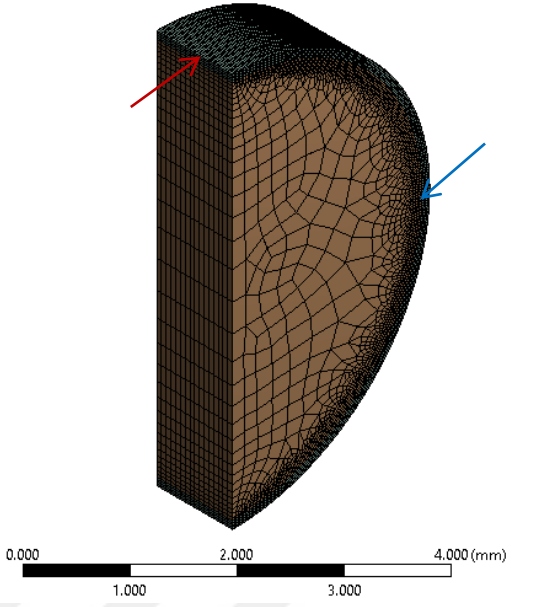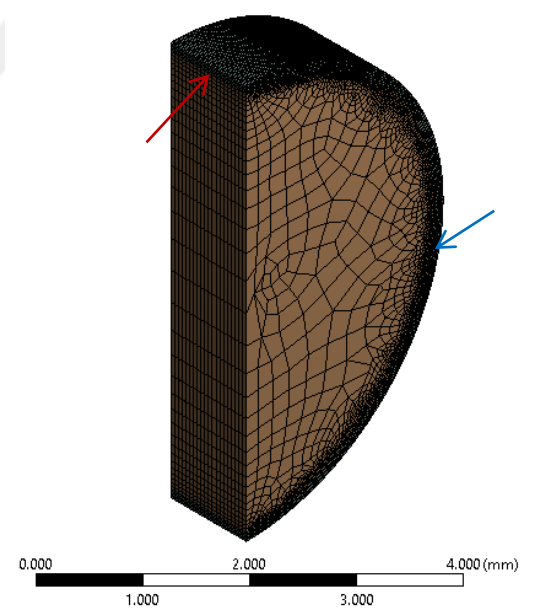
Number of division	:	16	
Total elements on selected body	:	55120	
Total elements on bolt body	:	365674	

Table 17: Fine mesh properties of the separation section

Model-1c			
Element size	:	0.02 mm	
Number of division	:	20	
Total elements on selected body	:	89660	
Total elements on bolt body	:	591901	

These generated models can be analyzed in LS-DYNA by using one CPU to observe the convergence and mesh independency of the pyrotechnic explosive bolt. The computational time is defined as 3×10^{-5} sec for all there models. Then, the total costs

become 9784, 37502 and 55045 sec as shown in Table 18 for coarse, medium and fine mesh models, respectively.

Table 18: Solving time of the created models for convergence and mesh independency

	Model-1a	Model-1b	Model-1c
Problem time [sec]	$3x10^{-5}$	$3x10^{-5}$	$3x10^{-5}$
Total CPU time [sec]	9784	37502	55045
Number of CPU	1	1	1

The simulation results were analyzed by taking consideration into front and separation section velocities of bolt body with velocity of the piston. In the following three figures, solid line represents the analysis results for coarse mesh model (Model-1a); dotted line represents the medium mesh model (Model-1b) results and dashed line represents the compact or fine mesh model (Model-1c) results. In Figure 40, the change of front section velocity with respect to time is presented. Moreover, the data, which are taken from this graph at time 10, 20 and 30 µs, are given in Table 19 to understand the effects of element size and refinement. According to these results, front section velocity of the bolt body for three models became close to each other up to 10 µs. After that, the coarse mesh model started to be different than two other models. Percentage of change velocity for coarse and medium models became 3.2 and this value was 0.88 for medium and fine mesh.
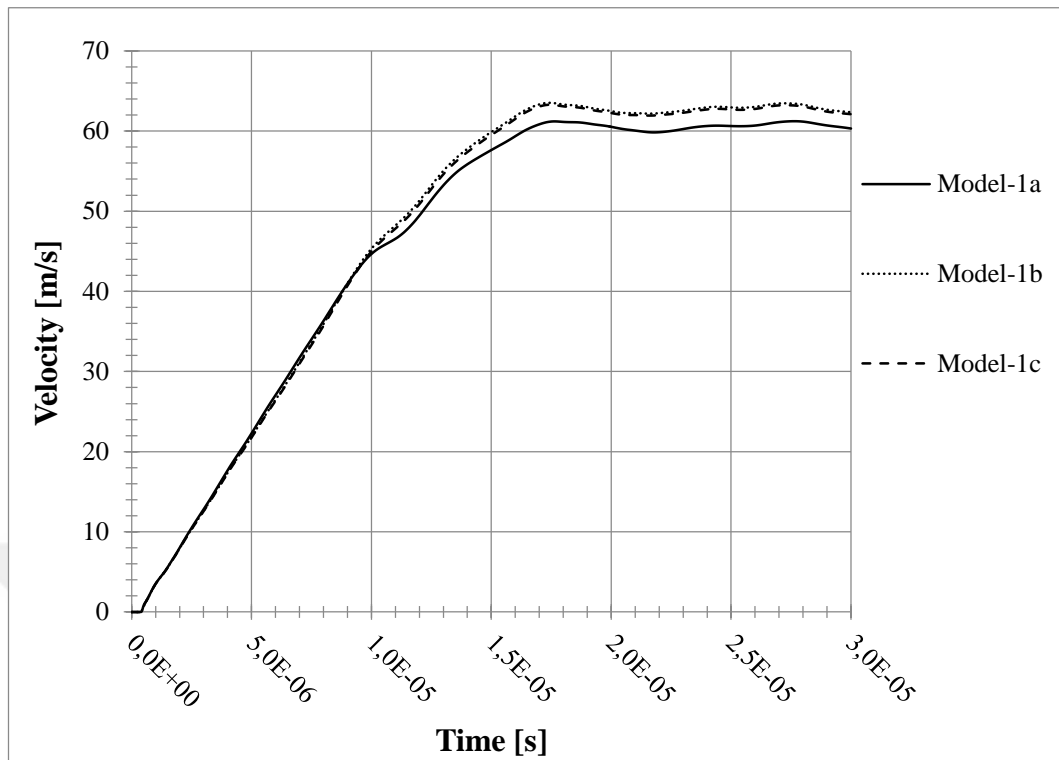
Figure 40: Front section velocity of the bolt body

Table 19: Comparison of simulation results for front section of bolt body

	Model-1a	Model-1b		Model-1c	
Time [μs]	Velocity [m/s]	Velocity [m/s]	%	Velocity [m/s]	%
10	44.6	45.4	1.76	45	0.88
20	60.5	62.5	3.2	62.3	0.32
30	60.4	62.3	3.05	62.1	0.32

In Figure 41, the change of separation section velocity with respect to time is presented. Moreover, the data at time 10, 20 and 30 μs are given in Table 20. At that time, the percentage of velocity change for coarse and medium model is 11.60 and this value decreases to 0.96 between the medium and fine mesh models.
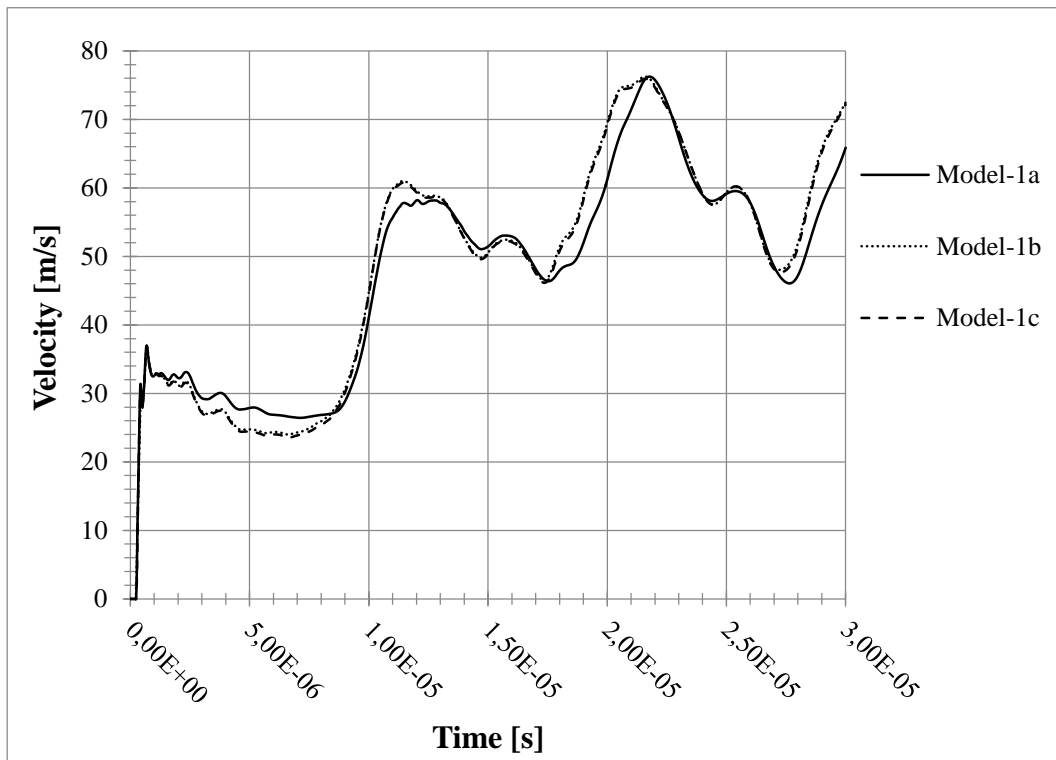
Figure 41: Separation section velocity of the bolt body

Table 20: Comparison of simulation results for separation section of bolt body

	Model-1a	Model-1b		Model-1c	
Time [μs]	Velocity [m/s]	Velocity [m/s]	%	Velocity [m/s]	%
10	41.4	45	8	44.9	0.22
20	61.7	69.8	11.60	69.5	0.43
30	65.9	72.7	9.35	72	0.96

In Figure 42, the velocity change of piston with respect to time is presented. Moreover, the data at time 10, 20 and 30 μs are given in Table 21. At that time, percentage of velocity change for coarse and medium models is 8.04 and this value decreases to 1.28 if medium and fine mesh models are compared.
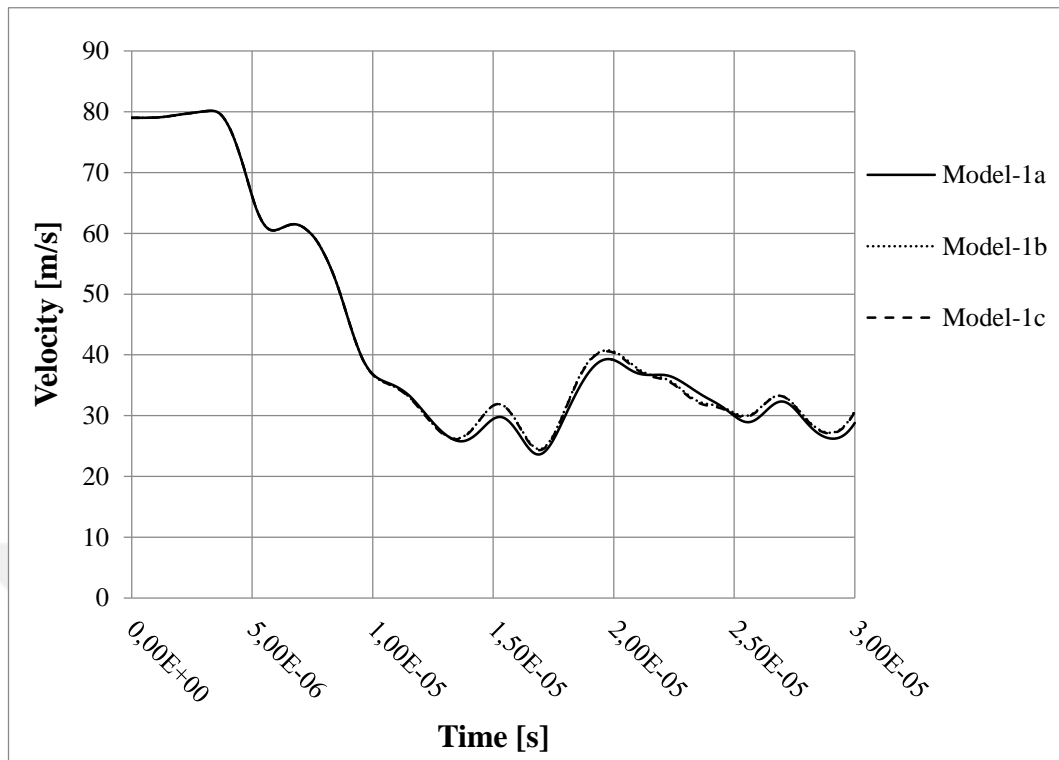
Figure 42: Velocity of the piston

Table 21: Comparison of simulation results for piston

	Model-1a	Model-1b		Model-1c	
Time [μs]	Velocity [m/s]	Velocity [m/s]	%	Velocity [m/s]	%
10	36.8	36.7	0.27	36.7	0
20	39.1	40.5	3.46	40.3	0.49
30	28.6	31.1	8.04	30.7	1.28

The simulations in LS-DYNA show that the medium model, which has 0.025 mm element size and 16 divisions on the critical edge, converges since the results does not distinctly change even the element size decreases. Also, this model is mesh independency when observing the effects of refinement on the model. As a result, Model-1b is the selected case for other analyses since it contains fewer elements than Model-1c.

4.5 INITIAL AND BOUNDARY CONDITIONS

In a system, where the pyrotechnic explosive bolt is used, two separated body are fixed by using this bolt and nut. In this configuration, the bolt body is fixed at the front side during the working. Therefore, the bolt body can be fixed from the front side as shown in Figure 43. Moreover, the constrained regions should be defined due to the symmetry model.
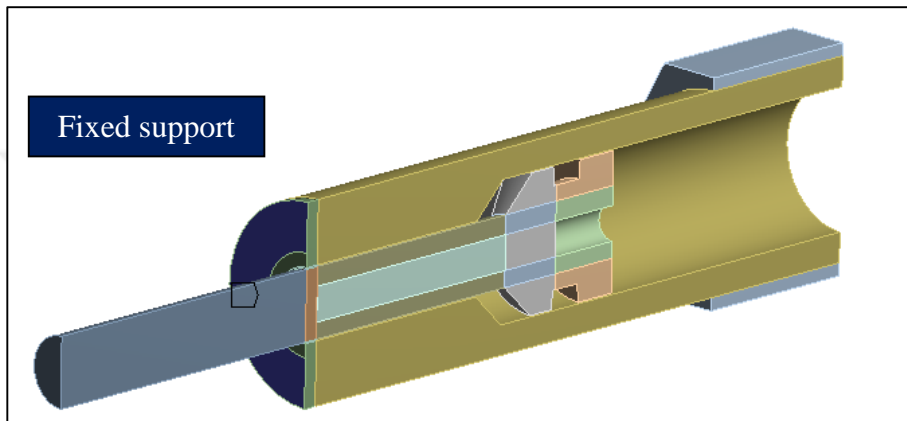
Figure 43: Fixed support on the bolt body

The pyrotechnic combustion in expansion chamber of the explosive bolt can be simulated in developed ballistic code given in previous chapter. The results of this ballistic performance code are the velocity variation of the piston and the pressure in the expansion chamber. In the second part of this study, the velocity value at the impact time of the piston and bolt body, 79 m/s, can be used as initial velocity of the piston. Also, the constant pressure value at 0.0003 sec, 22 MPa, can be defined shown in Figure 44.
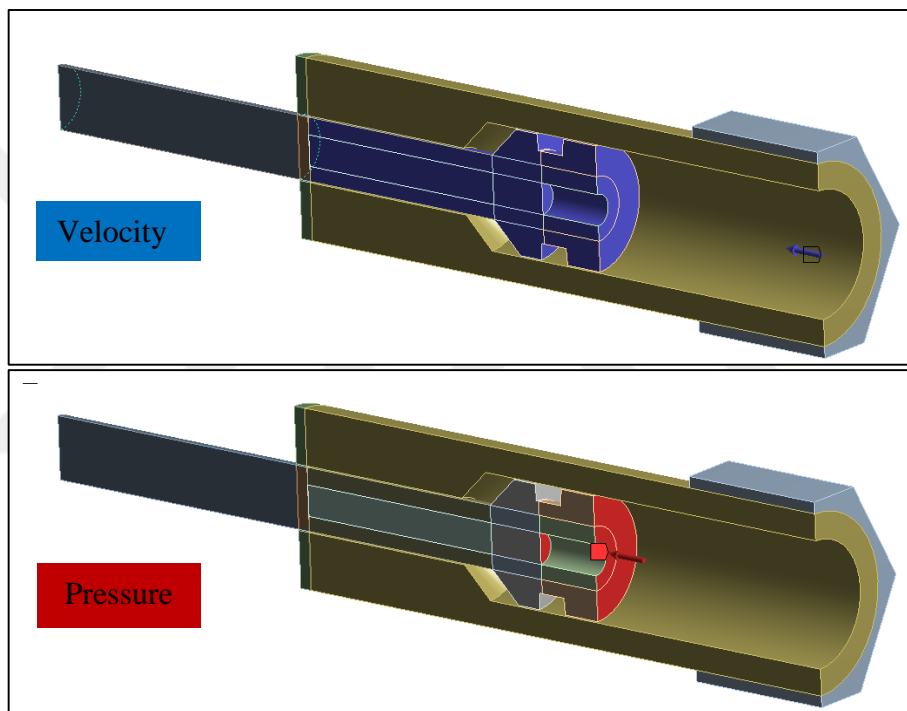
Velocity

Pressure

Figure 44: Velocity and pressure definition on the piston

CHAPTER 5

COMPARISON OF THE MODELS

In this chapter, different piston models for the developed pyrotechnic explosive bolt defined in previous chapters are presented and compared with their failure analysis in LS-DYNA. For the comparison of the models, the velocity and internal energy of the different sections on the explosive bolts were studied. Also, the stress and plastic strain parameters were analyzed to understand the different separation behavior behind these developed models.

First analysis, namely Model-1, covers the modelling of the piston with a flat surface in front as shown in Figure 7. This model has a bigger contact region than the other two models. Therefore in this model, on the separation section which is the most critical part of the bolt body, the stress and strain were expected to become lower compared to the other two models. To be able to observe and analyze deformation on the separation section, it would be useful to closely investigate Figure 45 and Figure 46. The first column under the figures represents the time while the second column illustrates the color distribution values for collected stress and strain data. When the piston impacted the bolt body with 79 m/s, the effective plastic strains on that section became between 0.02598 and 0.03898 at 1.21 µs as shown with green range in Figure 45. At the same time, the Von-mises stress on the separation section changed between 0.6229 and 0.9344 MPa as shown with green range in Figure 46. The failure of the elements on the separation section was started to occur between 4.84 µs and 5.75 µs as shown in Figure 45 and Figure 46. These plastic deformations propagated through the outer part of the separation section defined in

Figure 54. After 10.6 µs, it is realized that the critical part was totally separated from the main bolt body. That period, between 4.84 and 10.6 µs, can be used to show the

separation time of the pyrotechnic explosive bolts even if it is not considered to be precise.

Second analysis, namely Model-2, covers modelling of the piston with a hole in as shown in Figure 7. The intention of the hole in front of the piston is to decrease the contact area between the piston and bolt body. The contact region in this model is narrow compared to the one in Model-1. Therefore, it is expected that the stress and strain on that region result higher values than in the case of Model-1. For this case, Figure 47 and Figure 48 can be used to study the deformation on the separation section. Again, the first column under the figures represents the time while the second column illustrates the color distribution values for collected stress and strain data. When the piston impacted the bolt body with 79 m/s in Model-2, the effective plastic strains on that section were found to be between 0.02702 and 0.04053 at 1.21 μs as shown with green range in Figure 47. At the same time, the Von-mises stress on the separation section changed between the 0.7503 and 1.226 MPa as shown with green range in Figure 48. The failure of the elements on the separation section occurred at very close to 5.75 μs as shown in Figure 47 and Figure 48. After 11.93 μs, that critical part was totally separated from the main bolt body. For this case, it is apparent that the separation time is around 4.85 μs. Also, this model has very similar separation characteristics with Model-1 such as propagation of plastic failure on the elements.

Last analysis, namely Model-3, covers modelling of the piston with a convex built in front as shown in Figure 7. The intention of the convex structure in front of the piston is to decrease the contact area between the piston and bolt body. The contact region in this model is narrow compared to the ones in Model-1 and Model-2. Therefore, the stress and strain on the contact region has expected to be higher than the ones in the other two models. When the piston impacted the bolt body with 79 m/s in Model-3, the effective plastic strains on the front of the piston become higher than the strains on the bolt body at 1.21 μs as shown in Figure 49. At the same time, the Von-mises stress on the separation section changed between the 0.8417 and 1.052 MPa as shown with green in Figure 50. In these figures, same methodology is used to give details about the simulation. The first column under the figures represents the time while the second

90

column illustrates the color distribution values for collected stress and strain data. The failure of the elements on the separation section occurred between 8.48 and 9.69 µs as shown in Figure 49 and Figure 50. After 13.02 µs, that critical part was not still separated from the main bolt body. One possible reason for this result would be that in effective plastic strain force is created on the front part piston because of the smaller contact region between the bolt body and piston. Another possible reason can be the front shape of the piston. The piston in Model-3 can be considered as more deformable than the piston in Model-2. This argument can be validated with the comparison of the deformations on the piston for Model-2 and Model-3.

1.2107x10⁻⁶ sec			2.7265x10⁻⁶ sec		
0.03898	0.05197	0.05846	0.2189	0.2918	0.3283

3.9374x10⁻⁶ sec			4.8476x10⁻⁶ sec		
0.5082	0.6775	0.7622	0.6521	0.8695	0.9782

5.7556x10⁻⁶ sec			6.9676x10⁻⁶ sec		
1.080	1.440	1.621	0.9271	1.236	1.391

8.4825x10⁻⁶ sec			9.6958x10⁻⁶ sec		
1.739	2.319	2.608	2.257	3.010	3.386

1.0604x10⁻⁵ sec			1.1209x10⁻⁵ sec		
2.745	3.660	4.118	1.319	1.758	1.978

1.3028x10⁻⁵ sec			1.7573x10⁻⁵ sec		
1.319	1.758	1.978	1.319	1.758	1.978

Figure 45: Effective plastic strains for Model-1 at different time

1.2107x10^{-6} sec	2.7265x10^{-6} sec
9.344E+08 | 1.246E+09 | 1.402E+09	9.718E+08 | 1.296E+09 | 1.458E+09
3.9374x10^{-6} sec	4.8476x10^{-6} sec
9.777E+08 | 1.304E+09 | 1.467E+09	9.878E+08 | 1.317E+09 | 1.482E+09
5.7556x10^{-6} sec	6.9676x10^{-6} sec
9.800E+08 | 1.307E+09 | 1.470E+09	9.238E+08 | 1.232E+09 | 1.386E+09
8.4825x10^{-6} sec	9.6958x10^{-6} sec
8.764E+08 | 1.168E+09 | 1.315E+09	8.737E+08 | 1.165E+09 | 1.310E+09
1.0604x10^{-5} sec	1.1209x10^{-5} sec
8.733E+08 | 1.164E+09 | 1.310E+09	8.368E+08 | 1.116E+09 | 1.255E+09
1.3028x10^{-5} sec	1.7573x10^{-5} sec
6.785E+08 | 9.042E+08 | 1.017E+09	8.684E+08 | 1.158E+09 | 1.302E+09

Figure 46: Von-Mises stress for Model-1 at different times

93

1.2117x10⁻⁶ sec		2.7264x10⁻⁶ sec		
0.04053	0.05404	0.6079	0.1812	0.2416	0.2718
3.9389x10⁻⁶ sec		4.8476x10⁻⁶ sec		
0.3307	0.4410	0.4961	0.5883	0.7844	0.8824
5.7569x10⁻⁶ sec		6.9689x10⁻⁶ sec		
0.6959	0.9279	1.044	0.9221	1.229	1.383
8.4835x10⁻⁶ sec		9.6964x10⁻⁶ sec		
1.080	1.440	1.620	1.767	2.357	2.651
1.0605x10⁻⁵ sec		1.121x10⁻⁵ sec		
2.191	2.921	3.286	2.399	3.198	3.598
1.3029x10⁻⁵ sec		1.7574x10⁻⁵ sec		
2.297	3.062	3.445	2.297	3.062	3.445
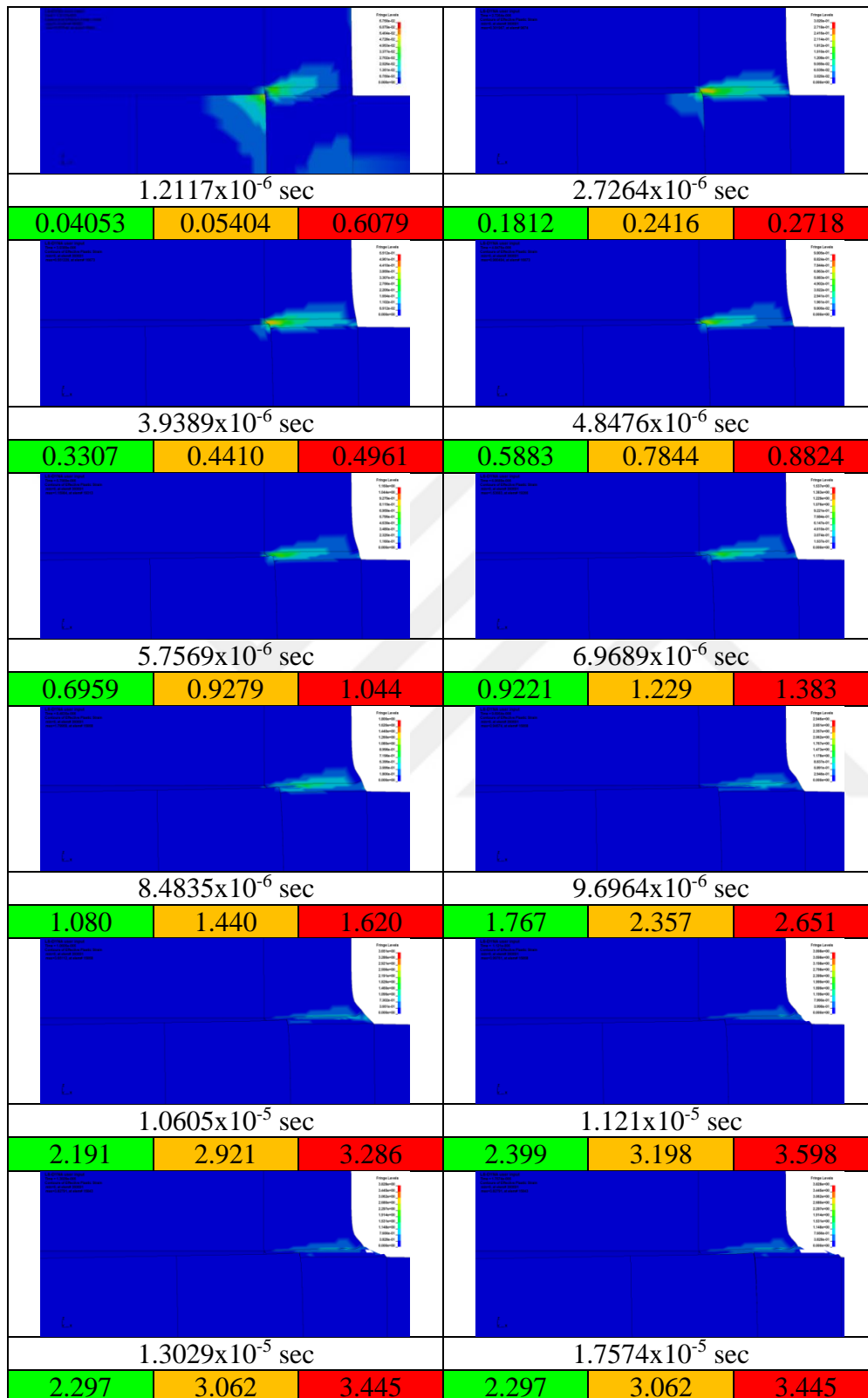
Figure 47: Effective plastic strains for Model-2 at different time

| 1.2117x10⁻⁶ sec | 2.7264x10⁻⁶ sec |

| 1.126E+09 | 1.501E+09 | 1.688E+09 | 1.191E+09 | 1.588E+09 | 1.786E+09 |

| 3.9389x10⁻⁶ sec | 4.8476x10⁻⁶ sec |

| 1.209E+09 | 1.611E+09 | 1.813E+09 | 1.211E+09 | 1.615E+09 | 1.816E+09 |

| 5.7569x10⁻⁶ sec | 6.9689x10⁻⁶ sec |

| 1.219E+09 | 1.626E+09 | 1.829E+09 | 1.193E+09 | 1.591E+09 | 1.790E+09 |

| 8.4835x10⁻⁶ sec | 9.6964x10⁻⁶ sec |

| 1.182E+09 | 1.575E+09 | 1.772E+09 | 1.224E+09 | 1.632E+09 | 1.836E+09 |

| 1.0605x10⁻⁵ sec | 1.121x10⁻⁵ sec |

| 1.224E+09 | 1.632E+09 | 1.836E+09 | 1.160E+09 | 1.647E+09 | 1.740E+09 |

| 1.3029x10⁻⁵ sec | 1.7574x10⁻⁵ sec |

| 1.139E+09 | 1.518E+09 | 1.708E+09 | 9.456E+09 | 1.261E+09 | 1.418E+09 |

Figure 48: Von-Mises stress for Model-2 at different times

1.2119x10^{-6} sec			2.7262x10^{-6} sec		
0.2235	0.2980	0.3352	0.2647	0.3529	0.3970

3.9389x10^{-6} sec			4.8476x10^{-6} sec		
0.2691	0.3588	0.4036	0.2751	0.3669	0.4127

5.7565x10^{-6} sec			6.9689x10^{-6} sec		
0.3763	0.5017	0.5644	0.5243	0.6990	0.7864

8.4834x10^{-6} sec			9.6967x10^{-6} sec		
0.6513	0.8684	0.9770	0.6875	0.9166	1.031

1.0605x10^{-5} sec			1.1211x10^{-5} sec		
0.7981	1.064	1.197	0.888	1.184	1.332

1.3028x10^{-5} sec			1.7574x10^{-5} sec		
1.115	1.487	1.673	1.121	1.494	1.681

Figure 49: Effective plastic strains for Model-3 at different times

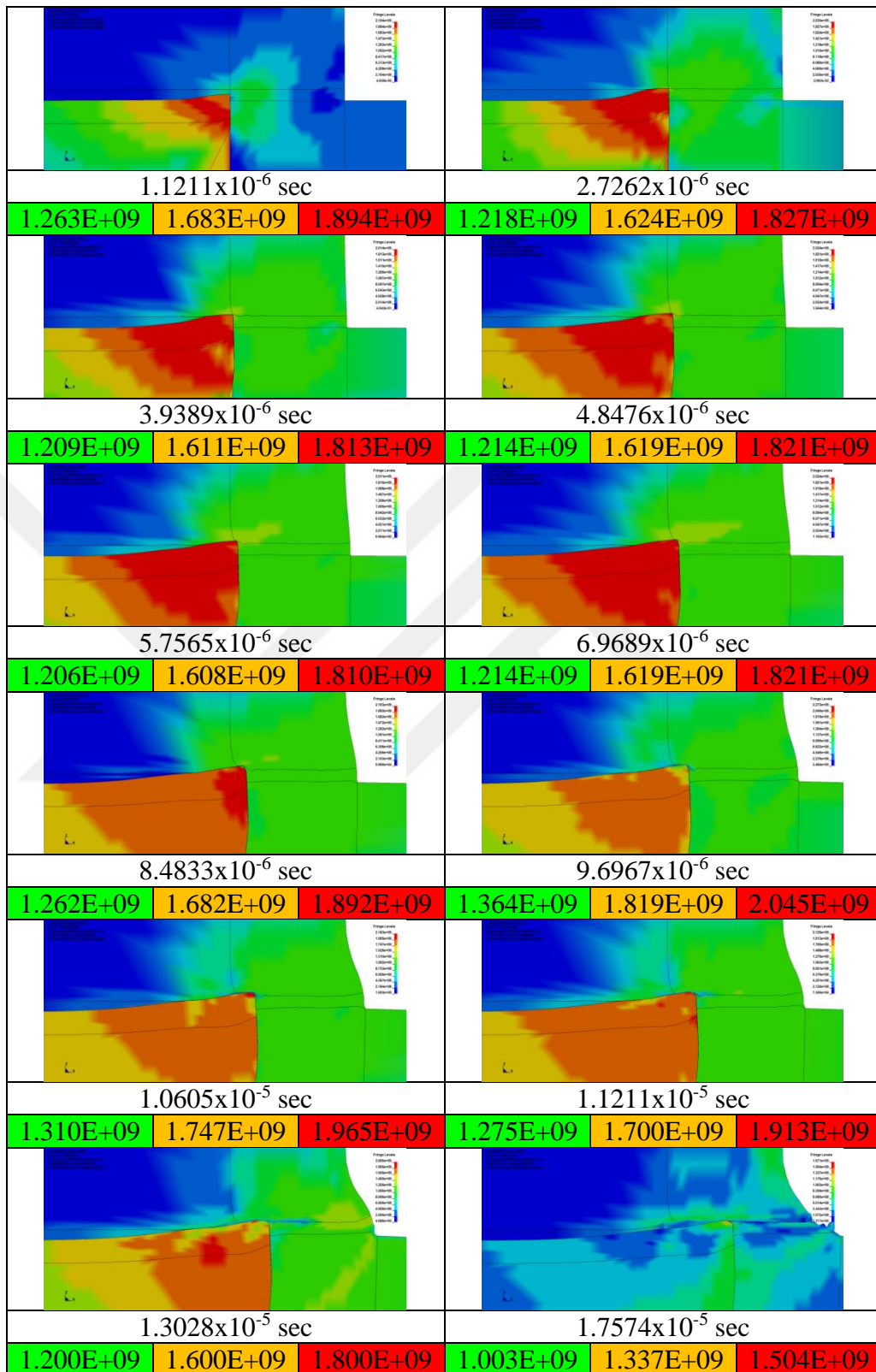| 1.1211x10⁻⁶ sec			2.7262x10⁻⁶ sec		
1.263E+09	1.683E+09	1.894E+09	1.218E+09	1.624E+09	1.827E+09
3.9389x10⁻⁶ sec			4.8476x10⁻⁶ sec		
1.209E+09	1.611E+09	1.813E+09	1.214E+09	1.619E+09	1.821E+09
5.7565x10⁻⁶ sec			6.9689x10⁻⁶ sec		
1.206E+09	1.608E+09	1.810E+09	1.214E+09	1.619E+09	1.821E+09
8.4833x10⁻⁶ sec			9.6967x10⁻⁶ sec		
1.262E+09	1.682E+09	1.892E+09	1.364E+09	1.819E+09	2.045E+09
1.0605x10⁻⁵ sec			1.1211x10⁻⁵ sec		
1.310E+09	1.747E+09	1.965E+09	1.275E+09	1.700E+09	1.913E+09
1.3028x10⁻⁵ sec			1.7574x10⁻⁵ sec		
1.200E+09	1.600E+09	1.800E+09	1.003E+09	1.337E+09	1.504E+09

Figure 50: Von-Mises stress for Model-3 at different times

To understand the separation behavior of these models, the velocity change of separation sections, the results are illustrated in Figure 51 for all three models. Model-1 and Model-2, represented with solid line and square dot line, respectively, showed the same behavior. Until the separation, the velocities in the first two models were in tendency to decrease with some oscillations as shown in Figure 51. Velocity of the separation section in Model-1 started to increase around 6.54 µs and continued until 11.4 µs while this separation duration was between 7.11 and 11.1 µs for Model-2. Model-3, represented with dashed line, exhibited a different separation behavior and also it seems more stabilized than the other models. Therefore, the separation duration cannot be realized in this graph. However, it is known that its separation time is higher in simulation when compared to the other models.
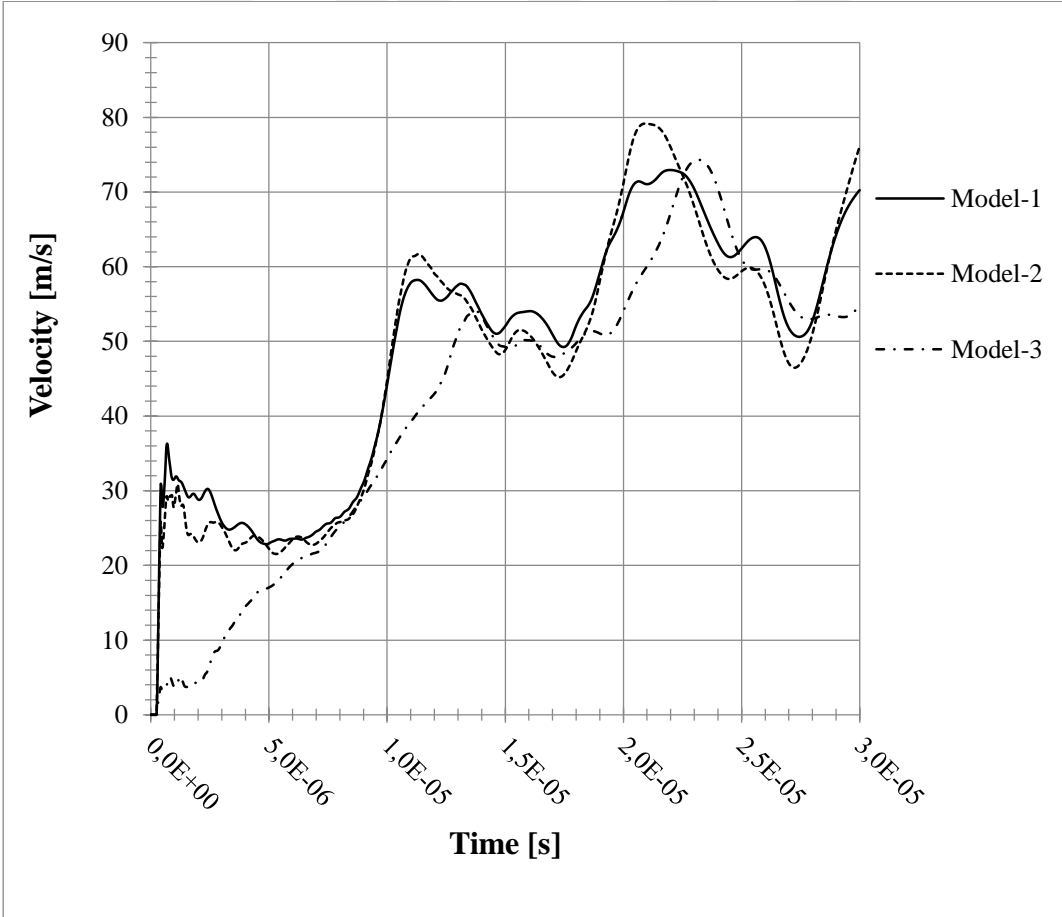

Figure 51: Velocity change of the separation section

Figure 52 illustrates the velocity change of front section of bolt body for all models. The velocity in Model-1, represented with a solid line, increased linearly up to around 63.9 m/s, but its slope tends to decrease after 1 µs. During the same period, the velocity of front section increased in Model-2; however, its maximum velocity is very close to Model-1. This situation can support the phenomenon for the separation times for Model-1 and Model-2 in Figure 51. It is known that the separation duration in Model-2 is less than the Model-1. The velocity change of front section for Model-3, represented with a dashed line, increased exponentially up to 61.6 m/s. The possible reason of this different separation behavior in Model-3 can be the deformation on the piston as shown in Figure 49 and Figure 50.
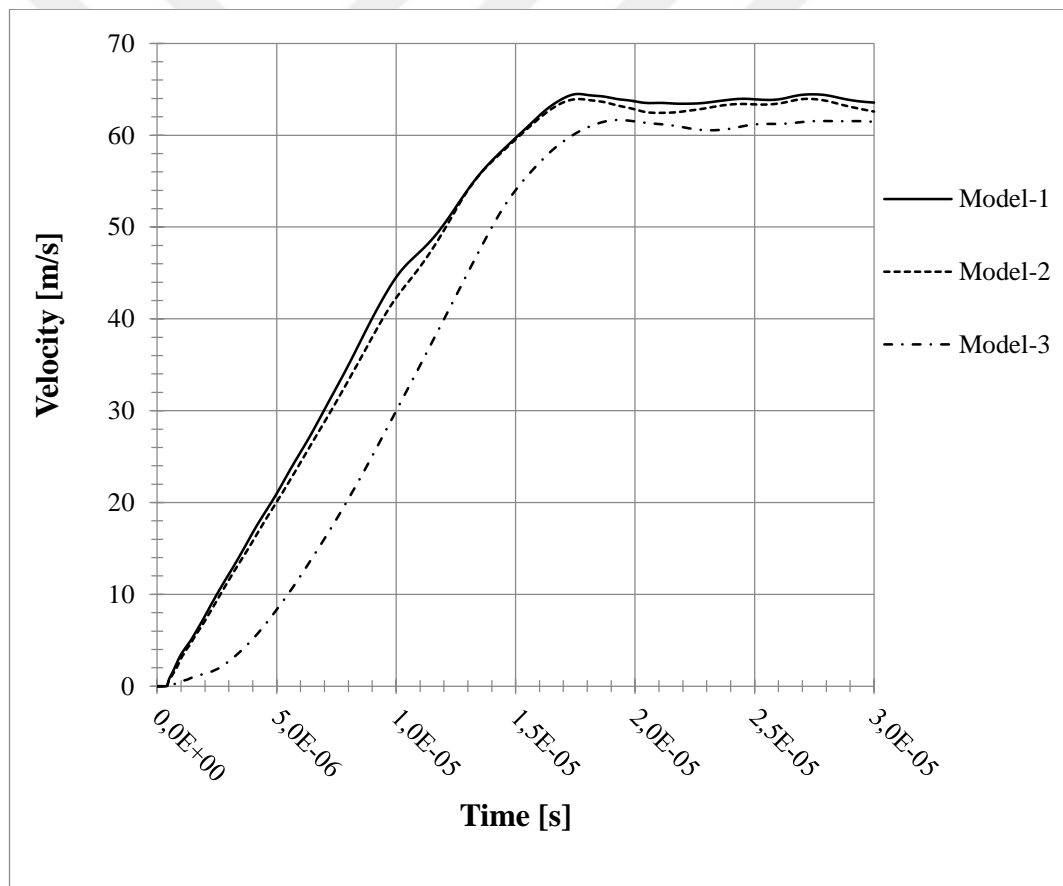

Figure 52: Velocity change of the front section

Figure 53 shows the comparison of velocity of piston between all three models. The results for Model-1 display similar qualitative trends as Model-2 in that the velocity decreases after 3.5 µs, reaches a minimum, then start increasing with the separation of the piston and front section of bolt body at around 17 µs. For Model-3, this separation occurred at 18.2 µs.
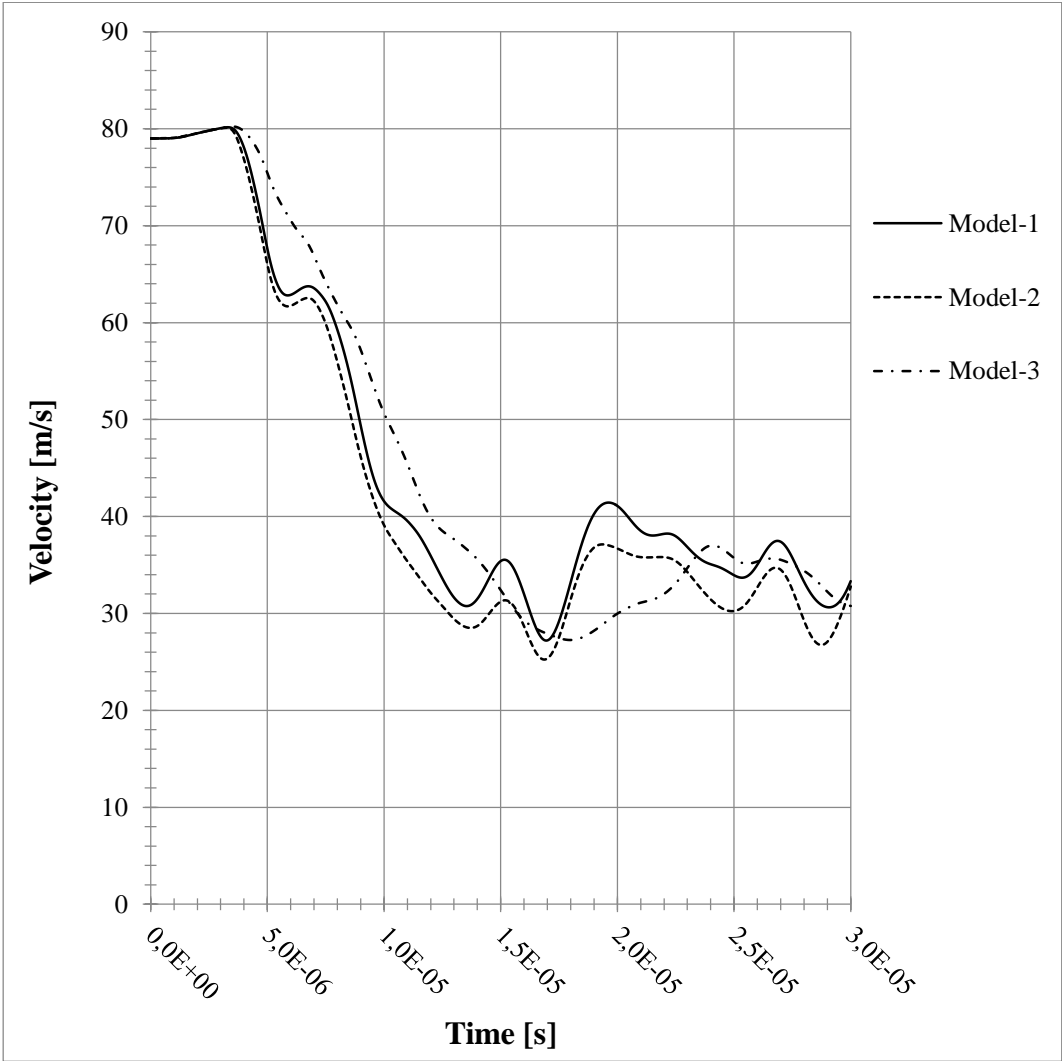

Figure 53: Velocity change of the piston

Another way to understand the separation behavior of the model in analysis is internal energy. Figure 55 and Figure 56 illustrate the internal energy change of inner and outer parts of separation sections shown in Figure 54. In the simulation, it is seen that inner

separation section in Model-3 deformed extensively when compared to other models due to the high velocity impact resulting from small contact area. As a result of it, the internal energy of Model-1 became higher than the other two models. The predicted maximum internal energies for Model-1 and Model-2 during the separation are 0.32 and 0.29 J, respectively. For Model-3, this value is around 0.69 J. At the outer part of the separation section, the internal energy in Model-2 increases rapidly as shown in Figure 56. However, this situation is not similar for Model-1 and Model-3.
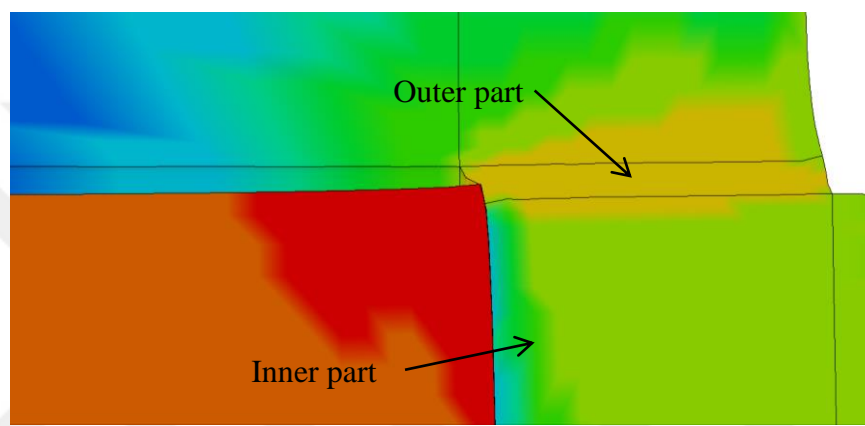

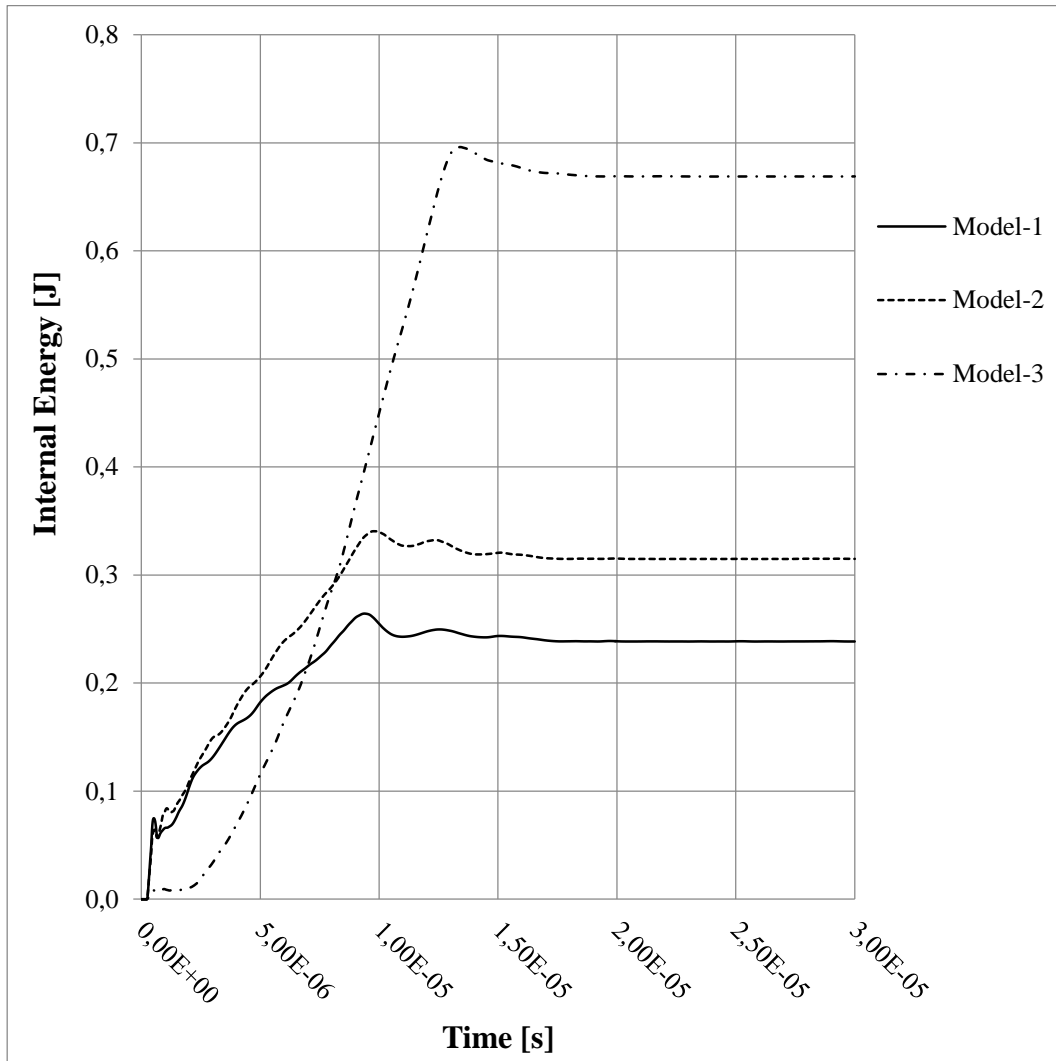Figure 54: Inner and Outer Parts of Separation Section

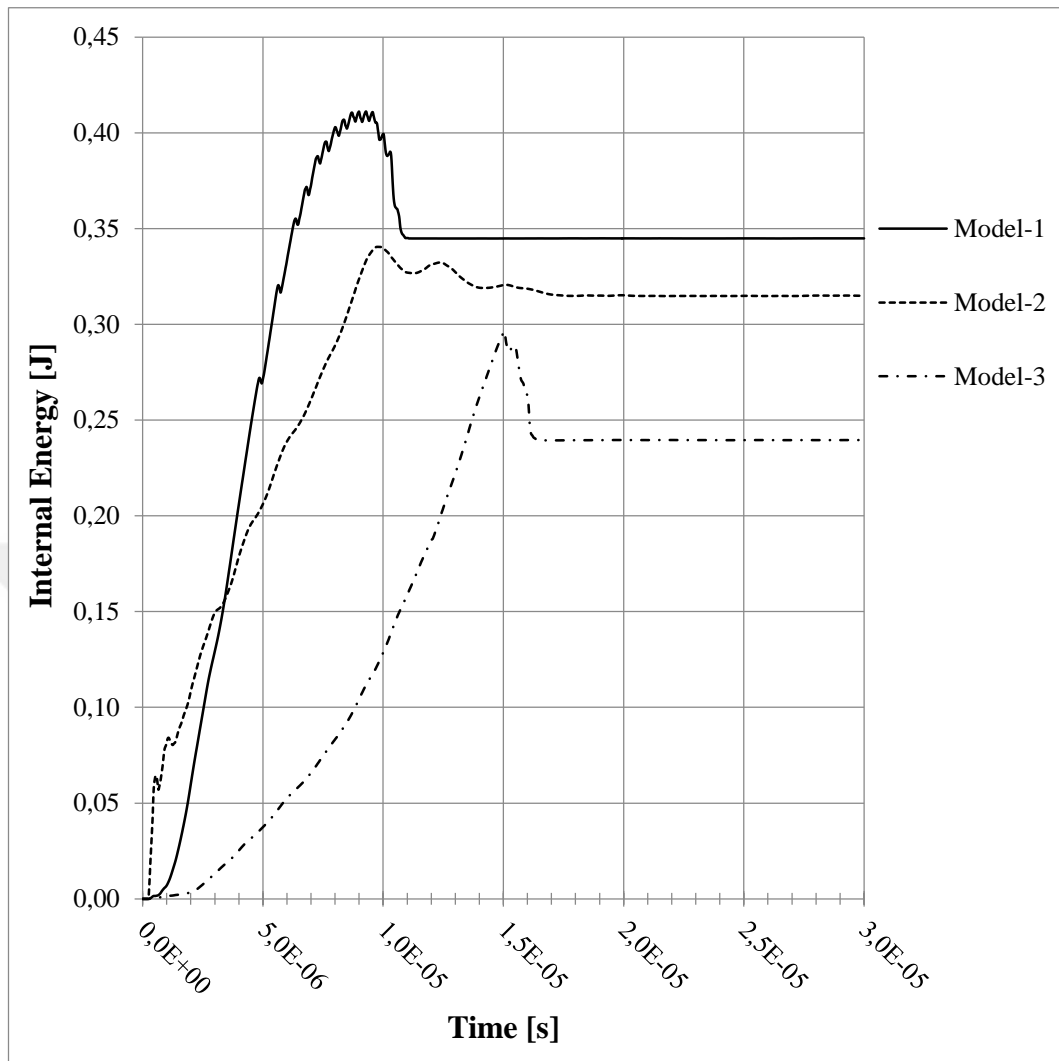Figure 55: Internal energy change of the inner part of separation section

Figure 56: Internal change of the outer part of separation section

Figure 57 illustrates the internal energy of the total system for Model-1, Model-2 and Model-3. The results for Model-1, represented with solid line, display similar qualitative trends as Model-2, represented with square dot line, up to 5 μs. After that time, the internal energy of Model-2 starts increasing with a higher slope than Model-1 and it reaches to 6.46 J at 10.5 μs. For Model-1, the maximum internal energy on the system becomes 6.14 J at the same time. For Model-3, the different separation behavior can be observed at the beginning of the simulation. During that period, the internal energy in Model-3 increases exponentially while the increments in Model-1 and Model-2 are linear.
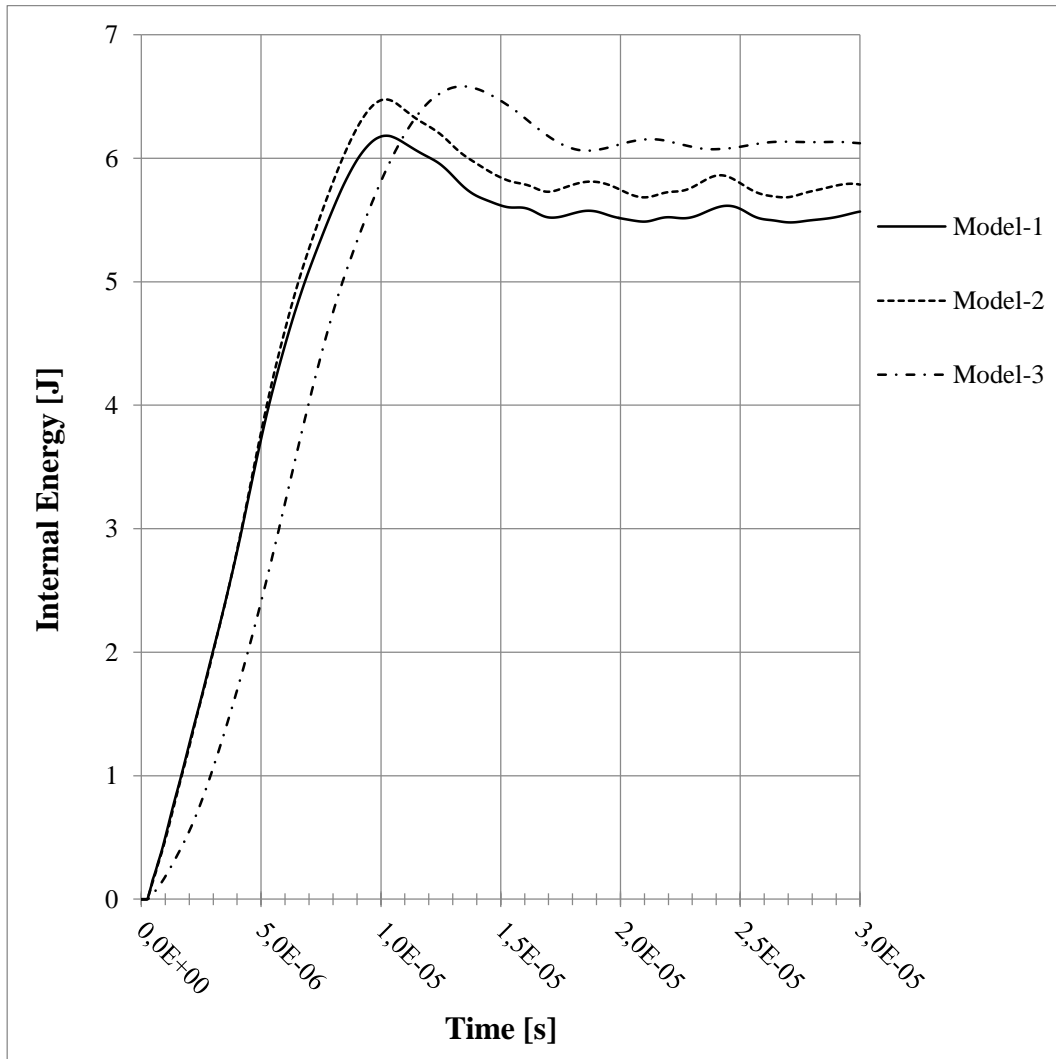
Figure 57: Internal energy of the system

CHAPTER 6

CONCLUSION AND DISCUSSION

In this thesis study, the different separation behaviors of the pyrotechnic explosive bolt were observed. For this purpose, the analyses were carried out to investigate the separation behaviors with different piston geometries. To illustrate the separation characteristics of developed three distinct models, a pyrotechnic combustion and explicit analyses in LS-DYNA were performed.

In the first step, pyrotechnic combustion analysis was studied and 0-D ballistic solver was developed to simulate the performance of the initiator. By using this developed model, the pressure and temperature in the expansion chamber can be predicted with the position and velocity of the piston. Then, the predicted pressure expansion was validated with closed bomb experiments. As a result, there is a good agreement between the experimental and numerical results if considering 10% error margin in NASA Standards.

In the second step, the explicit analyses were performed to simulate the separation of the developed models in LS-DYNA. To reduce the cost of analysis, the predicted velocity of piston at the impact time, which was taken from the pyrotechnic combustion analysis, were used as initial velocity of the piston in LS-DYNA. Also, mesh dependency was performed to get optimum results by using Model-1.

After the explicit analysis of Model-1, it is observed that the separation duration is around 4.86 µs. Notice that the duration time between the ignition of the initiator and impact of the piston should be added this separation duration to get exact solution. As a result, the exact separation time was predicted as 311 µs. The internal energy of the system was also studied to analyze the separation characteristics of Model-1 and as a result, it is the lowest value in all three models. Therefore, Model-1 can be preferred

with most reliable model when considering the clean separation without fragmenting parts and minimum dissipation energy.

In Model-2, the separation time is around 4 µs and it is less than the Model-1. If the duration time between the ignition of the initiator and impact of the piston is added to this separation duration, the exact separation time is 311 µs. The possible reason for this short separation is that high stress concentrations were created on the separation section due to the small contact region. However, the internal energy of the pyrotechnic explosive bolts during the separation is a bit more than the internal energy of Model-1. Therefore, Model-2 can be preferred when the separation time is critical.

In Model-3, the separation behavior was very different than the other two models. Although it has the smallest contact region in all three models, the front part of the body totally separates from the bolt body at 16.4 µs. If the duration time between the ignition of the initiator and impact of the piston is added this separation duration, the exact separation time is around 316 µs. Since the contact region between the piston and bolt body is very small, the stress concentrations at the front section of the piston was very high and as a result, high deformations were observed in Z-direction. Moreover, the internal energy of the system was also studied to analyze the separation characteristics of Model-3 and as a result, it is the highest value in all three models. Therefore, the clear separation cannot be observed in the system due to the high deformable piston.

The current thesis study may be improved in many ways. These are left as possible future works and may be listed as:

o In the ballistic simulation, the closure on the initiator can be modeled to get high accuracy for the increasing pressure in the expansion chamber at the beginning.

o In the ballistic simulation, the chemical database can be created for other pyrotechnic materials.

o In the ballistic simulation, the detailed heat transfer model can be developed to observe the effects on the performance of the initiator.

- In the explicit analysis for Model-3, can be modeled with higher ductile material to eliminate the deformations on the piston.
- In the explicit analysis for Model-2, can be optimized to get better separation than Model-1 by changing the diameter of the hole on the front of the piston.

REFERENCES

[1] Karl O. Brauer, *Handbook of Pyroechnics*. New York: Chemical Publishing Co. Inc., 1974.

[2] D. Han and H. Sung, "Parametric Analysis and Design Optimization of a Pyrotechnically Actuated Device," vol. 17, no. 3, pp. 409–422, 2016.

[3] K. A. Gonthiert and J. M. Powers, "Formulation, Predictions and Sensitivity Analysis of a Pyrotechnically Actuated Pin Puller Model," *J. Propuls. Power*, vol. 10, no. 4, 1994.

[4] J. M. Powerst and K. A. Gonthier, "Sensitivity Analysis for a Pyrotechnically Actuated Pin Puller Model *," no. July 1993.

[5] S. G. Jang, H. N. Lee, and J. Y. Oh, "Performance modeling of a pyrotechnically actuated pin puller," *Int. J. Aeronaut. Sp. Sci.*, vol. 15, no. 1, pp. 102–111, 2014.

[6] A. Braud, "Performance Modeling of Explosively Actuated Devices," no. December, 2006.

[7] P. M. C. L. Pacheco and M. A. Savı, "Modeling and Simulation of a Shape Memory," *Rev. Eng. e Ciências Apl.*, pp. 1–16, 2000.

[8] H. S. Lee, "Numerical Characterization of Detonator Performance in an Explosive Bolt Device," *49th AIAA/ASME/SAE/ASEE Jt. Propuls. Conf.*, pp. 1–9, 2013.

[9] L. EL, H. H.C., and K. J.W., "Adiabatic Expansion of High Explosive," Livermore, 1968.

[10] G. R. Johnson and W. H. Cook, "Fracture characteristics of three metals subjected to various strains, strain rates, temperatures and pressures," *Eng. Fract. Mech.*, vol. 21, no. 1, pp. 31–48, 1985.

[11] J. Lee, J.-H. Han, Y. Lee, and H. Lee, "Separation characteristics study of ridge-cut explosive bolts," *Aerosp. Sci. Technol.*, vol. 39, pp. 153–168, 2014.

[12] NASA, "Pyroshock Test Criteria," *NASA Tech. Stand. Syst.*, pp. 12–20, 2011.

[13] J. Lee *et al.*, "Pyroshock Prediction of Ridge-Cut Explosive Bolts Using Hydrocodes," *Shock Vib.*, vol. 2016, 2016.

[14] D. Hwang, J. Lee, J. Han, Y. Lee, and D. Kim, "Numerical Analysis and Simplified Mathematical Modeling of Separation Mechanism for the Ball-type Separation Bolt," *J. Korean Soc. Propuls. Eng.*, vol. 20, no. 3, pp. 63–70, 2016.

[15] N. Aeronautics, "NASA Reliability and Maintainability (R&M) Standard for Spacelight and Support Systems," 2017.

[16] F. Salazar, "Design and Performanc Specification for NSI-1 (NASA Stadard Initiator-1)," Houston, Texas, 1999.

[17] J. M. Powers, D. S. Stewart, and H. Krier, "Theory of Two-Phase Detonation-Part I : Modeling," *Combust. Flame*, vol. 80, pp. 264–279, 1990.

[18] B. J. McBride and S. Gordon, "CET93 and CETPC: An Interim Updated Version of the NASA Lewis Computer Program for Calculating Complex Chemical Equilibria with Applications," Ohio, 1994.

[19] A. Burcat, B. Ruscic, and Chemistry, "Third millenium ideal gas and condensed phase thermochemical database for combustion (with update from active thermochemical tables).," Illinois, 2005.

[20] P. B. Kempa, "ICT-Thermodynamic- Code (ICT-Code)." Fraunhofer Institute, Pfinztal.

[21] B. P. William H. Press, and W. Flannery, Saul A. Teukolsky, and T. Vetterling., "Runge-Kutta Method," in *Numerical Recipes in C: The Art of Scientific Computing*, 3rd ed., Cambridge: Cambridge University Press, 1990, pp. 710–714.

[22] B. J. McBride, S. Gordon, and B. J. McBride, "Computer Program for Calculation of Complex Chemical Equilibrium Compositions and Applications," *NASA Reference Publication 1311*. Cleveland, p. 184, 1994.

[23]   J. M. Powers and K. A. Gonthier, "Pyrotechnic Modelling for the NSI Driven Pin Puller," in *Internal Fluid Mechanics Division*, 1992.

[24]   J. Bement and L. Schimmel, "Determination of Pyrotechnic Functional Margin," Virginia.

[25]   L. J. Bement and M. L. Schimmel, "A Manual for Pyrotechnic Design , Development and Qualification," Virginia, 1995.

[26]   J. S. Sun, K. H. Lee, and H. P. Lee, "Comparison of implicit and explicit finite element methods for dynamic problems," *J. Mater. Process. Technol.*, vol. 105, no. 1–2, pp. 110–118, 2000.

[27]   H. Hilber and T. Hughes, "Collocation, dissipation and for time integration schemes in structural dynamics," ... *Eng. Struct. Dyn.*, vol. 6, no. December 1976, pp. 99–117, 1978.

[28]   LSTC, "Theory Manual." Livermore Software Technology Corparation, California, p. Section 27.2, 2018.

[29]   J. Bi, "Consitutive Modeling of Aliminum Foam and Finite Element Implementation for Crash Simulations," The University of North Carolina, 2012.

[30]   D. K. Coleman, "Evaluation of Concrete Modeling in LS-DYNA for Seismic Application," The University of Texas, 2016.

[31]   G. R. Johnson and W. H. Cook, "A constitutive model and data for metals subjected to large strains, high strain rates and high temperatures," in *Proc. 7th Int. Symp. on Ballistics*, 1983, pp. 541–547.

[32]   T. Özel and Y. Karpat, "Identification of constitutive material model parameters for high-strain rate metal cutting conditions using evolutionary computational algorithms," *Mater. Manuf. Process.*, vol. 22, no. 5, pp. 659–667, 2007.

[33]   Simulia, "Simulation of the ballistic perforation of aluminum plates with Abaqus / Explicit," *Abaqus Technol. Br.*, p. 6, 2012.

[34]   M. Grüneisen, *Zur kinetischen Theorie der einatomigen Körper*. Annalen der Physik, 1903.